THESIS FOR THE DEGREE OF DOCTOR OF PHILOSOPHY

Grid-forming wind power plants

Anant Narula

CHALMERS
UNIVERSITY OF TECHNOLOGY

Department of Electrical Engineering
Chalmers University of Technology
Gothenburg, Sweden, 2023

Grid-forming wind power plants

Anant Narula

ISBN: 978-91-7905-812-8
Doktorsavhandlingar vid Chalmers tekniska högskola
Ny serie nr 5278
ISSN 0346-718X
This thesis has been prepared using LaTeX.

Department of Electrical Engineering
Chalmers University of Technology
SE-412 96 Gothenburg, Sweden
Phone: +46 (0)31 772 1000
www.chalmers.se

Printed by Chalmers Digital Printing
Gothenburg, Sweden, 2023

To my buggu, parents, teachers and friends.

Grid-forming wind power plants

ANANT NARULA
Division of Electric Power Engineering
Department of Electrical Engineering
Chalmers University of Technology, Sweden

Abstract

With growing concerns over climate change, the power system is witnessing an unprecedented growth in electricity generation from intermittent renewable energy sources (RES) such as wind and solar, which are commonly interfaced to the grid by power-electronic converters. However, increasing the penetration level of converter-interfaced generation units reduces the number of synchronous generators (SGs) in the grid that provide system services to support voltage and frequency, either inherently or through mandatory requirements and market products. This brings several challenges for the grid operators, which include increasing risk of harmonic interactions, decreasing system inertia and reduction in the short-circuit power of the grid, which all together might jeopardize the security and availability of the power systems. As a countermeasure, it is necessary that the power-electronic-based generation units not only provide grid support services that are originally provided by the SGs, but also operate in harmony with other generation units in all kinds of grid conditions. As a result, the concept of grid-forming (GFM) control, which mimics the beneficial properties of the SGs in converter systems, has emerged as a viable solution to allow effective and secured operation of power systems with increased penetration of converter-based resources.

This thesis investigates the application of GFM control strategies in wind power plants (WPPs). In particular, the focus of the work will be on developing an effective GFM control strategy for the energy storage systems (ESS) in WPPs that not only supports the operation of the WPP in various grid conditions, but also offers a certain degree of GFM properties to the overall WPP. To start with, the selection of the most suitable GFM control strategy for wind power applications is made by evaluating and comparing various control strategies available in the literature. The comparison is based on their influence on the frequency characteristics of the converter and robustness of the

controller in varying grid strength. To address the transient stability problem of GFM converters during current limitation, a novel strategy based on the limitation of converter's internal voltage vector is developed, which effectively limits the converter current to a desired value and retains the GFM properties of the converter at all times. An experimental setup is used to validate the effectiveness of the proposed limitation strategy in case of various grid disturbances. By implementing the proposed GFM control strategy for the ESS in a test WPP model, it is shown using detailed time-domain simulation results that the GFM behaviour can be offered to the overall WPP. The Network Frequency Perturbation (NFP) plots are used to verify the GFM behaviour of the considered WPP. Furthermore, an overview of various energy storage technologies (ESTs) suitable for providing ancillary services from WPPs is presented. With a focus on the two most suitable ESTs, i.e., batteries and supercapacitors, recommendations are given for design and sizing of the ESS for a given application. Finally, a coordinated control strategy between the WPP and SGs is developed, which facilitates the provision of frequency support from the WPP and at the same time reduces the energy storage requirements for the converter system.

Keywords: Ancillary services, coordination, current limitation, energy storage systems (ESS), frequency support, grid-forming (GFM), inertia, transient stability, wind power plants (WPPs).

Acknowledgments

First of all, I would like to express my sincere and deepest gratitude to my examiner, main supervisor and head of the division of Electric Power Engineering, Prof. Massimo Bongiorno for his impeccable technical guidance, inspiration, encouragement and support throughout the course of this Ph.D. project. Thank you for your unwavering dedication towards research and education, which has helped me enhance my research, experimental, writing as well as teaching skills and reach this stage of my career. I consider myself fortunate to have had the opportunity to work under your guidance. I would also like to thank you for creating a friendly and inclusive working environment, which made this journey of learning enjoyable.

A special thanks goes to my co-supervisor, Dr. Mebtu Beza, for improving my mathematical as well as experimental skills and providing enormous help in conducting the laboratory tests. I would like to express my heartfelt gratitude for all your teachings and support during challenging times in the project. I would also like to thank Dr. Peiyuan Chen for being my co-supervisor and for many fruitful discussions at various occasions. Thank you Peiyuan for showing confidence in me from the beginning of my Ph.D. study and helping me to develop time management skills.

This project has been carried out as part of the VinEl Program with project number "44960-1" and has been funded by Energimyndigheten (Swedish Energy Agency). The financial support provided by the sponsoring organization is greatly acknowledged.

My acknowledgements go to members of the reference group for this project: Dr. Jan R. Svensson (Hitachi Energy Research), Robert Eriksson (SvK) and Jean-Philippe Hasler (Hitachi Energy) for the beneficial inputs and nice discussions through the course of the project. I would also like to thank Dr. Alireza Nami (Hitachi Energy Research) for introducing me to Prof. Massimo Bongiorno and encouraging industrial collaboration in the project.

Furthermore, I would like to thank my office mate and fellow Ph.D. student Paul Imgart for interesting discussions, suggestions and collaborations. I am extremely grateful to you for supporting me extensively over the past few months, which helped me to focus on writing this thesis. I would also like to thank master's thesis student Lluc Figueras Llerins for helping me with some parts of this project. I further would like to thank my office mate and fellow Ph.D. student Ahmed Sunjaq for having discussions from time to time and

sharing his Baklava with me, which helped in gaining some calories at work.

I would like to take this opportunity to thank Dr. Panagiotis Bakas (Hitachi Energy) and Dr. Luca Bessegato (SvK) for developing in me an interest for research activities right from my master's education at KTH Royal Institute of Technology, Stockholm.

The great and memorable experiences I had at Chalmers would not be possible without warm and welcoming work and social environment. For this I am very grateful to all my fellow Ph.D. students and colleagues, who have helped me in one way or another.

A special thanks goes to my friends Prasenjeet, Pavithra, Priyank, Judi, Sepideh, Poorya, Rose Lily, Shoaib, Adi, Amra, Arancha, Giorgio and Nikolina, who always have my back and are there for me when I need them the most.

Finally, I have no words to express my deepest gratitude to my parents and sister for loving, caring, supporting and believing in me. Last but not the least, I would like to express my deepest appreciation and love to my wife and soulmate Vini. Your unwavering support, love, care and patience have been the foundation of my success. I could not have made it to the end without you and I look forward to spending the rest of my life with you.

Anant Narula
Gothenburg, Sweden
March, 2023

Acronyms

GFM:	Grid forming
APC:	Active-power controller
APL:	Active-power loop
AVC:	AC-voltage controller
BESS:	Battery energy storage system
CC:	Current controller
CES:	Centralized energy storage
COI:	Center-of-inertia
CSA:	Current saturation algorithm
CVC:	Cascaded vector-control
DCCV:	Direct control of converter voltage
DFT:	Discrete Fourier Transform
DSBC:	Double star bridge cell
DUT:	Device under testing
EMF:	Electromotive force
ESR:	Equivalent series resistance
ESS:	Energy storage system
EST:	Energy storage technology
FCR:	Frequency Containment Reserve
FES:	Flywheel energy storage
FFR:	Fast Frequency Reserve

FRR:	Frequency Restoration Reserve
GFL:	Grid following
GFM:	Grid forming
GWEC:	Global Wind Energy Council
HV:	High voltage
HVAC:	High Voltage Alternating Current
HVDC:	High Voltage Direct Current
IEL:	Inertia-emulation loop
LV:	Low voltage
MMC:	Modular multilevel converter
NFP:	Network Frequency Perturbation
OCV:	Open circuit voltage
PCC:	Point-of-common-coupling
PI:	Proportional integral
PLL:	Phase-locked loop
pu:	Per-unit
RES:	Renewable energy sources
RoCoF:	Rate-of-change-of-frequency
SC:	Synchronous condenser
SCESS:	Supercapacitor-based energy storage system
SCR:	Short-circuit ratio
SG:	Synchronous generator
SMES:	Superconducting magnetic energy storage

SOC:	State of charge
STATCOM:	Static synchronous compensator
VA:	Virtual admittance
VABC:	Virtual-admittance based control
VCC:	Vector-current controller
VSC:	Voltage-source converter
WPP:	Wind power plant
WT:	Wind turbine

Contents

Abstract i

Acknowledgements v

Acronyms vii

1 Introduction 1
- 1.1 Background and motivation 1
- 1.2 Purpose of the thesis and main contributions 4
- 1.3 Structure of the thesis 5
- 1.4 List of publications 6

2 Grid-forming control for grid-connected converter systems 9
- 2.1 Introduction 9
- 2.2 Definition of grid-forming capability 10
- 2.3 Grid-forming principle and the proposed active-power controller 12
  - 2.3.1 Classical structure of the active-power controller 13
  - 2.3.2 Impact of steady-state grid-frequency deviation on the classical structure 15
  - 2.3.3 Proposed modification in the active-power controller . . 16

2.4 Grid-forming control strategies and system modeling 17
2.4.1 Cascaded vector-control (CVC) 18
2.4.2 Direct control of converter voltage (DCCV) 24
2.4.3 Virtual-admittance based control (VABC) 28
2.5 Comparison of grid-forming control strategies 32
2.5.1 Ability to prevent adverse control interactions 34
2.5.2 Impact of grid strength on control performance 37
2.6 Summary 38

3 Operation of grid-forming converters during current limitation 41
3.1 Introduction 41
3.2 Angle stability problem of grid-forming converters 42
3.2.1 Voltage-dip induced converter angle instability 45
3.2.2 Frequency-disturbance induced converter angle instability 46
3.3 Proposed methodology to limit converter current 47
3.3.1 Cascaded active-power controller 48
3.3.2 Calculation of active-power limits 53
3.3.3 Calculation of voltage-magnitude limits 53
3.4 Experimental validation of the proposed current-limitation strategy 54
3.4.1 Dynamic performance in case of a RoCoF event 56
3.4.2 Dynamic performance in case of a balanced three-phase voltage dip 56
3.4.3 Dynamic performance in case of a balanced three-phase voltage dip accompanied by a RoCoF event 59
3.5 Controller modifications for unbalanced grid conditions 61
3.5.1 Experimental validation under unbalanced grid conditions 63
3.6 Summary 66

4 Grid-forming wind power plants 67
4.1 Introduction 67
4.2 Description of the investigated system 68
4.3 Description of the wind turbine controller 70
4.4 Evaluation of the grid-forming capability of the wind power plant 72
4.4.1 Phase-angle jump in the onshore grid 73
4.4.2 Linear frequency change in the onshore grid 75
4.4.3 Voltage jump in the onshore grid 77

4.4.4 Presence of a negative-sequence component in the onshore grid . . . 77
4.4.5 Change in the grid impedance . . . 79
4.5 Network Frequency Perturbation (NFP) plot . . . 81
4.5.1 Methodology to generate the NFP plot and its interpretation . . . 81
4.5.2 NFP plot of the offshore wind power plant . . . 89
4.6 Summary . . . 92

5 Energy-storage system for wind power applications 95
5.1 Introduction . . . 95
5.2 Energy storage technologies for ancillary services . . . 96
5.3 Design and modelling of BESS . . . 99
5.3.1 Design of BESS . . . 99
5.3.2 Modelling of BESS . . . 102
5.4 Design and modelling of SCESS . . . 103
5.4.1 Design of SCESS . . . 103
5.4.2 Modelling of SCESS . . . 106
5.5 Control of SCESS-based grid-forming converters . . . 106
5.5.1 Alternative structure for the dc-link voltage controller . 107
5.5.2 Simulation verification . . . 108
5.6 Summary . . . 111

6 Coordination of wind power plants and synchronous generators 113
6.1 Introduction . . . 113
6.2 Frequency regulation in the Nordic power system . . . 114
6.3 Proposed structure of the frequency controller and problem formulation . . . 116
6.4 Modeling of system frequency dynamics and design of coordinated control . . . 121
6.4.1 Frequency dynamics of a system comprising of synchronous generators only . . . 122
6.4.2 Frequency dynamics of a system comprising of synchronous generator and WPP . . . 127
6.5 Simulation verification . . . 130
6.6 Summary . . . 131

7 Conclusions and future Work **135**
7.1 Conclusions 135
7.2 Future work 137

References **139**

CHAPTER 1

Introduction

1.1 Background and motivation

Aiming at reducing the global warming, 196 member states of the United Nations Framework Convention on Climate Change (UNFCCC) have signed the 2015 Paris Agreement on climate change and have agreed to limit global temperature rise to well below 2°C and to pursue efforts to limit it to 1.5°C by the end of the century [1]. A crucial part of these efforts is the decarbonization of the electrical power systems worldwide by using renewable energy sources (RES) such as wind, solar, tidal and wave [2]. Focusing on wind power, according to the statistics from Global Wind Energy Council (GWEC), the total wind capacity has grown rapidly over the past two decades, i.e., from 178 GW in 2010 to 830 GW in 2021 [3]. However, high penetration levels of wind power and other non-synchronous generation units, which are commonly interfaced with the grid through voltage-source converters (VSCs), bring new challenges for the power system operators from stability, reliability and protection point of view [4]–[8]. Some of these challenges are a reduction in the total system inertia, lack of reactive power to support the system recovery after a fault, introduction of new oscillation modes and resonance frequencies, which all

together reduce the stability margin of the network. Consequently, new grid codes and interconnection standards for converter systems have been developed over time to ensure the availability and reliability of the power systems [9]–[17]. Accordingly, such systems are expected to be capable of providing some of the beneficial functionalities of the synchronous generators (SGs) such as frequency support, inertial response, fast fault-current injection and black start.

It is within this context that in the last decade, the concept of grid-forming (GFM) control has emerged as one of the promising solutions to tackle challenges associated with increased penetration of converter-interfaced resources, thereby allowing an effective and secure operation of the future power systems [7], [8], [18]–[24]. Several GFM control strategies have been proposed over the past years, which facilitate the provision of aforementioned functionalities from the converter systems integrated with energy storage [25]–[39]. Being GFM a relatively new concept, there is no single control strategy which is prioritized over the others or has become an industry standard. This brings the need for a classification and comparison of the various control strategies available in the literature to facilitate selection of the most suitable control strategy for a given application. Though the control strategies are different from the perspective of implementation and realization of specific functionalities, they all share one common principle, i.e., the converter should emulate the voltage-source behaviour of the SG [40]. This property is of particular interest for the system operators as it provides grid-supportive responses naturally from the converter without relying on the control actions to take place following a grid disturbance [41]–[43].

However, due to the voltage-source behaviour of the converter, the current exchanged between the converter and the grid is not directly controlled, making its limitation challenging [44], [45]. Various current-limitation strategies have been investigated and reported in the literature. These include strategies mainly based either on a current saturation algorithm (CSA) [46]–[48] or the use of a virtual impedance [49]–[51]. Strategies based on the CSA are vulnerable to loss of synchronizm following a grid disturbance as reported in [52]–[54]. On the other hand, strategies deploying virtual impedance for current limitation require system knowledge and assumptions regarding the worst-case scenario for selecting the parameters of virtual impedance. System conditions differing from those assumptions can result in overcurrent or low

utilization of the converter's fault-current contribution capability [45], while an adaptive virtual impedance can result in system instability [55]. Furthermore, some studies suggest the use of a phase-locked-loop (PLL) during large grid disturbances in order to maintain synchronizm and effectively limit the converter current [33], [56]. However, the use of a PLL can negatively impact the operation of the converter especially during weak grid conditions [57]–[61] and eventually compromise the voltage-source behaviour of the converter. A novel limitation strategy will be proposed in this thesis, which effectively limits the converter current to the desired value without relying on any system knowledge and preserves the converter's GFM properties at all times.

It is clear that providing ancillary services demanding controllable active power (which also defines some of the GFM properties) such as inertial response, frequency support and black-start capability from the wind power plants (WPPs) requires some form of energy storage [62], [63]. Continuous developments and a fast decrease in the costs of various energy storage technologies (ESTs) such as batteries and supercapacitors, along with the advancements in power-electronic technologies have made the integration of energy storage systems (ESS) in WPPs viable [64], [65]. Although the majority of the works available in today's literature focus on the GFM properties of individual ESS, it is unclear how the overall behaviour of WPPs, which typically comprise of VSCs in grid-following (GFL) mode, will be affected if a GFM-ESS is introduced at the grid-connection point of the WPPs. Providing GFM properties through the ESS in this manner can be a fast and feasible solution as it does not require any modifications in the control structure of existing wind turbines (WTs). Moreover, this approach does not interfere with the optimum generation conditions and ensure the availability of various services from the WPPs at all times. Consequently, this thesis will evaluate the potential of an ESS in GFM mode to offer a certain degree of the GFM properties to the overall WPP. For this, an effective GFM control strategy for the ESS will be first developed, which aids the provision of above mentioned services from the WPPs and also improves their transient stability, thereby providing grid-code fulfillment.

1.2 Purpose of the thesis and main contributions

The purpose of this thesis is to investigate the application of GFM control strategies in WPPs. The ultimate goal is to design an effective GFM control strategy, which facilitates the provision of ancillary services such as fast fault-current injection, synthetic inertia support, fast frequency response and active damping power from the WPPs, thereby offering the GFM properties of a conventional SG to the WPPs. To the best of the author's knowledge, the main contributions of the thesis are summarized below.

- Analysis of the active-power controller, which also acts as a synchronization loop of the VSC with the considered GFM control strategies has been made. A modified structure for the active-power controller has been developed, which unlike the more classical structure decouples the damping and steady state frequency-droop characteristics of the converter. Consequently, a higher damping factor can be selected to damp subsynchronous oscillations (SSOs) without affecting the frequency-droop characteristic of the converter.

- A classification and comparison of state-of-the-art GFM control strategies has been performed, which allows selection of the most suitable control strategy based on application. The comparison is based on the ability of the VSC to prevent adverse control interactions and robustness of the controller against large variations in the grid strength. Furthermore, input-admittance model of the converter with various GFM control strategies has been derived, which is useful for small-signal stability analysis of the power system.

- Transient stability problem of the VSCs operated using GFM control strategies (referred here as GFM converters) has been analyzed. A novel current-limitation strategy has been proposed, which guarantees the stability of the converter during severe grid disturbances and preserves its GFM properties at all times. This is achieved by limiting the converter's internal voltage vector (the so called virtual back-electromotive force) instead of relying on a current limiter. To aid in this, a cascaded structure for the active-power controller has been designed, which decouples the synchronization task of and inertia provision from the active-power controller, thereby providing a fast control over the active power output

of the converter.

- From detailed time-domain simulations of a test WPP model, it has been shown that by adopting the proposed GFM control strategy for the ESS of an appropriate size, GFM properties can be offered to the overall WPP. The GFM behaviour of the considered WPP has been verified further by using the recently introduced Network Frequency Perturbation (NFP) plots.

- A coordinated control strategy between the WPP and SGs has been proposed to provide fast frequency response from the WPP. It utilizes the fast dynamic properties of the converter system to keep the instantaneous frequency following an electrical disturbance within the prescribed limits, without deteriorating the performance of the remaining SGs in the grid. This not only improves the frequency quality of the system, but also reduces the energy storage requirements for the converter system.

1.3 Structure of the thesis

The thesis is organized into seven chapters with the first chapter describing the background information, motivation, purpose and main contributions of the thesis. Chapter 2 summarises the definition of the GFM capability provided by various system operators, grid codes and standards. This is followed by a description of the fundamental principle behind the GFM control, classification of GFM control strategies into three types and evaluation of each type. The chapter concludes by making a choice for the most suitable type of the GFM control strategy for a given application. In Chapter 3, the transient stability problem of GFM converters during current limitation is first described. A novel current-limitation strategy and the proposed control structure for the GFM converters is presented next. The effectiveness of the proposed current-limitation strategy is demonstrated using experimental tests. By considering a test WPP model, Chapter 4 assesses the potential of a GFM-ESS to offer a certain degree of the GFM properties to the overall WPP. The methodology to generate the NFP plot and its interpretation are described in detail. The GFM behaviour of the considered WPP is validated using various time-domain simulations and NFP plots. In Chapter 5, recommendations are made for designing and sizing of the two most suitable energy storage technologies

for the GFM converters. A modified control strategy for the supercapacitor-based GFM converters is proposed in this chapter, which allows the provision of synthetic inertia support or fast frequency response from the converter without slowing down the direct-voltage controller. Chapter 6 proposes a coordinated control strategy between the WPP and SGs to facilitate frequency support from the WPP in future power systems. It is shown that a correct tuning of the frequency controller of the ESS facilitates a natural coordination between the WPP and SGs in the grid. The effectiveness of the proposed control strategy is validated using detailed time-domain simulations. Finally, the thesis concludes with a summary of the results obtained and plans for the future work in Chapter 7.

1.4 List of publications

The Ph.D. project has resulted in the following publications which constitute the majority of the thesis.

I. **A. Narula**, P. Imgart, M. Bongiorno, M. Beza, J. R. Svensson and J.-P. Hasler, "Voltage-based Current Limitation Strategy to Preserve Grid-forming Properties Under Severe Grid Disturbances," in *IEEE Open Journal of Power Electronics*, doi: 10.1109/OJPEL.2023.3246728.

II. **A. Narula**, M. Bongiorno, M. Beza, P. Chen, D. Karlsson, "Coordinated control of grid-forming converters and hydro generators to enhance frequency quality of future power system," *Electric Power Systems Research*, vol. 212, Nov. 2022, pp. 108456.

III. P. Imgart, **A. Narula**, M. Bongiorno, M. Beza and J. R. Svensson, "A Cascaded Power Controller for Robust Frequency Ride-Through of Grid-Forming Converters," in *2022 IEEE Energy Conversion Congress and Exposition (ECCE)*, Nov. 2022, pp. 1-8.

IV. **A. Narula**, M. Bongiorno and M. Beza, "Comparison of Grid-Forming Converter Control Strategies," in *2021 IEEE Energy Conversion Congress and Exposition (ECCE)*, Oct. 2021, pp. 361-368.

V. **A. Narula**, M. Bongiorno, M. Beza and P. Chen, "Tuning and evaluation of grid-forming converters for grid-support," in *2021 23rd European*

Conference on Power Electronics and Applications (EPE'21 ECCE Europe), Oct. 2021, pp. P.1-P.10.

VI. M. Beza, M. Bongiorno and **A. Narula**, "Passivity characterization of grid-forming converters with fault-ride through capability," in *2021 23rd European Conference on Power Electronics and Applications (EPE'21 ECCE Europe)*, Oct. 2021, pp. 1-10.

VII. M. Beza, M. Bongiorno, and **A. Narula**, "Impact of Control Loops on the Passivity Properties of Grid-Forming Converters with Fault-Ride through Capability," *Energies*, vol. 14, no. 19, p. 6036, Sep. 2021.

VIII. **A. Narula**, M. Bongiorno, M. Beza, J. R. Svensson, X. Guillaud and L. Harnefors, "Impact of steady-state grid-frequency deviations on the performance of grid-forming converter control strategies," in *2020 22nd European Conference on Power Electronics and Applications (EPE'20 ECCE Europe)*, Sep. 2020, pp. P.1-P.10.

IX. M. Beza, M. Bongiorno and **A. Narula**, "Impact of control loops on the low-frequency passivity properties of grid-forming converters," in *2020 22nd European Conference on Power Electronics and Applications (EPE' 20 ECCE Europe)*, Sep. 2020, pp. P.1-P.10.

The author has also contributed to the following publications which are not included in the thesis.

I. R. Mohanty, P. Chen, L. A. Tuan and **A. Narula**, "Challenges in Protection of Converter Dominated Medium-Voltage Microgrids," in *2019 IEEE PES Innovative Smart Grid Technologies Europe (ISGT-Europe)*, Oct. 2019, pp. 1-5.

II. L. Bessegato, **A. Narula**, P. Bakas and S. Norrga, "Design of a Modular Multilevel Converter Prototype for Research Purposes," in *2018 20th European Conference on Power Electronics and Applications (EPE'18 ECCE Europe)*, Sep. 2018, pp. P.1-P.10.

CHAPTER 2

Grid-forming control for grid-connected converter systems

2.1 Introduction

One of the fundamental objectives of a voltage-source converter (VSC) connected to an ac grid is to convert the dc into ac power and vice versa based on the direction of the desired power flow. In order to achieve this goal, the majority of the grid-connected converter systems use the conventional grid-following (GFL) control, based on the vector-current controller (VCC) [66]. Such converter systems rely on a fast-acting synchronization mechanism, typically using a PLL, to inject (or absorb) the desired amount of active and reactive power to (or from) the grid. In the classical GFL control, a PLL estimates the grid-voltage angle at the point-of-common-coupling (PCC), which is used to calculate the active and reactive component (reflecting active and reactive power, respectively) of the output current supplied by the converter. In other words, the controller adapts itself to "follow" the measured grid voltage, modelling the converter system as a controllable current source [67]. This implies that if the grid-voltage angle cannot be tracked accurately and quickly (as in weak grids, for instance), stable operation of the converter system might be compromised.

In the past decade, the continuous increase in the penetration level of converter-interfaced RES has led to a reduction in the number of SGs connected to the power system. Consequently, the grid strength (in terms of the short-circuit capacity and total system inertia) has reduced [7], and the risk of instability in converter systems has increased. Furthermore, there is a need to provide system services that were originally provided by synchronous generators such as frequency support, contribution to total system inertia, fast fault-current injection, black-start capability, etc., from the converter systems. To maintain the grid stability and reliability, grid codes and standards for converter systems have been developed and requirements of capability for the aforementioned services (sometimes referred as grid-forming capability) are today included in several interconnection standards [13]–[17], [68].

To begin with, this chapter briefly presents a state-of-the-art definition of the grid-forming capability based on the available grid codes, standards and guidelines from different system operators. This is followed by the description of the concept of GFM control. To select the most suitable GFM control strategy that can be used later in this thesis, a comparative study of various GFM control strategies available in the literature [30], [33]–[36], [40], [69], [70] is performed next. The considered GFM control strategies are here broadly classified into three categories; namely, Direct Control of Converter Voltage (DCCV), Cascaded Vector-Control (CVC), and Virtual-Admittance Based Control (VABC). This classification is based on the identification of fundamental differences in their control structure. The GFM control strategies are evaluated and compared based on the ability of the grid-connected converter system to prevent adverse control interactions. For this, the frequency-dependent input admittance of the converter system is used, which is first derived analytically and then verified using detailed simulation models. Furthermore, the robustness of the control system against large variations in the short-circuit ratio (SCR) of the grid at the PCC is also investigated.

2.2 Definition of grid-forming capability

Recently, system operators in the UK, Germany and in general across Europe (through the European Network of Transmission System Operators for Electricity, ENTSO-e) have identified several key features of the GFM capability of a converter [7], [17], [71]. Some of the common key features facilitate pro-

vision of a similar (or better) performance as that of a synchronous generator from the converter systems, in terms of supporting the grid during disturbances. Accordingly, a converter system with GFM capability (referred here as a GFM converter system[1]) should be able to

- Create or form the system voltage: This implies that a GFM converter system should be able to maintain its internal voltage in terms of its amplitude, frequency and phase angle irrespective of the load connected to it. It also means that operation of such converter systems should not rely on being provided with a firm clean voltage.
- Contribute to fault level (short-circuit power): This refers to the fault-current contribution of GFM converter systems which requires them to inject fault current up to their over-current capacity within the first quarter of a cycle (5 ms).
- Contribute to the total system inertia: This implies that during frequency disturbances in the grid, a GFM converter system should be able to provide an active-power response proportional to rate-of-change-of-frequency (RoCoF), thereby contributing to the total system inertia. However, this requirement is limited by the energy storage capacity and the available power rating of the GFM converter system.
- Contribute to the system damping: This implies that a GFM converter system should respond naturally, within 5 ms, to damp low-frequency oscillations in the system, without actions being required in the control system.
- Act as a sink to counteract harmonics and unbalances in the grid voltage: It implies that a GFM converter system should provide a damped response in the harmonic frequency range using harmonic current flow, with the effect of an improved voltage quality at the PCC. Thus, the GFM converter system should impose an inductive or inductive-resistive behaviour towards the grid.
- Prevent adverse control interactions: This requires a GFM converter system to impose a resistive behaviour over a wide range of frequency.

[1]GFM converter system can be an individual converter system or group of converter systems with GFM capability.

This is due to the fact that if the natural frequencies of the network appear within a region in which the GFM converter system presents a negative resistance behaviour, an instability might be triggered if the network itself does not provide enough damping to compensate.

Furthermore, the National Grid Code GC0137 provides quantitative requirements with regard to various withstand capabilities for the GFM converter systems [17]. For instance, it specifies that a GFM converter system should be designed to withstand ±2.0 Hz/s RoCoF and ±60° phase-angle jump without tripping offline. Furthermore, a minimum phase-angle jump limit of ±5° and RoCoF limit of ±1.0 Hz/s is recommended for a GFM converter system to remain in linear control mode without entering into current limitation. Additionally, GC0137 suggests GFM converter systems to contribute positively towards system damping, with a damping factor between 0.2 and 1.0. To ensure an adequate level of damping, contribution to inertia and a GFM behaviour of a converter system, the National Grid Electricity System Operator (National Grid ESO) recommends the use of Network Frequency Perturbation (NFP) plots. Details related to the NFP plot are discussed in Chapter 4.

2.3 Grid-forming principle and the proposed active-power controller

Figure 2.1(a) shows a generic GFM control structure for a grid-connected converter system, where the ac grid is represented by its Thévenin's equivalent. The fundamental property of the GFM control strategy is that it models the converter system as a controllable voltage-source behind an impedance[2] (see Fig. 2.1(b)) [67]. This is because, unlike the classical GFL control, the outer loops in a GFM control directly calculate a reference voltage for the emulated voltage source. Another property that characterizes the majority of GFM control strategies is that grid synchronization is provided through the active-power controller. Therefore, the synchronization of the converter system to the ac grid is achieved by means of transient power transfer. As seen from Fig. 2.1(a), the active-power controller provides the synchronization angle, θ_c, for the converter system, thereby eliminating the need for a dedicated

[2]This represents the equivalent impedance between the emulated voltage source and PCC.

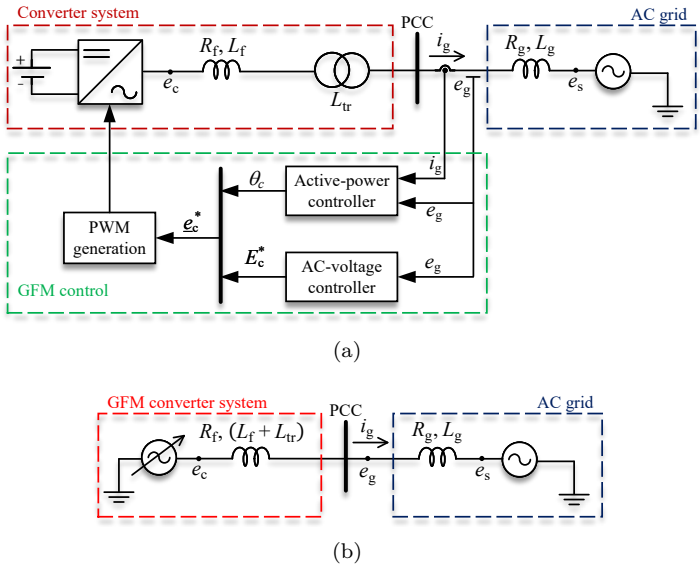

Figure 2.1: (a) A generic GFM control structure for a grid-connected VSC. b) An equivalent circuit representation of a GFM converter system.

synchronization unit like a PLL. Hence, the active-power controller also acts as the synchronization loop for GFM converter systems.

In this section, one of the first and simplest structures (referred here as the classical structure) for the active-power controller of GFM converter systems is presented. This is followed by the description of the issues related to the classical structure and the proposed solution.

2.3.1 Classical structure of the active-power controller

The classical structure of the active-power controller for the GFM converter systems is based on a direct emulation of the electro-mechanical dynamics of a SG [34]. Accordingly, the synchronization angle for the converter system is obtained as

$$\theta_c = \frac{\omega_c}{s} = \frac{1}{s}[\omega_N + \frac{1}{sM + \frac{K_D S_N}{\omega_N}}(P_g^\star - P_g)]; \quad \text{with} \quad M = \frac{2HS_N}{\omega_N}, \tag{2.1}$$

where ω_{c} denotes the internal angular frequency (in rad/s) of the converter system, ω_{N} and S_{N} are the rated angular frequency (in rad/s) of the ac grid and rated power of the converter, respectively, H and K_{D} represents the virtual inertia time-constant (in s) and virtual mechanical-damping coefficient (in pu) of the converter system, respectively. The term s is the Laplace-transform variable, which should be interpreted as d/dt wherever appropriate and "$\star$" denotes a reference signal in the notations. Assuming a lossless filter reactor and an inductive grid, the active-power output of the converter system in quasi-steady state, P_{g}, is given by

$$P_{\mathrm{g}} = \frac{E_{\mathrm{c}} E_{\mathrm{s}}}{X_{\mathrm{f}} + X_{\mathrm{tr}} + X_{\mathrm{g}}} \sin\theta_{\mathrm{L}}; \quad \text{with} \quad \theta_{\mathrm{L}} = \theta_{\mathrm{c}} - \theta_{\mathrm{s}}, \tag{2.2}$$

where E_{c} and E_{s} represent the voltage magnitudes at the terminals of the converter and the ideal-voltage source, respectively. The terms X_{f}, X_{tr} and X_{g} are the filter, transformer leakage and grid reactances, respectively; whereas, θ_{s} denotes the voltage angle of the ideal-voltage source.

In a GFM converter system, H can be selected freely based on the desired amount of synthetic inertia from the converter system. The upper limit of H is dependent on the power ratings and energy storage capacity of the converter system. Furthermore, K_{D} being a control parameter can be selected based on the desired damping ratio, ζ, of the second-order response from the reference to actual active-power output of the converter system. From the small-signal models of (2.1) and (2.2), the closed-loop transfer function from the reference to actual active-power output of the converter system is obtained as

$$\frac{\Delta P_{\mathrm{g}}}{\Delta P_{\mathrm{g}}^{\star}} = \frac{\frac{\omega_{\mathrm{N}} K_{\mathrm{s}}}{2H}}{s^2 + \frac{K_{\mathrm{D}}}{2H} s + \frac{\omega_{\mathrm{N}} K_{\mathrm{s}}}{2H}} = \frac{\omega_{\mathrm{n}}^2}{s^2 + 2\zeta\omega_{\mathrm{n}} s + \omega_{\mathrm{n}}^2}. \tag{2.3}$$

With θ_{L0} representing the converter's load angle in steady state, the synchronizing power coefficient, K_{s}, is given by

$$K_{\mathrm{s}} = \frac{E_{\mathrm{c}} E_{\mathrm{s}}}{X_{\mathrm{f}} + X_{\mathrm{tr}} + X_{\mathrm{g}}} \cos\theta_{\mathrm{L0}}.$$

From (2.3), the virtual mechanical damping coefficient can be calculated as

$$K_{\mathrm{D}} = 2\zeta\omega_{\mathrm{N}} \sqrt{K_{\mathrm{s}} M}. \tag{2.4}$$

In order to guarantee the desired speed of response for all grid conditions, X_{g} is typically set for the strongest grid strength provided by the system operator [72].

2.3.2 Impact of steady-state grid-frequency deviation on the classical structure

The issues related to the classical structure of the active-power controller during steady-state deviation in the grid frequency are investigated here. By substituting $s = 0$ in (2.1) and rearranging the terms, the equation for the active-power flow from the converter system in steady state is obtained as

$$P_{\mathrm{g}} = P_{\mathrm{g}}^{\star} + \frac{K_{\mathrm{D}} S_{\mathrm{N}}}{\omega_{\mathrm{N}}}(\omega_{\mathrm{N}} - \omega_{\mathrm{c}}). \tag{2.5}$$

During steady state, ω_{c} is equal to the angular frequency of the grid, ω_{g}. Therefore, from (2.5) it can be observed that if the grid frequency is at its rated value during steady state, $P_{\mathrm{g}} = P_{\mathrm{g}}^{\star}$. However, a grid-frequency deviation in steady state will lead to an active-power deviation, resulting in an uncontrolled droop effect. Denoted by $P_{\mathrm{e}} = \frac{(P_{\mathrm{g}} - P_{\mathrm{g}}^{\star})}{S_{\mathrm{N}}}$, the steady state active-power deviation is given by

$$P_{\mathrm{e}} = K_{\mathrm{D}} \omega_{\mathrm{e}}. \tag{2.6}$$

It can be observed from (2.6) that P_{e} is directly proportional to K_{D} and the deviation in the grid frequency, $\omega_{\mathrm{e}} = \frac{(\omega_{\mathrm{N}} - \omega_{\mathrm{g}})}{\omega_{\mathrm{N}}}$. For a GFM converter system, the value of K_{D} can be large depending upon the desired H and ζ. For instance, with $\zeta = 0.707$, $H = 5$ s, $X_{\mathrm{f}} = 0.05$ pu and $X_{\mathrm{tr}} = 0.1$ pu, (2.4) results in $K_{\mathrm{D}} \approx 205$ pu. This implies that even very small deviations in the grid frequency from the rated value will lead to large deviations of the active power from the desired value; for example, according with (2.6) a 0.2% grid-frequency deviation will result in $P_{\mathrm{e}} \approx 0.4$ pu. Such large deviations in active power are problematic for converter systems with limited active-power injection capability and energy storage capacity.

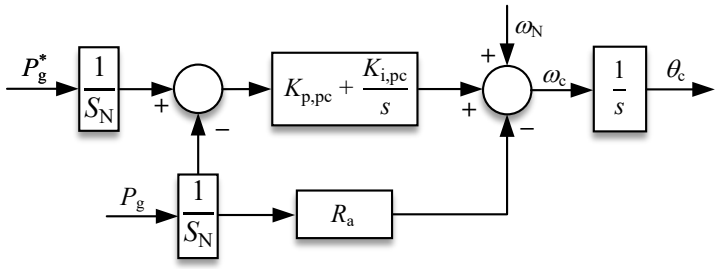

Figure 2.2: Block scheme of the proposed active-power controller for GFM converter systems.

2.3.3 Proposed modification in the active-power controller

To avoid the steady-state error in the active power output of the converter system, an integrator should be added in the active-power controller [73]. This can be achieved by feed-forwarding the grid-frequency estimate from a PLL [74] or by using a proportional-integral (PI) regulator in the active-power controller. The latter is used in this thesis to avoid the use of a PLL in the synchronization loop of GFM converter systems.

Figure 2.2 shows the block diagram of the proposed structure for the active-power controller. It consists of a PI regulator for accurate reference tracking and an active-damping term, R_a, to improve the controller's dynamic performance. This control structure is inspired by the design of two-degree-of-freedom current controller proposed in [75]. The synchronization angle in this case is obtained by

$$\theta_c = \frac{\omega_c}{s} = \frac{1}{s}[(K_{p,pc} + \frac{K_{i,pc}}{s})\frac{(P_g^\star - P_g)}{S_N} - R_a\frac{P_g}{S_N} + \omega_N], \tag{2.7}$$

where $K_{p,pc}$ and $K_{i,pc}$ are the proportional and integrals gains, respectively, of the PI regulator. Using small-signal models of (2.2) and (2.7), the closed-loop transfer function from the reference to actual active-power output of the converter system is given by

$$\frac{\Delta P_g}{\Delta P_g^\star} = \frac{K_{p,pc}s + K_{i,pc}}{\frac{S_N}{K_s}s^2 + (K_{p,pc} + R_a)s + K_{i,pc}}. \tag{2.8}$$

The existence of the zero will lead to a pronounced overshoot in the step response [76]. By proper selection of the controller's gains and the active-damping term, a pole-zero cancellation can be achieved, thereby reducing the system to first order. Accordingly, the parameters of the active-power controller are selected as

$$K_{\mathrm{p,pc}} = \frac{\alpha_{\mathrm{pc}}}{K_{\mathrm{s}}} S_{\mathrm{N}}, \quad K_{\mathrm{i,pc}} = \frac{\alpha_{\mathrm{pc}}^2}{K_{\mathrm{s}}} S_{\mathrm{N}}, \quad \text{and} \quad R_{\mathrm{a}} = K_{\mathrm{p,pc}}, \tag{2.9}$$

which results in

$$\frac{\Delta P_{\mathrm{g}}}{\Delta P_{\mathrm{g}}^{\star}} = \frac{\alpha_{\mathrm{pc}}}{s + \alpha_{\mathrm{pc}}}, \tag{2.10}$$

with α_{pc} the loop bandwidth (in rad/s) of the active-power controller. By equating the closed-loop bandwidths of the two transfer functions, (2.3)[3] and (2.10), α_{pc} can be related to the virtual inertia constant as

$$\alpha_{\mathrm{pc}} = \sqrt{\frac{K_{\mathrm{s}} \omega_{\mathrm{N}}}{2H}}. \tag{2.11}$$

2.4 Grid-forming control strategies and system modeling

In this section, the three major types of GFM control strategies are presented. The structural differences between the considered GFM control strategies are described and the corresponding input-admittance model of the converter system is derived. All controllers described here are designed in the rotating *dq*-reference frame, using power-invariant transformation, which is defined by the angle output of the active-power controller. For a fair comparison, the same active-power controller as described in Section 2.3.3 is used in all GFM control strategies. Furthermore, a stiff voltage at the dc side of the converter system is assumed; hence, the dynamics of the dc-link voltage controller are not included in the analysis.

[3] For a well damped second-order system, the closed-loop bandwidth can be approximated to the natural frequency, ω_{n}.

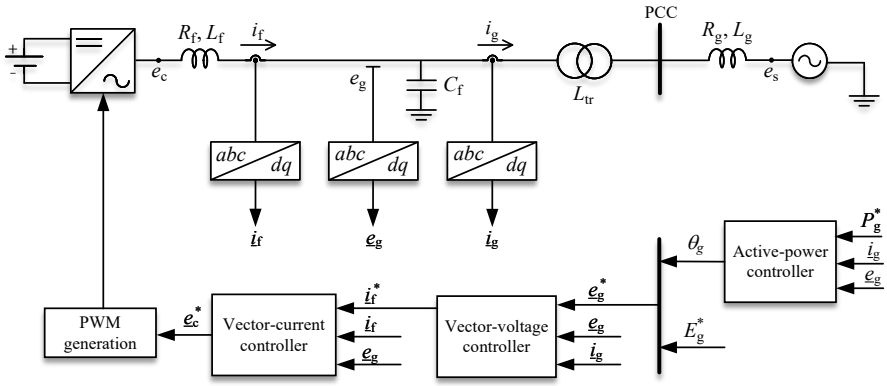

Figure 2.3: Single-line diagram of a grid-connected VSC and block scheme of CVC.

2.4.1 Cascaded vector-control (CVC)

The single-line diagram of a grid-connected VSC with cascaded vector-control (CVC) is shown in Fig. 2.3. The converter is connected to the grid through an RLC filter of resistance, R_f, inductance, L_f (inductive reactance, X_f), and shunt capacitance, C_f, and a lossless transformer with leakage inductance, L_{tr} (leakage reactance, X_{tr}). The grid model comprises of an ideal-voltage source, e_s, behind a grid impedance of resistance, R_g, and inductance, L_g (inductive reactance, X_g). The voltage across the filter capacitor is denoted by e_g, while the voltage at the converter's terminal is denoted by e_c. The quantities i_f and i_g denote the current flowing through the converter and into the grid, respectively; P_g and Q_g represent the active and reactive powers exchanged between the converter and the grid, respectively.

The CVC shown in Fig. 2.3 is similar to the one proposed in [35], [77]. In this type of control, the active-power controller calculates the capacitor-voltage angle, θ_g. As the outer loops in CVC directly calculate the reference value of the capacitor-voltage vector, $\underline{e}_g^\star$, the grid-forming property[4] is offered at the connection point of the filter capacitor in this case. The vector-voltage controller is used to regulate the capacitor-voltage vector and calculate the ref-

[4]The point where the voltage vector is actuated is used to define the grid-forming property of the converter.

erence current, $\underline{i}_{\mathrm{f}}^{\star}$, for the inner-current controller. Finally, the inner-current controller regulates the current flowing through the converter and calculates the reference voltage, $\underline{e}_{\mathrm{c}}^{\star}$, for the modulation stage of the converter.

Vector-current controller

The implemented current controller has a classical structure and is based on a PI regulator with cross-coupling cancellation and voltage feed-forward that is low-pass filtered with a closed-loop bandwidth of α_{ff}. The current controller calculates the converter-voltage reference as

$$\underline{e}_{\mathrm{c}}^{\star} = \overbrace{\frac{\alpha_{\mathrm{ff}}}{s+\alpha_{\mathrm{ff}}}}^{H_{\mathrm{ff}}} \underline{e}_{\mathrm{g}} + j\omega_{\mathrm{N}} L_{\mathrm{f}} \underline{i}_{\mathrm{f}} + \overbrace{(K_{\mathrm{p,cc}} + \frac{K_{\mathrm{i,cc}}}{s})}^{G_{\mathrm{cc}}} (\underline{i}_{\mathrm{f}}^{\star} - \underline{i}_{\mathrm{f}}). \tag{2.12}$$

$K_{\mathrm{p,cc}}$, $K_{\mathrm{i,cc}}$ denote the proportional and integral gains of the PI regulator for the current controller, respectively.

The converter current can be expressed in terms of the grid current and capacitor voltage as

$$\underline{i}_{\mathrm{f}} = \underline{i}_{\mathrm{g}} + j\omega_{\mathrm{N}} C_{\mathrm{f}} \underline{e}_{\mathrm{g}} + sC_{\mathrm{f}} \underline{e}_{\mathrm{g}}. \tag{2.13}$$

Vector-voltage controller

The vector-voltage controller calculates the reference value of the current for the inner-current controller as

$$\underline{i}_{\mathrm{f}}^{\star} = \underline{i}_{\mathrm{g}} + j\omega_{\mathrm{N}} C_{\mathrm{f}} \underline{e}_{\mathrm{g}} + \overbrace{(K_{\mathrm{p,vc}} + \frac{K_{\mathrm{i,vc}}}{s})}^{G_{\mathrm{vc}}} (\underline{e}_{\mathrm{g}}^{\star} - \underline{e}_{\mathrm{g}}), \tag{2.14}$$

where $K_{\mathrm{p,vc}}$, $K_{\mathrm{i,vc}}$ denote the proportional and integral gains of the PI regulator for the vector-voltage controller, respectively. The gains of the vector-voltage and current controllers are selected in accordance to the recommendations given in [77].

To allow operation of the converter in strong grids and alongside other converters, a reactive-droop model is used for the vector-voltage controller. Accordingly, the reference value of the capacitor-voltage vector is calculated

as

$$\underline{e}_{\mathrm{g}}^{\star} = E_{\mathrm{set}} - \frac{K_{\mathrm{d,vc}} Q_{\mathrm{g}}}{I_{\mathrm{base}}} = E_{\mathrm{g}}^{\star} \quad \text{with} \quad I_{\mathrm{base}} = \frac{S_{\mathrm{N}}}{E_{\mathrm{N}}}. \tag{2.15}$$

E_{set} denotes the desired set-point of the capacitor-voltage magnitude, $K_{\mathrm{d,vc}}$ represents the droop constant (in pu) and E_{N} is the rated line-to-line voltage of the converter.

Active-power controller

The active-power controller calculates the capacitor-voltage angle as

$$\theta_{\mathrm{g}} = \frac{1}{s}[\overbrace{(K_{\mathrm{p,pc}} + \frac{K_{\mathrm{i,pc}}}{s})}^{G_{\mathrm{pc}}} \frac{(P_{\mathrm{g}}^{\star} - P_{\mathrm{g}}}{S_{\mathrm{N}}}) - R_{\mathrm{a}} \frac{P_{\mathrm{g}}}{S_{\mathrm{N}}} + \omega_{\mathrm{N}}], \tag{2.16}$$

The gains of the PI regulator are selected in accordance to (2.9), with the synchronizing power coefficient, K_{s}, for this case given by

$$K_{\mathrm{s}} = \frac{E_{\mathrm{g}} E_{\mathrm{s}}}{(X_{\mathrm{tr}} + X_{\mathrm{g}})}. \tag{2.17}$$

Input-admittance derivation

The concept of input admittance is useful for modeling of three-phase systems (especially, those systems that comprise of power-electronics based devices), as it provides the ability to independently investigate the impact of each device on the overall system stability [78]. For a generic three-phase system as the one shown in Fig. 2.4, the frequency dependent input-admittance matrix, $\mathbf{Y}(s)$ is defined as

$$\begin{bmatrix} i^d(s) \\ i^q(s) \end{bmatrix} = \mathbf{Y}(s) \begin{bmatrix} e^d(s) \\ e^q(s) \end{bmatrix}, \quad \text{with} \quad \mathbf{Y}(s) = \begin{bmatrix} Y_{\mathrm{dd}}(s) & Y_{\mathrm{dq}}(s) \\ Y_{\mathrm{qd}}(s) & Y_{\mathrm{qq}}(s) \end{bmatrix}, \tag{2.18}$$

where i^d, i^q and e^d, e^q represent the dq components of the current and voltage vectors, respectively. Due to the presence of active-power and ac-voltage

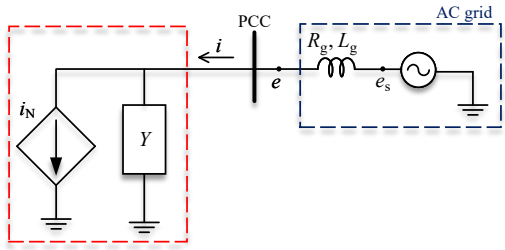

Figure 2.4: Norton's equivalent representation of a generic three-phase grid-connected system.

controllers, the input-admittance matrix of the converter is not symmetric[5] in the low-frequency range and is derived as described below.

In order to account for the dynamics of the active-power controller in the system model, the input admittance of the converter is derived in a rotating *dq*-frame, which is defined by the angle θ_N, obtained by integrating the rated angular frequency, ω_N, and having a zero initial phase. For this, the controller dynamics described above should be transformed to this frame (referred here as *source dq-frame*). It can be observed from (2.16) that the angle θ_N is given by

$$\theta_N = \theta_g - \theta_L, \quad \text{with} \quad \theta_L = \frac{1}{s}\frac{[G_{pc}(P_g^\star - P_g) - R_a P_g]}{S_N}, \tag{2.19}$$

where θ_L represents the phase-angle difference between the emulated-voltage source and the ideal-voltage source, and can be interpreted as the converter's load angle. Thus, any space-vector $\underline{y}$ defined earlier can be transformed to the *source dq-frame* using the following relation

$$\underline{z} = \underline{y} e^{j\theta_L}. \tag{2.20}$$

In order to derive the input admittance, the small-signal model of the capacitor-voltage reference is expressed in terms of the scalar components of capacitor-voltage (e_g^d, e_g^q) and grid current (i_g^d, i_g^q) using (2.15), (2.19), and

[5] A transfer matrix, $\mathbf{F}(s)$, is symmetric if it can be expressed in the form $\mathbf{F}(s) = \begin{bmatrix} F_{11}(s) & -F_{21}(s) \\ F_{21}(s) & F_{11}(s) \end{bmatrix}$

(2.20) as

$$\begin{bmatrix}\Delta e_{\mathrm{g}}^{d\star}\\ \Delta e_{\mathrm{g}}^{q\star}\end{bmatrix} = \overbrace{\begin{bmatrix}-e_{\mathrm{g0}}^{q\star} & \cos\theta_{\mathrm{L0}}\\ e_{\mathrm{g0}}^{d\star} & \sin\theta_{\mathrm{L0}}\end{bmatrix}}^{G_{\mathrm{T}}}\begin{bmatrix}\Delta\theta_{\mathrm{L}}\\ \Delta E_{\mathrm{set}}\end{bmatrix} + \overbrace{\begin{bmatrix}-\frac{K_{\mathrm{d,vc}}}{I_{\mathrm{base}}}\cos\theta_{\mathrm{L0}}e_{\mathrm{g0}}^{q} & \frac{K_{\mathrm{d,vc}}}{I_{\mathrm{base}}}\cos\theta_{\mathrm{L0}}e_{\mathrm{g0}}^{d}\\ -\frac{K_{\mathrm{d,vc}}}{I_{\mathrm{base}}}\sin\theta_{\mathrm{L0}}e_{\mathrm{g0}}^{q} & \frac{K_{\mathrm{d,vc}}}{I_{\mathrm{base}}}\sin\theta_{\mathrm{L0}}e_{\mathrm{g0}}^{d}\end{bmatrix}}^{G_{\mathrm{PVc1}}} \tag{2.21}$$
$$\begin{bmatrix}\Delta i_{\mathrm{g}}^{d}\\ \Delta i_{\mathrm{g}}^{q}\end{bmatrix} + \overbrace{\begin{bmatrix}\frac{K_{\mathrm{d,vc}}}{I_{\mathrm{base}}}\cos\theta_{\mathrm{L0}}i_{\mathrm{g0}}^{q} & -\frac{K_{\mathrm{d,vc}}}{I_{\mathrm{base}}}\cos\theta_{\mathrm{L0}}i_{\mathrm{g0}}^{d}\\ \frac{K_{\mathrm{d,vc}}}{I_{\mathrm{base}}}\sin\theta_{\mathrm{L0}}i_{\mathrm{g0}}^{q} & -\frac{K_{\mathrm{d,vc}}}{I_{\mathrm{base}}}\sin\theta_{\mathrm{L0}}i_{\mathrm{g0}}^{d}\end{bmatrix}}^{G_{\mathrm{PVv1}}}\begin{bmatrix}\Delta e_{\mathrm{g}}^{d}\\ \Delta e_{\mathrm{g}}^{q}\end{bmatrix},$$

with

$$\begin{bmatrix}\Delta\theta_{\mathrm{L}}\\ \Delta E_{\mathrm{set}}\end{bmatrix} = \begin{bmatrix}\frac{G_{\mathrm{pc}}}{sS_{\mathrm{N}}} & 0\\ 0 & 1\end{bmatrix}\begin{bmatrix}\Delta P_{\mathrm{g}}^{\star}\\ \Delta E_{\mathrm{set}}\end{bmatrix} + \overbrace{\begin{bmatrix}-\frac{(G_{\mathrm{pc}}+R_{\mathrm{a}})e_{\mathrm{g0}}^{d}}{sS_{\mathrm{N}}} & -\frac{(G_{\mathrm{pc}}+R_{\mathrm{a}})e_{\mathrm{g0}}^{q}}{sS_{\mathrm{N}}}\\ 0 & 0\end{bmatrix}}^{\mathbf{G}_{\mathrm{PVc2}}} \tag{2.22}$$
$$\begin{bmatrix}\Delta i_{\mathrm{g}}^{d}\\ \Delta i_{\mathrm{g}}^{q}\end{bmatrix} + \overbrace{\begin{bmatrix}-\frac{(G_{\mathrm{pc}}+R_{\mathrm{a}})i_{\mathrm{g0}}^{d}}{sS_{\mathrm{N}}} & -\frac{(G_{\mathrm{pc}}+R_{\mathrm{a}})i_{\mathrm{g0}}^{q}}{sS_{\mathrm{N}}}\\ 0 & 0\end{bmatrix}}^{\mathbf{G}_{\mathrm{PVv2}}}\begin{bmatrix}\Delta e_{\mathrm{g}}^{d}\\ \Delta e_{\mathrm{g}}^{q}\end{bmatrix},$$

where the expression $P_{\mathrm{g}} = e_{\mathrm{g}}^{d}i_{\mathrm{g}}^{d} + e_{\mathrm{g}}^{q}i_{\mathrm{g}}^{q}$, and $Q_{\mathrm{g}} = -e_{\mathrm{g}}^{d}i_{\mathrm{g}}^{q} + e_{\mathrm{g}}^{q}i_{\mathrm{g}}^{d}$ are used for the active and reactive powers injected to the grid, respectively. Note that "Δ" denotes small-signal perturbations around the steady-state quantities represented by the subscript "0" in the notations.

The current dynamics in the *source dq-frame* are given by

$$\underline{e}_{\mathrm{c}} = \underline{e}_{\mathrm{g}} + j\omega_{\mathrm{N}}L_{\mathrm{f}}\underline{i}_{\mathrm{f}} + R_{\mathrm{f}}\underline{i}_{\mathrm{f}} + sL_{\mathrm{f}}\underline{i}_{\mathrm{f}}. \tag{2.23}$$

As the focus here is mainly on the frequency characteristics of the converter at low frequencies (between 0-100 Hz in the rotating *dq*-frame), the impact of delays arising due to the discretization of measured quantities and that due to the modulation stage can be neglected [79]. Hence, the converter-output voltage, $\underline{e}_{\mathrm{c}}$, is given by

$$\underline{e}_{\mathrm{c}} = \underline{e}_{\mathrm{c}}^{\star}. \tag{2.24}$$

Now, using the small-signal models for (2.12), (2.13), (2.14), (2.23) and (2.24), and using (2.20), (2.21) and (2.22), the input admittance of the converter,

$\mathbf{Y}_{\text{conv}}$, in the *source dq-frame* is derived as[6]

$$\begin{bmatrix}\Delta i_{\text{g}}^{d}\\ \Delta i_{\text{g}}^{q}\end{bmatrix} = \mathbf{G}_{\text{conv}}\begin{bmatrix}\Delta P_{\text{g}}^{\star}\\ \Delta E_{\text{set}}\end{bmatrix} - \mathbf{Y}_{\text{conv}}\begin{bmatrix}\Delta e_{\text{g}}^{d}\\ \Delta e_{\text{g}}^{q}\end{bmatrix}, \tag{2.25}$$

where $\mathbf{Y}_{\text{conv}}$ is given by

$$\begin{aligned}\mathbf{Y}_{\text{conv}} =&[I - \mathbf{G}_{\text{c,mat}}(G_{\text{vc}}(G_{\text{T}}\mathbf{G}_{\text{PVc2}} + G_{\text{PVc1}}) + I)]^{-1}\\ &[\mathbf{G}_{\text{cap}} + \mathbf{Y}_{\text{i,mat}} - \mathbf{G}_{\text{c,mat}}(G_{\text{vc}}(G_{\text{T}}\mathbf{G}_{\text{PVv2}} + G_{\text{PVv1}}) + \mathbf{G}_{\text{DC}})],\end{aligned} \tag{2.26}$$

and I represents the identity matrix. Transfer function matrices $\mathbf{G}_{\text{c,mat}}$, $\mathbf{Y}_{\text{i,mat}}$, $\mathbf{G}_{\text{cap}}$, and $\mathbf{G}_{\text{DC}}$ are given by

$$\begin{aligned}\mathbf{G}_{\text{c,mat}} &= G_{\text{cc}}\begin{bmatrix}\frac{1}{sL_{\text{f}}+R_{\text{f}}+G_{\text{cc}}} & 0\\ 0 & \frac{1}{sL_{\text{f}}+R_{\text{f}}+G_{\text{cc}}}\end{bmatrix},\\ \mathbf{Y}_{\text{i,mat}} &= (1-H_{\text{ff}})\begin{bmatrix}\frac{1}{sL_{\text{f}}+R_{\text{f}}+G_{\text{cc}}} & 0\\ 0 & \frac{1}{sL_{\text{f}}+R_{\text{f}}+G_{\text{cc}}}\end{bmatrix},\\ \mathbf{G}_{\text{cap}} &= \begin{bmatrix}sC_{\text{f}} & -\omega_{\text{N}}C_{\text{f}}\\ \omega_{\text{N}}C_{\text{f}} & sC_{\text{f}}\end{bmatrix},\\ \mathbf{G}_{\text{DC}} &= \begin{bmatrix}-G_{\text{vc}} & -\omega_{\text{N}}C_{\text{f}}\\ \omega_{\text{N}}C_{\text{f}} & -G_{\text{vc}}\end{bmatrix}.\end{aligned}$$

Input admittance verification

To verify the analytically derived $\mathbf{Y}_{\text{conv}}$, a detailed PSCAD/EMTDC time-domain simulation of the grid-connected converter system shown in Fig. 2.3, including all control loops (implemented in discrete time) is used. The method presented in [80] is adopted to extract the admittance matrix of the converter system from the simulation model. For this, a stiff-grid connection (i.e., $L_{\text{g}} = R_{\text{g}} = 0$) is assumed, and a perturbation is made on the grid voltage at various frequencies. For each perturbation, the resulting perturbations in the *dq*-components of the grid current are measured and the input-admittance matrix of the grid-connected converter system as seen from the PCC, $\mathbf{Y}_{\text{PCC}}$, is extracted using Discrete Fourier Transform (DFT) calculations. Using the

[6]Since the direction of current flowing out of the converter in Fig.2.3 is taken as positive, the negative sign for $\mathbf{Y}_{\text{conv}}$ is used in (2.25).

Table 2.1: System and control parameters for CVC

System parameters		Control parameters	
S_{N}	100 MVA (1.0 pu)	α_{ff}	$2\pi500$ rad/s
E_{N}	20 kV (1.0 pu)	$K_{\mathrm{p,cc}}$	0.73 pu
ω_{N}	314.16 rad/s	$K_{\mathrm{i,cc}}$	1.19 pu
R_{f}	0.015 pu	$K_{\mathrm{p,vc}}$	0.104 pu
L_{f}	0.15 pu	$K_{\mathrm{i,vc}}$	0.232 pu
C_{f}	0.066 pu	$K_{\mathrm{d,vc}}$	0.05 pu
L_{tr}	0.15 pu	α_{pc}	$2\pi5$ rad/s

analytical model, $\mathbf{Y}_{\mathrm{PCC}}$ is calculated as

$$\mathbf{Y}_{\mathrm{PCC}} = [\mathbf{Y}_{\mathrm{conv}}^{-1} + \mathbf{Z}_{\mathrm{tr}}]^{-1} \quad \text{with} \quad \mathbf{Z}_{\mathrm{tr}} = \begin{bmatrix} sL_{\mathrm{tr}} & -\omega_{\mathrm{N}}L_{\mathrm{tr}} \\ \omega_{\mathrm{N}}L_{\mathrm{tr}} & sL_{\mathrm{tr}} \end{bmatrix}.$$

The system and control parameters used for the simulation tests are given in Table 2.1. The simulation tests are performed with the converter transferring 0.5 pu active power and the capacitor voltage being regulated at 1.0 pu. Figure 2.5 show the frequency response of the magnitude and phase of the four elements of $\mathbf{Y}_{\mathrm{PCC}}$ obtained analytically (solid-blue curves) and from the detailed simulation model (dotted-red curves). One aspect to highlight here is the frequency axis, which corresponds to the frequencies in the rotating *dq*-frame. The results show a very good match between the simulation and the analytical frequency characteristics, verifying the validity of the analytical model.

2.4.2 Direct control of converter voltage (DCCV)

Figure 2.6 shows the block scheme of DCCV, whose structure is similar to the Power Synchronization Control proposed in [30], [33]. Usually, the filter capacitor is not considered with this type of control strategy; however, it is here included for the fairness in comparison with CVC. In this type of control strategy, the ac-voltage controller typically regulates the magnitude of the voltage at the PCC and calculates the reference value of the converter-voltage magnitude; the active-power controller calculates the converter-voltage angle, θ_{c}. As the outer loops directly calculate the reference value of the converter-voltage vector, the grid-forming property is offered at the terminals of the converter

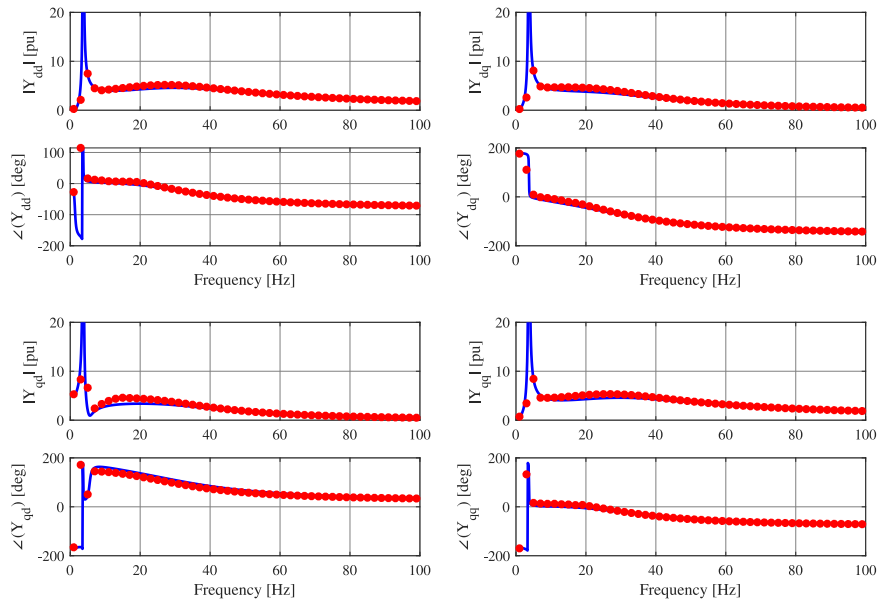

Figure 2.5: Input-admittance matrix of the grid-connected converter system as seen from the PCC for CVC; analytical model (solid-blue curves), simulation model (dotted-red curves)

.

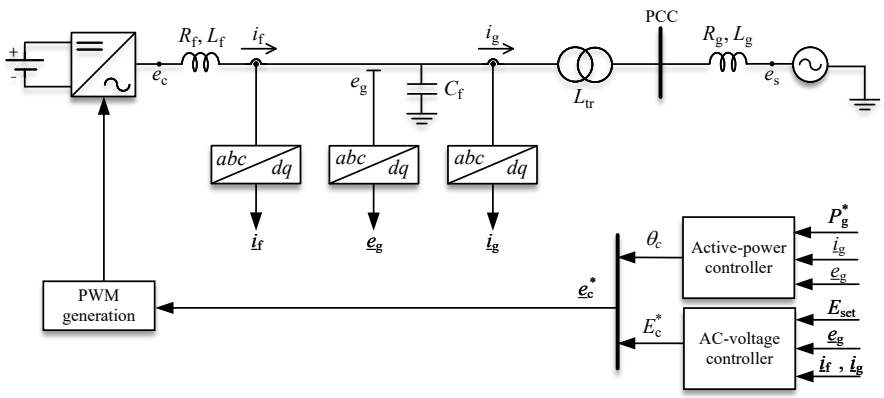

Figure 2.6: Single-line diagram of a grid-connected VSC and block scheme of DCCV.

in this case. To allow fault-ride-through operation of the converter system, an embedded current controller is used with this type of control strategy. As it is transparent during normal operation but only acts during over-current limitation [30], [33], it is not included in the system model.

AC-voltage controller

The ac-voltage controller implemented here comprises of an integrator with a reactive-power droop. To have an analogy with the CVC, the magnitude of the voltage at the low-voltage side of the transformer (voltage across the filter capacitor) is regulated using the ac-voltage controller. Accordingly, the converter voltage reference, $\underline{e}_{\mathrm{c}}^{\star}$, is calculated as

$$\underline{e}_{\mathrm{c}}^{\star} = V_{\mathrm{base}} + \overbrace{\frac{K_{\mathrm{i,vc}}}{s}}^{G'_{\mathrm{vc}}}(E_{\mathrm{set}} - \frac{K_{\mathrm{d,vc}}}{I_{\mathrm{base}}}Q_{\mathrm{g}} - \overbrace{\frac{\alpha_{\mathrm{fmv}}}{s+\alpha_{\mathrm{fmv}}}}^{H_{\mathrm{fmv}}}E_{\mathrm{g}}) - \overbrace{\frac{s}{s+\alpha_{\mathrm{hpf}}}}^{G_{\mathrm{hpf}}}R'_{\mathrm{a}}\underline{i}_{\mathrm{f}}, \quad (2.27)$$

with $E_{\mathrm{g}} = \sqrt{(e_{\mathrm{g}}^{d})^2 + (e_{\mathrm{g}}^{q})^2}$. The term α_{fmv} denotes the cut-off frequency of the low-pass filter for the capacitor voltage measurement. As suggested in [30], a transient damping term comprising of high-pass filtered converter current is added at the output of the ac-voltage controller to prevent a poorly damped closed-loop system. R'_{a} denotes the active resistance and α_{hpf} the cut-off frequency of the high-pass filter, whose values are selected as suggested in [30]. The integral gain of the controller, $K_{\mathrm{i,vc}}$, can be calculated using the loop-shaping approach described in [76], as

$$K_{\mathrm{i,vc}} = \frac{\alpha_{\mathrm{vc}}(X_{\mathrm{f}} + X_{\mathrm{tr}} + X_{\mathrm{g}})}{(X_{\mathrm{tr}} + X_{\mathrm{g}})}, \quad (2.28)$$

where α_{vc} denotes the desired closed-loop bandwidth.

Active-power controller

The structure of the active-power controller implemented here is similar to the one described in (2.16). The only difference is that, in this case, the active-power controller calculates the reference value of the converter-voltage angle,

and the synchronizing power coefficient is given by

$$K_{\mathrm{s}} = \frac{E_{\mathrm{c}} E_{\mathrm{s}}}{(X_{\mathrm{f}} + X_{\mathrm{tr}} + X_{\mathrm{g}})}. \tag{2.29}$$

Input-admittance derivation

Using (2.20) and (2.27), the small-signal model of the converter-voltage reference in the *source dq-frame* can be expressed as

$$\begin{aligned}
\begin{bmatrix} \Delta e_{\mathrm{c}}^{d\star} \\ \Delta e_{\mathrm{c}}^{q\star} \end{bmatrix} = & \overbrace{\begin{bmatrix} -(e_{\mathrm{c0}}^{q\star} + G_{\mathrm{hpf}} R'_{\mathrm{a}} i_{\mathrm{f0}}^{q}) & G'_{\mathrm{vc}} \cos\theta_{\mathrm{L0}} \\ (e_{\mathrm{c0}}^{d\star} + G_{\mathrm{hpf}} R'_{\mathrm{a}} i_{\mathrm{f0}}^{d}) & G'_{\mathrm{vc}} \sin\theta_{\mathrm{L0}} \end{bmatrix}}^{\mathbf{G}'_{\mathrm{T}}} \begin{bmatrix} \Delta\theta_{\mathrm{L}} \\ \Delta E_{\mathrm{set}} \end{bmatrix} + G'_{\mathrm{vc}} G_{\mathrm{PVc1}} \begin{bmatrix} \Delta i_{\mathrm{g}}^{d} \\ \Delta i_{\mathrm{g}}^{q} \end{bmatrix} \\
& + G'_{\mathrm{vc}} \left(G_{\mathrm{PVv1}} - \overbrace{\begin{bmatrix} \frac{H_{\mathrm{fmv}} \cos\theta_{\mathrm{L0}} e_{\mathrm{g0}}^{d}}{E_{\mathrm{g0}}} & \frac{H_{\mathrm{fmv}} \cos\theta_{\mathrm{L0}} e_{\mathrm{g0}}^{q}}{E_{\mathrm{g0}}} \\ \frac{H_{\mathrm{fmv}} \sin\theta_{\mathrm{L0}} e_{\mathrm{g0}}^{d}}{E_{\mathrm{g0}}} & \frac{H_{\mathrm{fmv}} \sin\theta_{\mathrm{L0}} e_{\mathrm{g0}}^{q}}{E_{\mathrm{g0}}} \end{bmatrix}}^{\mathbf{G}'_{\mathrm{PVv1}}} \right) \begin{bmatrix} \Delta e_{\mathrm{g}}^{d} \\ \Delta e_{\mathrm{g}}^{q} \end{bmatrix} \\
& + \overbrace{\begin{bmatrix} -G_{\mathrm{hpf}} R'_{\mathrm{a}} & 0 \\ 0 & -G_{\mathrm{hpf}} R'_{\mathrm{a}} \end{bmatrix}}^{\mathbf{G}_{\mathrm{DH}}} \begin{bmatrix} \Delta i_{\mathrm{f}}^{d} \\ \Delta i_{\mathrm{f}}^{q} \end{bmatrix},
\end{aligned} \tag{2.30}$$

Now, using the small-signal models for (2.13), (2.23) and (2.24), and using (2.22) and (2.30), the input admittance of the converter is derived as

$$\begin{aligned}
\mathbf{Y}_{\mathrm{conv}} = & [\mathbf{G}'_{\mathrm{T}} \mathbf{G}_{\mathrm{PVc2}} + G'_{\mathrm{vc}} G_{\mathrm{PVc1}} + \mathbf{G}_{\mathrm{DH}} - \mathbf{Z}_{\mathrm{f}}]^{-1} \\
& [\mathbf{G}'_{\mathrm{T}} \mathbf{G}_{\mathrm{PVv2}} + G'_{\mathrm{vc}} (G_{\mathrm{PVv1}} - \mathbf{G}'_{\mathrm{PVv1}}) + \mathbf{G}_{\mathrm{DH}} \mathbf{G}_{\mathrm{cap}} - \mathbf{Z}_{\mathrm{f}} \mathbf{G}_{\mathrm{cap}} - I],
\end{aligned} \tag{2.31}$$

$$\text{with} \quad \mathbf{Z}_{\mathrm{f}} = \begin{bmatrix} R_{\mathrm{f}} + sL_{\mathrm{f}} & -\omega_{\mathrm{N}} L_{\mathrm{f}} \\ \omega_{\mathrm{N}} L_{\mathrm{f}} & R_{\mathrm{f}} + sL_{\mathrm{f}} \end{bmatrix}.$$

Input admittance verification

The system and control parameters used for the simulation tests are given in Table 2.2. The same set points as the previous case are selected for the con-

Table 2.2: System and control parameters for DCCV

System parameters		Control parameters	
S_{N}	100 MVA (1.0 pu)	α_{vc}	$2\pi 3$ rad/s
E_{N}	20 kV (1.0 pu)	$K_{\mathrm{d,vc}}$	0.05 pu
ω_{N}	314.16 rad/s	R'_{a}	0.1 pu
R_{f}	0.015 pu	α_{hpf}	$2\pi 5$ rad/s
L_{f}	0.15 pu	α_{pc}	$2\pi 5$ rad/s
C_{f}	0.066 pu		
L_{tr}	0.15 pu		

verter. Figure 2.7 shows the frequency response of the magnitude and phase of the four elements of $\mathbf{Y}_{\mathrm{PCC}}$ for this case that are obtained analytically (solid-blue curves) and from the detailed simulation model (dotted-red curves). The results show a very good match verifying the validity of the analytical model.

2.4.3 Virtual-admittance based control (VABC)

Figure 2.8 shows the single-line diagram of a grid-connected VSC with VABC, whose structure is similar to the one proposed in [36]. Similar to the previous case, the filter capacitor is considered here for a fair comparison with CVC. As shown in Fig. 2.9, with this type of control strategy the VSC appears like a virtual machine connected to the grid, when seen from the connection point of the filter capacitor; with e_{EMF} representing the virtual back-electromotive force (EMF) and Z_{v} being the virtual impedance. The virtual impedance (R_{v}, L_{v}) includes the physical converter filter impedance (R_{f}, L_{f}) and a tunable virtual part (R'_{v}, L'_{v}). The virtual reactance, $X_{\mathrm{v}} = \omega_{\mathrm{N}} L_{\mathrm{v}}$, is selected in the range of a typical synchronous machine's transient reactance [36]. Due to a relatively large virtual reactance, changes in the virtual back-EMF result in a dc-current component. Hence, the virtual resistance, R_{v}, is chosen to provide a small time constant for the decay of this dc-current offset.

In this type of control strategy, the ac-voltage controller typically regulates the magnitude of the voltage at the PCC, and calculates the reference value of the virtual back-EMF magnitude; whereas, the active-power controller calculates the reference value of the virtual back-EMF angle, θ_{EMF}. As the outer loops in this case directly calculate the reference value of the virtual back-EMF vector, the grid-forming property is offered at the terminals of the

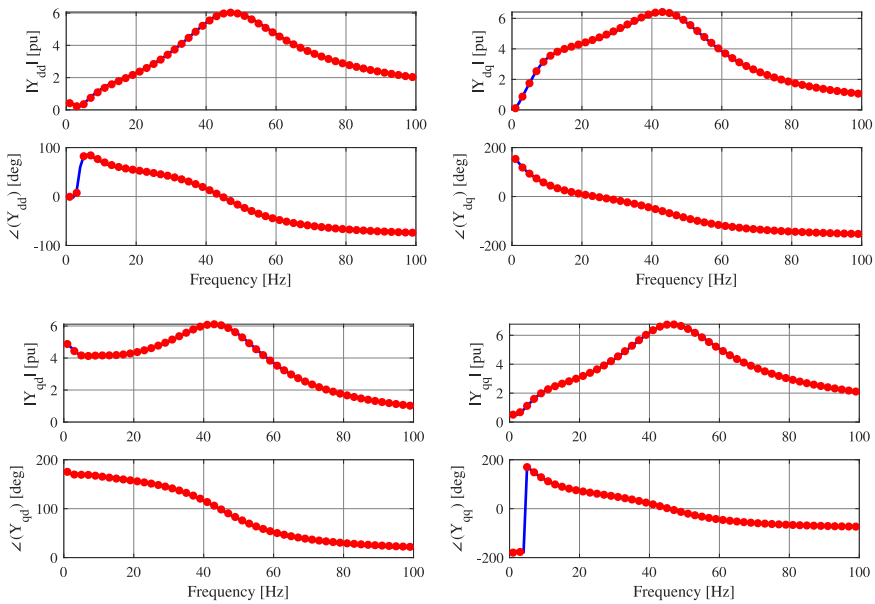

Figure 2.7: Input-admittance matrix of the grid-connected converter system as seen from the PCC for DCCV; analytical model (solid-blue curves), simulation model (dotted-red curves)

.

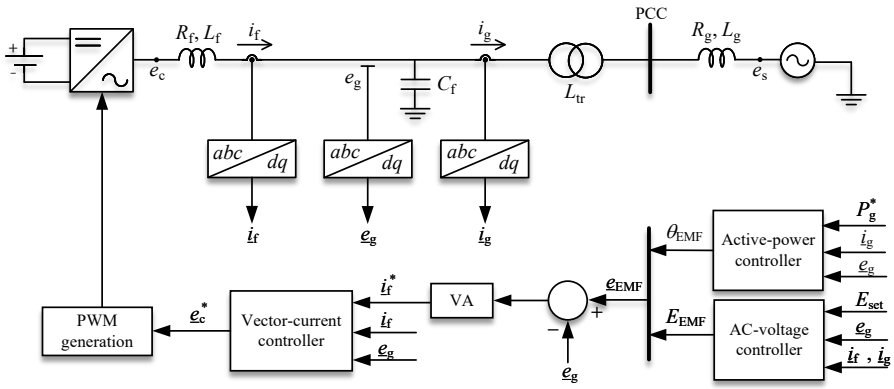

Figure 2.8: Single-line diagram of a grid-connected VSC and block scheme of VABC.

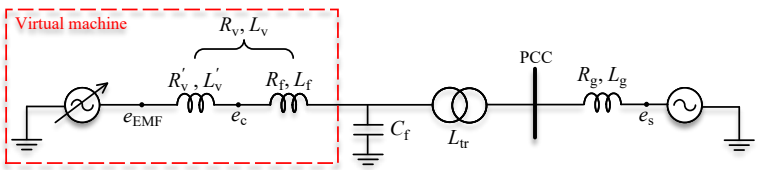

Figure 2.9: Equivalent circuit representation of a grid-connected VSC with VABC.

virtual machine. An inner-current controller as the one described in (2.12) is used to regulate the converter current and calculate the reference voltage for the modulation stage of the converter. The gains of the PI regulator in this case are calculated using the classical loop-shaping approach as $K_{\mathrm{p,cc}} = \alpha_{\mathrm{cc}} L_{\mathrm{f}}$ and $K_{\mathrm{i,cc}} = \alpha_{\mathrm{cc}} R_{\mathrm{f}}$, where α_{cc} denotes the loop bandwidth of the current controller [78]. The reference value for the current controller is calculated using the virtual admittance[7] (VA), as

$$\underline{i}_{\mathrm{f}}^{\star} = \frac{\underline{e}_{\mathrm{EMF}} - \underline{e}_{\mathrm{g}}}{R_{\mathrm{v}} + sL_{\mathrm{v}} + jX_{\mathrm{v}}}. \tag{2.32}$$

AC-voltage controller

The ac-voltage controller has a similar structure as the one described in (2.27). However, in this case, it calculates the virtual back-EMF voltage as

$$\underline{e}_{\mathrm{EMF}} = V_{\mathrm{base}} + \overbrace{\frac{K_{\mathrm{i,vc}}}{s}}^{G'_{\mathrm{vc}}} \left(E_{\mathrm{set}} - \frac{K_{\mathrm{d,vc}}}{I_{\mathrm{base}}} Q_{\mathrm{g}} - \overbrace{\frac{\alpha_{\mathrm{fmv}}}{s + \alpha_{\mathrm{fmv}}}}^{H_{\mathrm{fmv}}} E_{\mathrm{g}}\right) - \overbrace{\frac{s}{s + \alpha_{\mathrm{hpf}}}}^{G_{\mathrm{hpf}}} R'_{\mathrm{a}} \underline{i}_{\mathrm{f}}. \tag{2.33}$$

The integral gain for this case is selected as

$$K_{\mathrm{i,vc}} = \frac{\alpha_{\mathrm{vc}}(X_{\mathrm{v}} + X_{\mathrm{tr}} + X_{\mathrm{g}})}{(X_{\mathrm{tr}} + X_{\mathrm{g}})}. \tag{2.34}$$

Active-power controller

The structure of the active-power controller is similar to the one described in (2.16). In this case, the controller calculates the virtual back-EMF angle, and the synchronizing power coefficient is given by

$$K_{\mathrm{s}} = \frac{E_{\mathrm{EMF}} E_{\mathrm{s}}}{(X_{\mathrm{v}} + X_{\mathrm{tr}} + X_{\mathrm{g}})}. \tag{2.35}$$

Input-admittance derivation

Similar to the previous case, the first step here is to calculate the small-signal model of (2.33) in the *source dq-frame* by using (2.20). Next, by using the

[7] The VA corresponds to the inverse of the virtual impedance shown in Fig. 2.9

Table 2.3: System and control parameters for VABC

System parameters		Control parameters	
S_{N}	100 MVA (1.0 pu)	α_{ff}	$2\pi500$ rad/s
E_{N}	20 kV (1.0 pu)	α_{cc}	$2\pi500$ rad/s
ω_{N}	314.16 rad/s	$R_{\mathrm{v}} = 0.25$ pu	$L_{\mathrm{v}} = 0.5$ pu
R_{f}	0.015 pu	α_{vc}	$2\pi3$ rad/s
L_{f}	0.15 pu	$K_{\mathrm{d,vc}}$	0.05 pu
C_{f}	0.066 pu	$R'_{\mathrm{a}} = 0.1$ pu	$\alpha_{\mathrm{hpf}} = 2\pi5$ rad/s
L_{tr}	0.15 pu	α_{pc}	$2\pi5$ rad/s

small-signal models of (2.12), (2.13), (2.23), (2.24) and (2.32), and (2.20), (2.22) and (2.30), the input admittance of the converter, $\mathbf{Y}_{\mathrm{conv}}$ is derived as

$$\mathbf{Y}_{\mathrm{conv}} = [I - \mathbf{G}_{\mathrm{c,mat}}\mathbf{G}_{\mathrm{v}}(\mathbf{G}'_{\mathrm{T}}\mathbf{G}_{\mathrm{PVc2}} + G'_{\mathrm{vc}}G_{\mathrm{PVc1}} + \mathbf{G}_{\mathrm{DH}})]^{-1}$$
$$[\mathbf{G}_{\mathrm{cap}} + \mathbf{Y}_{\mathrm{i,mat}} - \mathbf{G}_{\mathrm{c,mat}}\mathbf{G}_{\mathrm{v}}(\mathbf{G}'_{\mathrm{T}}\mathbf{G}_{\mathrm{PVv2}} + G'_{\mathrm{vc}}(G_{\mathrm{PVv1}} - \mathbf{G}'_{\mathrm{PVv1}}) + \mathbf{G}_{\mathrm{DH}}\mathbf{G}_{\mathrm{cap}} - I)], \tag{2.36}$$

$$\text{with} \quad \mathbf{G}_{\mathrm{v}} = \frac{1}{(R_{\mathrm{v}} + sL_{\mathrm{v}})^2 + (\omega_{\mathrm{N}}L_{\mathrm{v}})^2} \begin{bmatrix} R_{\mathrm{v}} + sL_{\mathrm{v}} & X_{\mathrm{v}} \\ -X_{\mathrm{v}} & R_{\mathrm{v}} + sL_{\mathrm{v}} \end{bmatrix}.$$

Input admittance verification

The system and control parameters used for the simulation tests are given in Table 2.3. The same set points as the previous case are selected for the converter. Figure 2.10 shows the frequency response of the magnitude and phase of the four elements of $\mathbf{Y}_{\mathrm{PCC}}$ for this case that are obtained analytically (solid-blue curves) and from the detailed simulation model (dotted-red curves). Again, results show a very good match verifying the validity of the analytical model.

2.5 Comparison of grid-forming control strategies

By using the concept of passivity, the ability of the converter system to prevent adverse control interactions is assessed and compared for the three GFM control strategies. For this, the analytically derived input admittance matri-

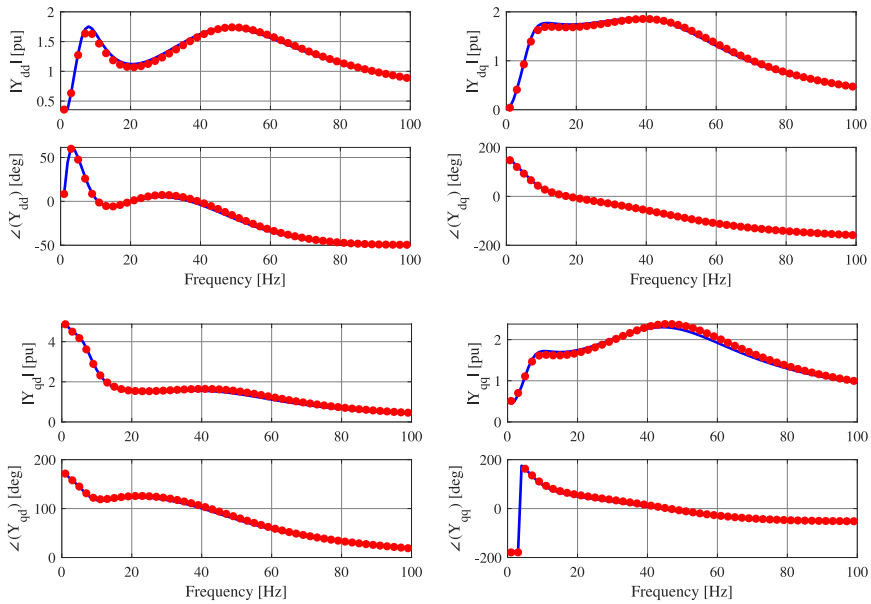

Figure 2.10: Input-admittance matrix of the grid-connected converter system as seen from the PCC for VABC; analytical model (solid-blue curves), simulation model (dotted-red curves)

.

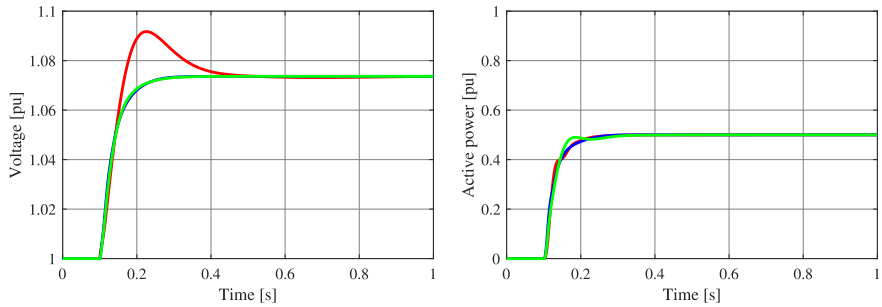

(a) (b)

Figure 2.11: Step-response of the a) ac-voltage controller b) active-power controller with CVC (red), DCCV (blue), and VABC (green).

ces are used to asses the power-dissipative behaviour of the converter system in the sub-synchronous frequency region. The same control parameters as listed in Tables 2.1, 2.2 and 2.3 are used for the GFM control strategies. As shown in Fig. 2.11, the parameter choice has been made in such a way that for all the three GFM control strategies, a similar rise-time for a step in the active-power reference and capacitor voltage set-point is obtained in a strong grid case (SCR $= \frac{1}{X_g(\text{in pu})} = 10.0$). Furthermore, the influence of the considered GFM control strategies on the performance of the converter system during large variations in the grid strength is also investigated.

2.5.1 Ability to prevent adverse control interactions

In order to reduce the risk of control interactions, the converter system should impose a passive behaviour over a large frequency range [79], [81]. Passivity is related to the resistive behaviour of a device, which is a very desirable property for the grid-connected converter systems, as it prevents the converter system from contributing negatively towards the stability of the network. Passivity of a Multiple-Input/Multiple-Output (MIMO) system can be understood from its power-dissipative property as described here. Once again considering the generic electrical system shown in Fig. 2.4, the relation between the voltage

and current phasors v and i can be expressed in steady-state as

$$i(j\omega) = \mathbf{Y}(j\omega)e(j\omega). \tag{2.37}$$

In a rotating dq frame and by using power-invariant Clark transformation and (2.37), the active input power, P, for the current direction shown in Fig. 2.4 is given by [79]

$$P = \frac{1}{2}(e^H i + i^H e) = \frac{1}{2}e^H[\mathbf{Y}(j\omega) + \mathbf{Y}^H(j\omega)]e = \frac{1}{2}e^H\mathbf{Y}_\mathrm{P}e, \tag{2.38}$$

where the superscript H denotes the Hermitian conjugate, i.e., the transpose and complex conjugate of a matrix.

When $\mathbf{Y}_\mathrm{P} > 0$ (positive-definite matrix), (2.38) is positive, meaning that the active power is dissipated at the frequency ω. This holds if and only if the eigenvalues, $\lambda_{1,2}$, of $\mathbf{Y}_\mathrm{P}$ are positive [79]. Therefore, the power-dissipative property (thus, passivity) of the converter system can be understood by analysing the frequency characteristic of the two eigenvalues, $\lambda_{1,2}$, of the matrix $[\mathbf{Y}_\mathrm{PCC} + \mathbf{Y}^H_\mathrm{PCC}]$. For those frequency intervals where the eigenvalues are positive (meaning that the converter system is power dissipative), there is no risk of negative contribution from the converter system towards stability of the network. On the other hand, the existence of frequency intervals where one of the eigenvalues is negative (meaning that the converter system is non-dissipative) indicates a risk of causing instability. For all the case studies presented in this section, one of the two eigenvalues is always positive; hence, only the minimum of the two eigenvalues, λ_min, which is termed as the passivity index, is considered for the analysis here. For the generic admittance matrix given in (2.18), λ_min is given by [82]

$$\lambda_\mathrm{min} = 0.5([a+b] - \sqrt{[a-b]^2 + [c_1+c_2]^2 + [d_2-d_1]^2}), \tag{2.39}$$

where the variables are defined as

$$\begin{aligned} a = \mathrm{Re}[Y_\mathrm{dd}(jw)], \quad b = \mathrm{Re}[Y_\mathrm{qq}(jw)] \\ c_1 = \mathrm{Re}[Y_\mathrm{dq}(jw)], \quad d_1 = \mathrm{Im}[Y_\mathrm{dq}(jw)] \\ c_2 = \mathrm{Re}[Y_\mathrm{qd}(jw)], \quad d_2 = \mathrm{Im}[Y_\mathrm{qd}(jw)]. \end{aligned}$$

Figure 2.12 shows the frequency response of the passivity index for the

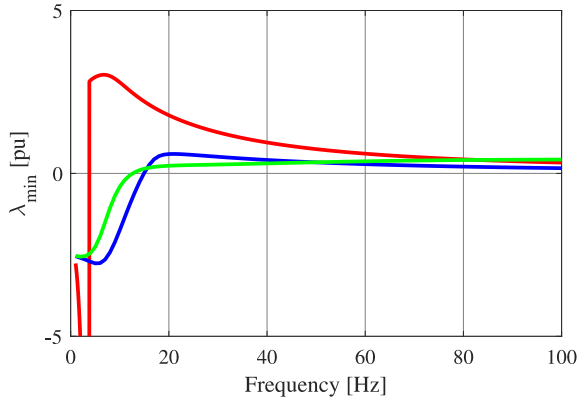

Figure 2.12: Frequency response of the passivity index with: CVC (red), DCCV (blue), and VABC (green).

considered GFM control strategies. It can be seen from the figure that the converter system presents a non-passive behaviour at low frequencies for all the three GFM control strategies. The frequency region in which the converter system exhibits a non-passive behavior is relatively small with CVC as compared to the other two control strategies. However, at very low frequencies (between 0-4.0 Hz in this case), there is a higher risk of control interactions with CVC. This is evident from the more negative values of the passivity index with CVC as compared to DCCV or VABC at those frequencies. It can also be observed from the figure that the passivity of the converter system with VABC is slightly better as compared to DCCV.

It is found that the speed of response of both ac-voltage and active-power controllers affect the passivity of the converter system in the low-frequency region. It can be observed from Fig. 2.13 that for all the three GFM control strategies, reducing the speed of response of both ac-voltage and active-power controllers improves the passivity of the converter system at low frequencies. Hence, it is advantageous to keep the loop bandwidth of ac-voltage and active-power controllers as low as possible from the passivity point-of-view. This behaviour agrees well with the requirements from the National Grid ESO, which specifies a 5 Hz limit for the loop bandwidths of both active-power and voltage controllers for the GFM converters to avoid control interactions [17]. However, the energy storage capacity of the converter system imposes

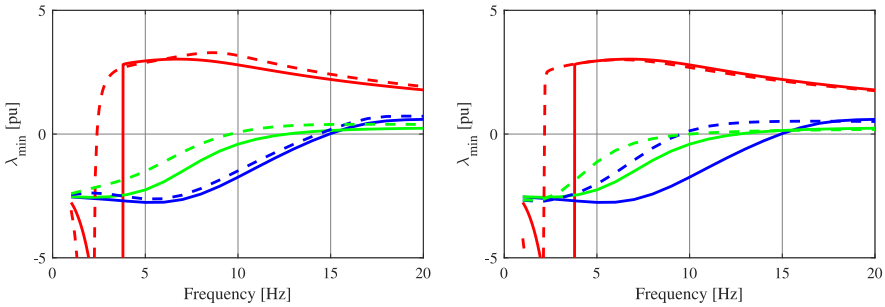

Figure 2.13: Frequency response of the passivity index with speed of response of a) ac-voltage and b) active-power controllers reduced to half (dashed curves) of its original value (solid curves) for: CVC (red), DCCV (blue) and VABC (green).

restrictions on the lower limit of the active-power controller's loop bandwidth.

2.5.2 Impact of grid strength on control performance

The impact of grid strength on the performance of the converter system during an active-power step is investigated here. For this, the closed-loop transfer function of the active-power controller, $F_{\mathrm{pc}}(s)$, in (2.8) is recalled.

$$F_{\mathrm{pc}}(s) = \frac{\Delta P_{\mathrm{g}}}{\Delta P_{\mathrm{g}}^{\star}} = \frac{K_{\mathrm{p,pc}} s + K_{\mathrm{i,pc}}}{\frac{s^2}{K_{\mathrm{s}}} + (K_{\mathrm{p,pc}} + R_{\mathrm{a}}) s + K_{\mathrm{i,pc}}}, \tag{2.40}$$

where K_{s} is given in accordance with (2.17), (2.29) and (2.35) for CVC, DCCV and VABC, respectively. It can be seen from (2.17) and (2.29) that in case of both CVC and DCCV, a small value of $X_{\mathrm{tr}} = 0.15$ pu and $X_{\mathrm{f}} = 0.15$ pu, makes K_{s} in these two cases highly dependent on the grid reactance. This makes the tuning of their active-power controllers more sensitive to any variations in the SCR of the grid. On the contrary, due to a relatively large value of virtual reactance, $X_{\mathrm{v}} = 0.5$ pu, in case of VABC, the impact of the grid strength on K_{s} is lower. Hence, the tuning of active-power controller is more robust in case of VABC as compared to the other two. This can be visualized from the pole-zero map of $F_{\mathrm{pc}}(s)$ for the three GFM control strategies shown in

Fig.2.14.

It can be observed from Fig. 2.14(a) and 2.14(b) that as the grid strength decreases, the poles of $F_{\mathrm{pc}}(s)$ move closer towards the origin for both CVC and DCCV. On the other hand, in case of VABC, there is a relatively less movement in the poles when decreasing grid strength as seen from Fig. 2.14(c). This explains for a slower and less damped response of the active-power controller with decreasing grid strength for both CVC and DCCV, whereas in case of VABC, the change is smaller as can be visualized in Fig. 2.15.

2.6 Summary

A new structure for the active-power controller of GFM converters has been proposed in this chapter, which allows selection of a higher damping factor without affecting the steady state frequency-droop characteristics of the converter system. Additionally, three GFM control strategies have been investigated and compared, based on their influence on the frequency characteristics of the converter system and ability to provide a robust converter operation in varying grid strength. The case studies presented here reveal that a high loop bandwidth of the ac-voltage and active-power controllers negatively impact the passivity of the converter system in the sub-synchronous frequency region for the considered GFM control strategies. Hence, it is advantageous to keep the loop bandwidth of ac-voltage and active-power controllers as low as possible from the passivity point-of-view. However, the energy storage capacity of the converter system imposes a restriction on the lower limit of the active-power controller's speed of response. Due to a relatively better performance of the converter system from the passivity point-of-view at low frequencies and under varying grid strength, VABC is the preferred choice in this thesis among the investigated variants of the GFM control strategies. Furthermore, the resistive-inductive nature of the VA used in this type of control, facilitates provision of additional reference-current filtering (through virtual reactance) and damping (through virtual resistance) from the converter without a need of larger physical components.

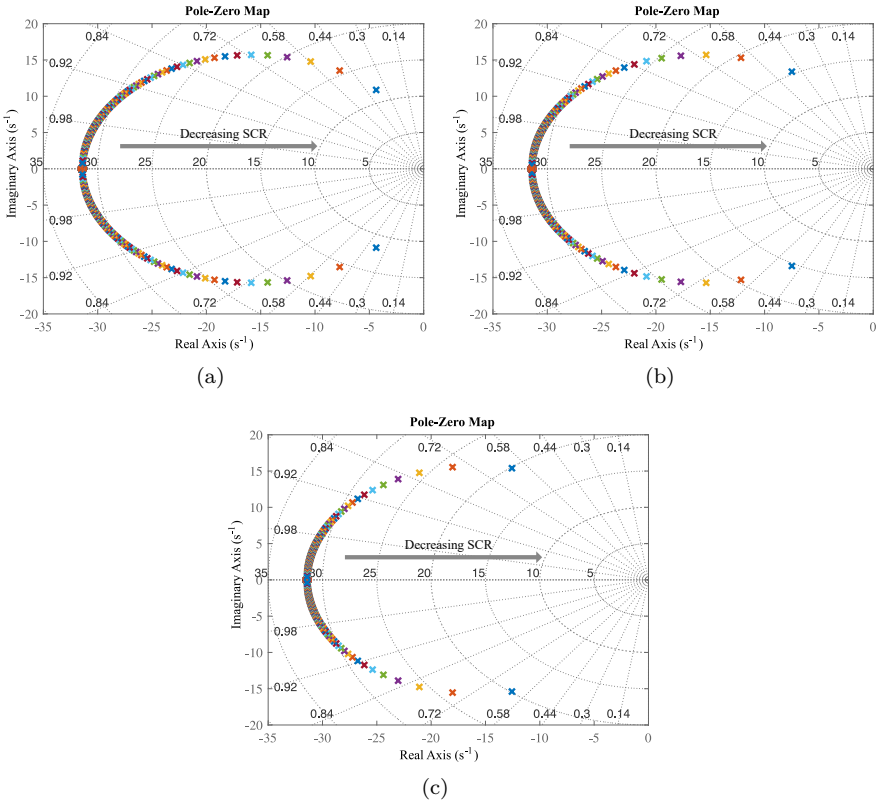

Figure 2.14: Pole-zero map of $F_{\mathrm{pc}}(s)$ with variation in the grid-strength for (a) CVC (b) DCCV and (c) VABC.

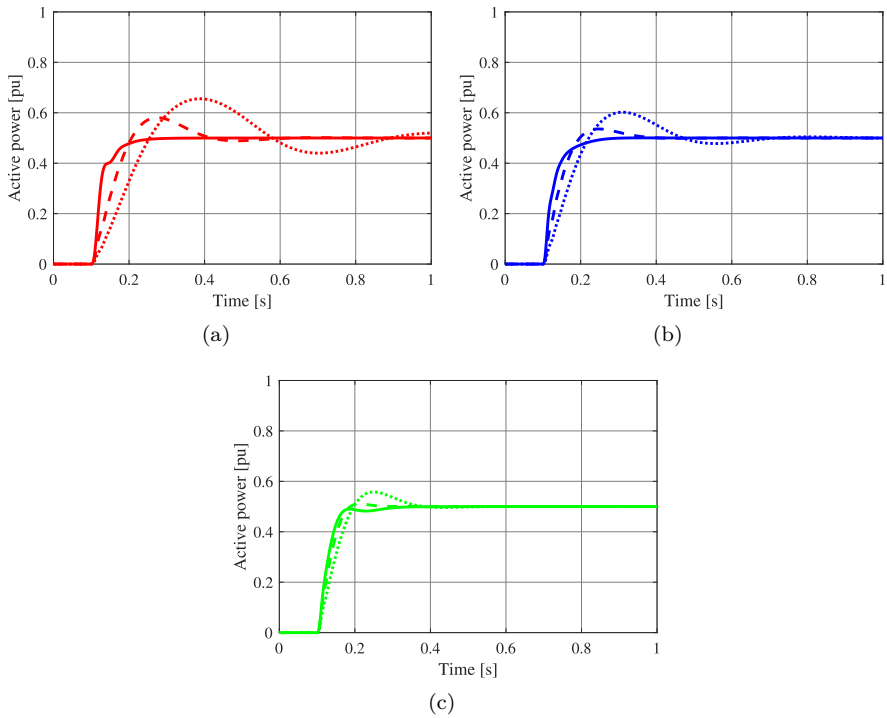

Figure 2.15: Impact of grid strength on the performance of (a) CVC (b) DCCV (c) VABC. SCR = 10.0 (solid), SCR = 3.0 (dashed), SCR = 1.0 (dotted).

CHAPTER 3

Operation of grid-forming converters during current limitation

3.1 Introduction

Unlike the conventional SGs that can withstand a fault current of up to several times their rated value, power-electronic converters have a very limited over-current capability. Hence, it is necessary to be able to limit the converter current not only during normal operation, but even during grid disturbances irrespective of the control strategy implemented for the converter. As described in the previous chapter, in contrast to the more conventional GFL control, GFM control strategies model the converter system as a controllable voltage source behind an impedance. Consequently, there is no direct control over the current exchanged between the converter and the grid, thereby making its limitation challenging [44], [45]. Typically in grid-connected converter systems, current limitation is reached during large grid disturbances such as faults or large frequency excursions. It is during such conditions when the grid is most vulnerable and in need of support. For this reason, it is desirable that the converter systems retain as much of their GFM behaviour as possible even

during current limitation. This implies that, if at all necessary, the converter dynamic properties should be changed for the shortest time possible, typically up to a few cycles at fundamental frequency; then the converter system should return into linear control mode [41], [42].

This chapter first theoretically describes the transient stability problem of GFM converters during current limitation. Thereafter, a novel current-limitation strategy based on the limitation of the reference active power and the magnitude of the virtual back-EMF is presented. Finally, the effectiveness of the proposed limitation strategy in case of various grid disturbances is validated using an experimental setup.

3.2 Angle stability problem of grid-forming converters

The GFM converter's angle stability problem is analyzed here by using the equivalent circuit representation of a grid-connected converter system with the VABC shown in Fig. 3.1(a). The block-scheme of the VABC is recalled and shown in Fig. 3.1(b). Neglecting the system losses, the steady state converter current (in pu) in the synchronous-reference frame aligned with the converter's virtual back-EMF voltage is given by

$$\underline{I}_{\mathrm{f}} = \frac{\underline{E}_{\mathrm{EMF}} - \underline{E}_{\mathrm{s}}}{jX} = \frac{E_{\mathrm{s}} \sin\delta + j(E_{\mathrm{s}} \cos\delta - E_{\mathrm{EMF}})}{X}, \tag{3.1}$$

where δ denotes the phase-angle difference between the virtual back-EMF and the ideal-voltage source, and $X = X_{\mathrm{v}} + X_{\mathrm{g}}$ is the total reactance between them. The active power transferred from the converter to the grid is defined as

$$P_{\mathrm{g}} = \mathrm{Re}\{\underline{E}_{\mathrm{EMF}}\ \mathrm{conj}\{\underline{I}_{\mathrm{f}}\}\} = \frac{E_{\mathrm{EMF}} E_{\mathrm{s}}}{X} \sin\delta. \tag{3.2}$$

To investigate the impact of current limitation on the transient stability of the converter, a current-magnitude limiter (also addressed as circular-current limiter [48]) is introduced. Applying this to limit the unlimited converter-current reference, $\underline{I}_{\mathrm{f}}^{\star}$, results in a limited converter-current reference, $\underline{I}_{\mathrm{f,lim}}^{\star}$

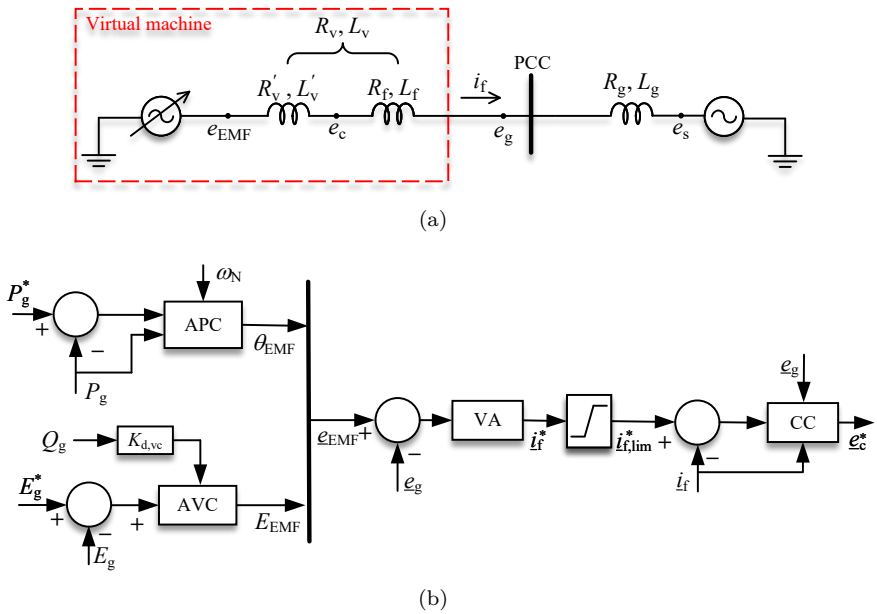

Figure 3.1: (a) Equivalent circuit representation of a GFM converter with VABC (b) Block scheme of the VABC.

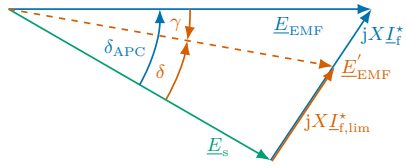

Figure 3.2: Phasor diagram illustrating the effect of current limitation on the virtual back-EMF. Unlimited in blue, limited in red [83].

as

$$\underline{I}_{\mathrm{f,lim}}^{\star} = \underline{I}_{\mathrm{f}}^{\star} \frac{I_{\max}}{I_{\mathrm{f}}^{\star}} \qquad \forall\ I_{\mathrm{f}}^{\star} > I_{\max}, \tag{3.3}$$

where $I_{\max}$ denotes the maximum allowed converter current. This current limitation is equivalent to a variation of the virtual back-EMF phasor from $\underline{E}_{\mathrm{EMF}}$ to $\underline{E}'_{\mathrm{EMF}}$ as shown in Fig. 3.2. The figure shows that the current limitation results in a reduced load angle, δ, as compared to the unlimited angle demanded by the active-power controller (APC), δ_{APC}[1]. Even though the load angle is manipulated by the current limitation, δ_{APC} still has an impact on the exchanged active power as it determines the angle of the current references $\underline{I}_{\mathrm{f}}^{\star}$ and consequently $\underline{I}_{\mathrm{f,lim}}^{\star}$. Using (3.1)-(3.3), the relation between the current-limited active power, P_{lim}, and δ_{APC} can be expressed as

$$\begin{aligned} P_{\mathrm{lim}} &= \mathrm{Re}\{\underline{E}_{\mathrm{s}}\ \mathrm{conj}\{\underline{I}_{\mathrm{f,lim}}^{\star}\}\} \\ &= \frac{E_{\mathrm{EMF}} E_{\mathrm{s}} I_{\max} \sin\delta_{\mathrm{APC}}}{\sqrt{E_{\mathrm{EMF}}^2 + E_{\mathrm{s}}^2 - 2E_{\mathrm{EMF}} E_{\mathrm{s}} \cos\delta_{\mathrm{APC}}}} \qquad \forall\ I_{\mathrm{f}}^{\star} > I_{\max}. \end{aligned} \tag{3.4}$$

Figure 3.3 illustrates the P-δ_{APC} relationship according with (3.2) in blue and (3.4) in red for an example system. It can be observed from the figure that in contrary to the unlimited case shown in blue, the power transfer decreases with an increasing δ_{APC} after the current reaches its limit at the operating point B.

Based on this analysis, the two main sources of GFM converter's angle stability problem can be identified: firstly, an active-power reference which is too large for the prevailing grid conditions (i.e., grid-voltage magnitude and grid strength) during a fault or in post-fault steady-state, and secondly the

[1]Note that without current limitation, $\delta = \delta_{\mathrm{APC}}$.

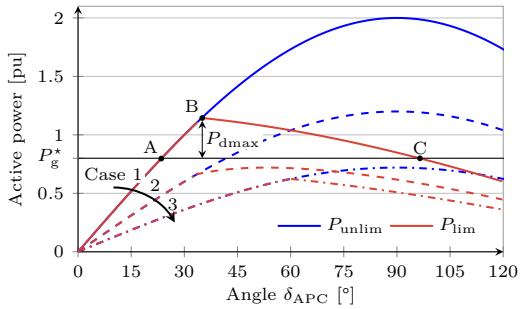

Figure 3.3: P-δ_{APC} curve illustrating the converter angle stability problem for a current limit of 1.2 pu. A: pre-disturbance operating point; B: current limit reached; C: transient stability limit; P_{dmax}: maximum decelerating power; all outlined for case 1: $E_{\mathrm{EMF}} = E_{\mathrm{s}} = 1.0$ pu. Case 2: $E_{\mathrm{EMF}} = 1.0$ pu & $E_{\mathrm{s}} = 0.6$pu; case 3: $E_{\mathrm{EMF}} = E_{\mathrm{s}} = 0.6$ pu.

inability of the active-power controller to follow the grid-voltage angle during a frequency disturbance or phase-angle jump. Both instability mechanisms are summarized in this section.

3.2.1 Voltage-dip induced converter angle instability

The first of the two angle instability mechanisms is caused by a voltage dip resulting from a fault, for instance. Equations (3.2) and (3.4) demonstrate that the active-power transfer between the converter and the grid is proportional to the product of E_{EMF} and E_{s}. Consequently, a voltage dip will result in a reduced active-power transfer capability, no matter how the magnitude of the virtual back-EMF is controlled in response to the voltage dip (compare cases 2 and 3 in Fig. 3.3). As described in [55], the instability under such conditions can occur due to violated equal-area criterion, which mainly affects the GFM converters providing synthetic inertia support, or due to a lack of a stable post-fault operating point. This type of instability has been studied widely in the literature and several solutions have been proposed [84]. The most popular solutions are scaling of the power references proportional to the voltage magnitude [48], control-mode switching (e.g. deactivation of inertia [85] or transition to a GFL control [30], [33]) and inclusion of additional control terms [86]. Of these approaches, voltage-proportional power reference scaling

has the advantage of retaining as much of the GFM capabilities as possible, while at the same time aiding in current-limitation. Moreover, in contrast to approaches modifying the control structure, it does not require any fault detection mechanism [84].

3.2.2 Frequency-disturbance induced converter angle instability

The second angle instability mechanism is caused by severe frequency disturbances or phase-angle jumps in the grid, resulting in the inability of the active-power controller to follow the grid-voltage angle and moving the operating point to the unstable part in Fig. 3.3. Since the active-power controller in a GFM converter does not only provide power reference tracking but also the synchronization, a power control error is required to follow a change in the grid frequency by letting the active-power controller adapt the converter's internal frequency, ω_c. For instance, a decline in the grid frequency causes δ_APC to increase until the additional decelerating power $P_\mathrm{d} = -2H\frac{\mathrm{d}\omega_\mathrm{c}}{\mathrm{d}t}$ is reached. However, during current limitation the decelerating power might not be large enough to keep the converter's internal frequency synchronized with the grid frequency, which would lead to a continuous increase of δ_APC. If the unstable equilibrium point C is crossed the synchronizm is lost, which is equivalent to a synchronous generator's first swing instability.

Limitation of the outer loop references as introduced in the previous instability mechanism cannot prevent loss of synchronizm in this case. This is because the requirement for the additional active power, which exceeds the current-limited maximum, P_dmax, is not caused by a change in the reference, but by the inability of the slow active-power controller to reject the grid disturbance. This slowness is desired to provide an inertial support to the grid, but causes instability when the converter current limits are reached. As the angle output of the active-power controller is manipulated to guarantee current limitation, the synchronization signal is lost. Not only the GFM converters adopting VABC structure, but all GFM converters with non-zero inertia time-constant that rely on the active-power controller for synchronization and provision of synthetic inertia are vulnerable to type of instability. The risk for this type of instability increases with a large virtual inertia constant of the converter, H, high RoCoF and operating points close to the maximum transferable active power, due to more decelerating power being needed or

less current reserve being available for it, respectively.

While these instability mechanisms are studied here for a GFM converter with circular-current limitation, the same principles apply for GFM converters relying on a virtual impedance for current limitation. This can be understood from (3.2), showing that an increase in the reactance between the virtual back-EMF and the grid voltage will reduce the active-power transfer for any given load angle, which results in similar dynamics for both instability types.

3.3 Proposed methodology to limit converter current

From the previous section, it is understood that limitation of the current reference for the current controller (henceforth referred to as hard-current limiter) might in GFM converters result in a loss of synchronization with the ac grid. Furthermore, the use of a hard-current limiter introduces non-linearities in the control system and modifies the dynamic properties of the converter (by hiding the impact of the voltage controller and the virtual admittance) while activated, which is not desirable as discussed earlier [41], [42]. This section presents a novel strategy that allows to keep the converter current within its permissible value without relying on the hard-current limiter and alteration of the GFM properties.

In a grid-following converter, the use of a hard-current limiter is effective because such converters are modeled as a current source. Following the same philosophy for GFM converters, which are modeled as a voltage source instead, current limitation can be achieved by dynamically limiting the generated virtual back-EMF, $\underline{e}_{\mathrm{EMF}}$, so that the resulting current reference is within the limits. This is realized through the GFM control structure depicted in Fig. 3.4. It is of importance to consider that, unlike the magnitude, limiting the phase of the voltage vector $\underline{e}_{\mathrm{EMF}}$ is challenging. This is because in the absence of a PLL in GFM converters, there is no direct information about the load angle; and hence, the active-power flow from the converter dictates the phase of the emulated voltage source. Therefore, one obvious solution is to include a PLL in the design of the APL to calculate the converter's load angle. However, this can have a negative impact on the stability of the converter in weak grids, and restrict the converter's GFM properties [87]. Another alternative to limit the resulting phase of the converter at all times without the aforementioned

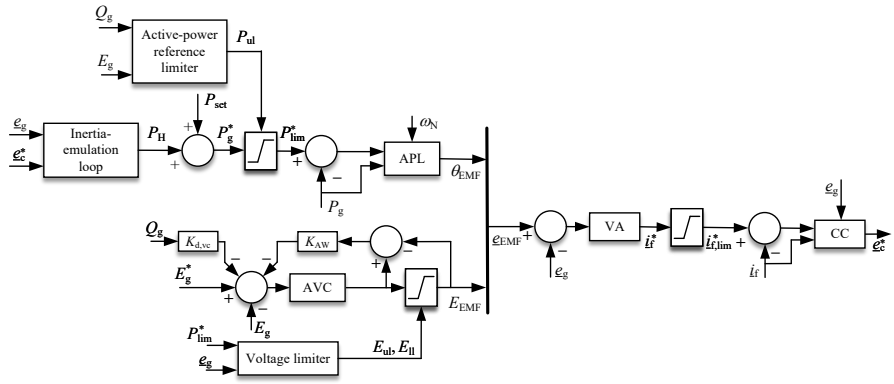

Figure 3.4: Block diagram of the proposed control structure for GFM converters.

restrictions is to limit the active-power reference. However, as discussed in the previous section, this solution is not effective in GFM converter systems emulating inertia, owing to their slow active-power controller. To overcome this issue, a cascaded active-power controller described in the following section is proposed. The calculation of the limits for the active power and voltage magnitude references is described in the subsequent sections.

3.3.1 Cascaded active-power controller

The cascaded active-power controller consists of an inertia-emulation loop (IEL) in cascade with a fast active-power loop (APL). The IEL is illustrated in Fig. 3.5 and is based on the structure of a PLL. It is used to calculate the inertial power, P_{H}, to be injected (or absorbed) by the converter in case of frequency disturbances. This is similar to the approach proposed in [88], where a PLL is used to provide an inertial response from a GFL converter. The advantage of this approach over other methods to provide RoCoF-proportional inertial response is that the frequency derivative is implicitly determined within the PLL. This replaces the noise-sensitive derivation step and means that the RoCoF estimate is immediately available, reducing delays in the converter's inertial response [88]. The inertial power P_{H} is then added onto the active power set-point of the converter, P_{set}, to form the reference power, $P_{\mathrm{g}}^{\star}$, for the APL, which can be effectively limited. The PI-based APL then tracks the

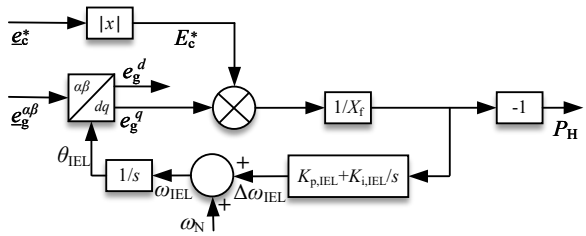

Figure 3.5: Structure of the inertia-emulation loop.

limited power reference, $P^{\star}_{\text{lim}}$, and synchronizes the converter with the grid.

Providing the inertia through the active-power reference allows a higher closed-loop bandwidth for the APL, thus making synchronization and reference tracking fast[2]. Decoupling the synchronization task of the APL from the inertia provision gives the flexibility to limit and achieve a fast control over the active-power injection from the converter, and ultimately the resulting phase of the virtual back-EMF. The magnitude of the virtual back-EMF, E_{EMF}, can then be limited based on the available PCC voltage and estimated power flow as described in Section 3.3.3. In this way it is possible to limit the generated current reference vector without triggering the hard-current limiter.

Tuning of the inertia-emulation loop

The IEL shown in Fig. 3.5 is designed in such a way that its output is a pure inertial power, P_{H}, which is equivalent to the inertial response of a lossless synchronous condenser (SC). The fundamental idea is that both SC and IEL track the phase angle of the grid voltage with a given speed, which corresponds to their inertia. To derive the parameters of the IEL, the swing equation of a SC is utilized, which is given as

$$\frac{2H}{\omega_{\text{N}}} s\omega_{\text{r}} = -P_{\text{g}} - \frac{K_{\text{D}}}{\omega_{\text{N}}}(\omega_{\text{r}} - \omega_{\text{g}}), \tag{3.5}$$

where ω_{r} and ω_{g} denote the angular frequency (in rad/s) of the rotor and at the the PCC, respectively, and P_{g} is the electrical power (in pu) injected to the grid. By neglecting the resistances and assuming a dq-reference frame that

[2]The upper limit for the closed-loop bandwidth of the APL is limited by the grid-code requirements (5.0 Hz, for instance, from the National Grid ESO [17])

is aligned with the machine's back EMF, P_g can be expressed in quasi-steady state as

$$P_\mathrm{g} = \frac{E_\mathrm{EMF} E_\mathrm{g}}{X} \sin(\theta_\mathrm{r} - \theta_\mathrm{g}) = -\frac{E_\mathrm{EMF}}{X} e_\mathrm{g}^q, \tag{3.6}$$

where e_g^q denotes the q-component of the PCC voltage, and X is the sum of the reactances between the back EMF and PCC. In case of a SC, the back EMF and PCC voltage are aligned to each other in steady state and e_g^q is zero. However, a change in the PCC-voltage angle will result in a misalignment of the two voltages and an active-power flow, $P_\mathrm{g} = P_\mathrm{H}$. For a small angle difference, (3.6) can be expressed as

$$P_\mathrm{g} = P_\mathrm{H} = \frac{E_\mathrm{EMF} E_\mathrm{g}}{X} (\theta_\mathrm{r} - \theta_\mathrm{g}) = \frac{E_\mathrm{EMF} E_\mathrm{g}}{X s} (\omega_\mathrm{r} - \omega_\mathrm{g}), \tag{3.7}$$

where the following relationships are utilized

$$s\theta_\mathrm{r} = \omega_\mathrm{r} \qquad \text{and} \qquad s\theta_\mathrm{g} = \omega_\mathrm{g}. \tag{3.8}$$

Using (3.7), (3.5) can be rearranged as

$$s\omega_\mathrm{r} = -(\frac{K_\mathrm{D}}{2H P_\mathrm{max,SC}} s + \frac{\omega_\mathrm{N}}{2H}) P_\mathrm{H}, \quad \text{with} \quad P_\mathrm{max,SC} = \frac{E_\mathrm{EMF} E_\mathrm{g}}{X}. \tag{3.9}$$

An equivalent expression can now be derived for the IEL. If the negation of the emulated inertial-power reference, i.e., -P_H is selected as the input to the IEL's PI-regulator (see Fig. 3.5), the derivative of the loop's estimated frequency is determined as

$$s\omega_\mathrm{IEL} = -(K_\mathrm{p,IEL} s + K_\mathrm{i,IEL}) P_\mathrm{H}, \tag{3.10}$$

where ω_IEL is the loop's frequency estimate, $K_\mathrm{p,IEL}$ and $K_\mathrm{i,IEL}$ are the proportional and integral gains, respectively. In this case, the inertial power, P_H, is defined as

$$P_\mathrm{H} = -\frac{E_\mathrm{c}^\star}{X_\mathrm{f}} e_\mathrm{g}^q, \tag{3.11}$$

with e_g^q denoting the q-component of the PCC voltage in the synchronous-rotating frame defined by the IEL's angle, θ_IEL, and aligned with the PCC

voltage; whereas, X_f represents the filter reactance and $E_\mathrm{c}^\star$ the magnitude of the reference voltage vector output from the current controller (CC). Basically, (3.11) is the two-port equation formulated using the terminal voltage of the converter and PCC voltage. Unlike (3.6), the terminal voltage of the converter is used here instead of the virtual back-EMF; this is to overcome the coupling between active and reactive power introduced by the large virtual resistance.

The tracking behaviour of the SC given by (3.9) and that of the IEL in (3.10) can be related to each other to establish an equivalent behaviour resulting in the following tuning criteria

$$K_\mathrm{i,IEL} = \frac{\omega_\mathrm{N}}{2H}, \quad K_\mathrm{p,IEL} = \frac{K_\mathrm{D}}{2HP_\mathrm{max}}, \quad \text{with} \quad P_\mathrm{max} = \frac{E_\mathrm{c}^\star E_\mathrm{g}}{X_\mathrm{f}}. \tag{3.12}$$

It can be observed from (3.12) that the integral gain of the IEL relates to the inertia constant to be emulated, while the proportional gain to the damping. To receive an accurate replication of the desired inertial response it is advisable to subtract the inertia constant remaining in the APL from the inertia constant used for the IEL so that the cumulative effect is as required. The inertia constant remaining in the APL depends upon its closed-loop bandwidth and can be calculated using (2.11).

Selection of the inertia-emulation loop's damping coefficient

In a SC, damping is linked to the physical properties such as friction and typically associated with losses. As a consequence, SCs are usually poorly damped. On the contrary, in the IEL, the damping does not imply any losses, which means it becomes an additional degree of freedom. However, an increased damping comes with a downside of slower response. Hence, the damping coefficient should be selected as a compromise between the speed and damping of the inertial response.

As described earlier, the inertial response relates to tracking changes in the grid-voltage angle with a certain speed. This tracking speed is determined by the closed-loop transfer function of the IEL, which is given by

$$G_\mathrm{IEL}(s) = \frac{\Delta\theta_\mathrm{IEL}}{\Delta\theta_\mathrm{g}} = \frac{P_\mathrm{max}(K_\mathrm{p,IEL}s + K_\mathrm{i,IEL})}{s^2 + P_\mathrm{max}K_\mathrm{p,IEL}s + P_\mathrm{max}K_\mathrm{i,IEL}}, \tag{3.13}$$

where the small-signal relationship $E_\mathrm{g}\Delta\theta_\mathrm{g} = \Delta E_\mathrm{g}^q$ is utilized. This can be

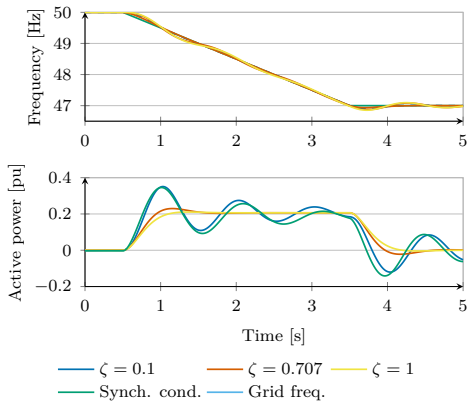

Figure 3.6: Comparison with synchronous condenser and impact of the damping ratio on rise time and overshoot.

related to a generalized second-order transfer function with the zero as

$$G_{\mathrm{IEL}}(s) = \frac{2\zeta\omega_{\mathrm{n}}s + \omega_{\mathrm{n}}^2}{s^2 + 2\zeta\omega_{\mathrm{n}}s + \omega_{\mathrm{n}}^2}, \tag{3.14}$$

which using (3.12) allows to determine the proportional gain based on the desired damping ratio, ζ, as

$$K_{\mathrm{p,IEL}} = \zeta\sqrt{\frac{2\omega_{\mathrm{N}}}{HP_{\mathrm{max}}}}. \tag{3.15}$$

The effect of different damping ratios is shown using time-domain simulations of the example grid-connected converter system shown in Fig. 3.1. For this case study, frequency of the ideal-voltage source is reduced with 1 Hz/s from 50.0-47.0 Hz, while the active power set point of the converter, $P_{\mathrm{set}} = 0$ pu. The inertia constant is selected as $H = 5.0$ s, meaning that the specified frequency disturbance should result in an inertial power of 0.2 pu. Figure 3.6 demonstrates that the proposed controller is able to reproduce the behaviour of a SC with good accuracy. In case of a SC, an oscillatory inertial response can be observed due to its poor damping. On the other hand, with a flexibility to choose any desired value of ζ in the proposed controller,

a well-damped response without overshoot can be achieved for $\zeta = 1.0$. However, to reduce the rise time, a damping ratio of $\zeta = 0.707$ is suggested as a compromise between speed and damping of the inertial response.

3.3.2 Calculation of active-power limits

As stated earlier, the phase of the virtual back-EMF is a resultant of the active-power flow from the converter. Therefore, setting the limits for the active-power reference would limit the resulting phase of the virtual back-EMF. During limitation, prioritizing active or reactive-power injection from the converter depends upon the grid-code requirements. Here, reactive-power injection is prioritized[3]; accordingly, the upper limit for the active-power reference, P_{ul}, is calculated as

$$P_{\mathrm{ul}} = \sqrt{S_{\mathrm{avail}}^2 - Q_{\mathrm{g}}^2}, \tag{3.16}$$

where S_{avail} denotes the available apparent power of the converter, and Q_{g} is the reactive power injected from the converter (or, eventually, the reactive power demanded by the grid codes). At any time instant, depending upon the PCC-voltage magnitude, E_{g}, the available apparent power of the converter to keep the current within its rated value is calculated as $S_{\mathrm{avail}} = \frac{S_{\mathrm{N}} E_{\mathrm{g}}}{E_{\mathrm{N}}}$, where S_{N} and E_{N} denote the rated power and voltage of the converter, respectively. If $Q_{\mathrm{g}} \geq S_{\mathrm{avail}}$ (this condition prevails during a voltage dip for instance, when the converter current momentarily rises above its rated value), the upper limit for the active-power reference is set to zero.

3.3.3 Calculation of voltage-magnitude limits

The limits for the magnitude of virtual back-EMF can be calculated by using the estimated power flow. Considering the sign convention for the current in Fig. 3.1, a decrease in the PCC voltage will result in a positive reactive-power injection into the grid. Hence, the upper limit for the magnitude of the virtual

[3]Prioritization of active and reactive power can be modified depending upon the system requirements.

back-EMF, E_{ul}, is calculated as

$$E_{\mathrm{ul}} = \left| \underline{e}_{\mathrm{g}} + \frac{P^{\star}_{\mathrm{lim}} - jQ_{\mathrm{avail}}}{\mathrm{conj}(\underline{e}_{\mathrm{g}})} (R_{\mathrm{v}} + jX_{\mathrm{v}}) \right|; \quad \text{with } Q_{\mathrm{avail}} = \sqrt{S^2_{\mathrm{avail}} - P^{\star 2}_{\mathrm{lim}}}. \tag{3.17}$$

Similarly, if a voltage swell at the PCC is to be considered, the lower limit for the virtual back-EMF, E_{ll}, can be calculated accordingly, i.e.,

$$E_{\mathrm{ll}} = \left| \underline{e}_{\mathrm{g}} + \frac{P^{\star}_{\mathrm{lim}} + jQ_{\mathrm{avail}}}{\mathrm{conj}(\underline{e}_{\mathrm{g}})} (R_{\mathrm{v}} + jX_{\mathrm{v}}) \right|. \tag{3.18}$$

It is worth mentioning here that during limitation, $P^{\star}_{\mathrm{lim}}$ will be equal to P_{ul} as defined in (3.16). Thus, reactive-power injection is prioritized here. Furthermore, as $P_{\mathrm{g}} = P^{\star}_{\mathrm{lim}}$ during limitation, the angle of the voltage phasors $\underline{E}_{\mathrm{ul}}$ and $\underline{E}_{\mathrm{ll}}$ will be equal to zero in the controller's dq-reference frame.

In order to prevent the accumulation of the voltage error during limitation, an anti-windup loop with the gain K_{AW} is implemented in the ac-voltage controller (AVC) as shown in Fig. 3.4.

3.4 Experimental validation of the proposed current-limitation strategy

In order to validate the effectiveness of the proposed current-limitation strategy, experimental verification is made and discussed for various grid scenarios in this section. A photo of the laboratory setup is depicted in Fig. 3.7 and it resembles the system shown in Fig. 3.1. The grid is emulated using a REGATRON's four quadrant programmable AC power source. Furthermore, the GFM converter system used here comprises of a 2-level VSC supplied by an ideal DC voltage source. It is controlled using dSPACE dS1006, and is connected at the PCC through a phase reactor of resistance R_{f} and inductance L_{f}. Various system and control parameters used for the grid-interfaced converter system are shown in Table 3.1. The closed-loop bandwidths of the APL and AVC are chosen to comply with the recommendations for GFM control action defined in [17].

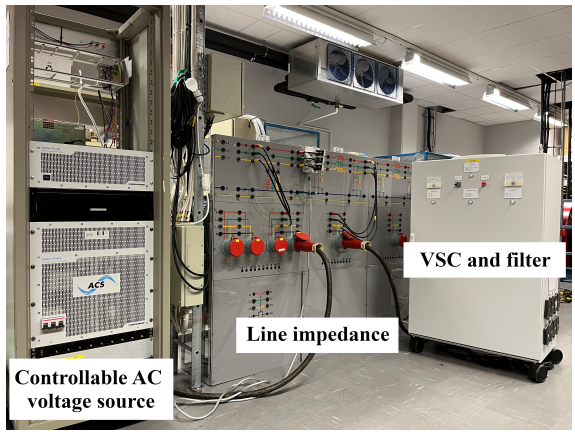

Figure 3.7: Photo of the laboratory setup.

Table 3.1: System and control parameters

System parameters		Control parameters	
S_N	1 kVA (1.0 pu)	L_v	0.5 pu
E_N	100 V (1.0 pu)	R_v	0.25 pu
ω_N	314.16 rad/s	α_pc	$2\pi5$ rad/s
L_f	0.15 pu	ζ	0.707
R_f	0.015 pu	α_cc	$2\pi500$ rad/s
SCR	3	$\alpha_\mathrm{vc} = 2\pi1$ rad/s	$K_\mathrm{d,vc} = 0.05$ pu

3.4.1 Dynamic performance in case of a RoCoF event

In order to investigate the dynamic performance of the GFM converter system during a RoCoF event, the frequency, f_s, of the voltage source behind grid impedance is varied from 50.0 Hz to 48.0 Hz at a rate of -2.0 Hz/s between 0.5 s and 1.5 s. The active power set-point of the converter is selected as 0.8 pu in this case. The blue curves in Fig. 3.8 show the dynamic response of the converter system emulating an inertia of 5.0 s using the proposed control structure and current-limitation strategy. For comparison, the dynamic performance of a converter system emulating the same amount of inertia within the APL and deploying circular-current limitation (henceforth referred as *Integrated GFM control*[4]) is shown with red curves in Fig. 3.8, where the upper-limit for the hard-current limiter is set to 1.1 pu.

It can be seen from the figure that by using the proposed control structure and current-limitation strategy, it is possible to limit the converter current close to its rated value without triggering the hard-current limiter. Additionally, the internal frequency of the converter closely follows the declining grid frequency (light-blue curve), i.e., the converter keeps its synchronism with the grid. Furthermore, the active-power flow from the converter is limited close to 1.0 pu which otherwise would have reached 1.2 pu without limitation (corresponding to set-point power of 0.8 pu and inertial power of 0.4 pu). On the other hand, due to the presence of inertia within the APL in the second case, the converter loses it synchronism when the maximum-current limit of the converter is reached.

3.4.2 Dynamic performance in case of a balanced three-phase voltage dip

In order to investigate the dynamic performance of the converter system during a balanced three-phase voltage dip, starting at 0.5 s, the magnitude of the source voltage, E_s, is reduced by 50% for a duration of 1.0 s. The set point for the active power is zero and inertia provision from the converter is minimized by deactivating the IEL for this case. Figure 3.9 shows the dynamic response of the GFM converter system against a balanced three-phase voltage dip.

[4]The integrated GFM control used here for comparison corresponds to the structure displayed in Fig. 3.1(b), which provides inertia by selecting a lower loop bandwidth for the APC resulting in the desired inertia.

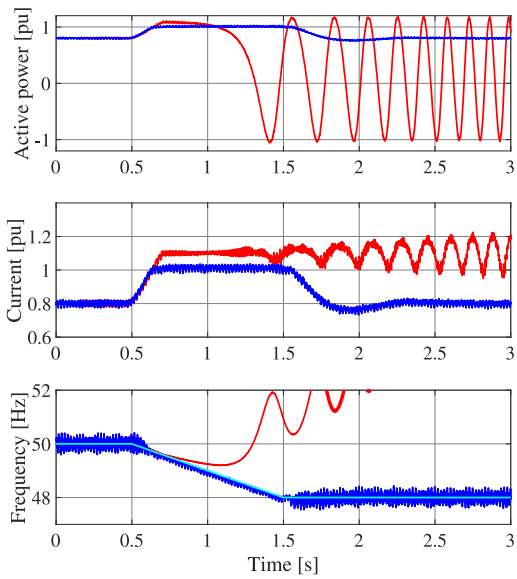

Figure 3.8: Dynamic response of GFM converter to a frequency disturbance with proposed control structure (blue curves), and Integrated GFM control (red curves). Top: measured active power; middle: measured converter-current magnitude; bottom: measured PCC frequency (light-blue curve depicts the frequency disturbance imposed by the controllable AC power source).

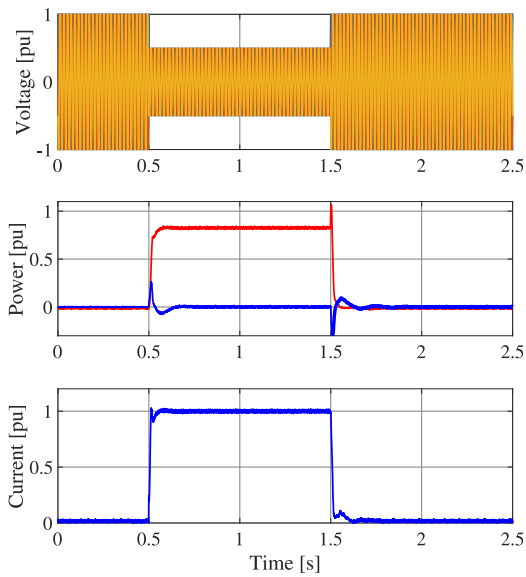

Figure 3.9: Dynamic response of GFM converter to a balanced three-phase voltage dip. Top: three-phase source voltage; middle: measured active (blue curve) and reactive power (red curve); bottom: measured converter-current magnitude.

It can be seen from the figure that following the voltage dip, the converter current is immediately limited close to its rated value without triggering the hard-current limiter, thus, without changing the converter's dynamics. Additionally, maximum reactive power (red curve) is injected from the converter instantaneously to support the system. It can also be observed that after the fault clearance, the active and reactive powers as well as the converter current immediately return to their initial operating points.

3.4.3 Dynamic performance in case of a balanced three-phase voltage dip accompanied by a RoCoF event

In order to investigate the dynamic performance of the converter during a balanced three-phase voltage dip accompanied by a RoCoF event, E_s is reduced as in the previous case. At the same time, f_s is varied from 50.0 Hz to 48.0 Hz at a rate of -2.0 Hz/s. Such a severe event, comprising of a combination of large voltage and frequency disturbance, might happen in extreme system conditions like the system event reported in [89] or during the 2021 European system split between France and Spain [90], and is here used to test the capabilities and robustness of the suggested converter control. Figure 3.10 shows the dynamic response of the GFM converter system emulating an inertia of 5.0 s for this case.

It can be observed from the figure that following the specified event, the converter current is immediately limited close to its rated value without triggering the hard-current limiter. Additionally, the converter injects maximum reactive power (red curve) instantaneously to support the system. Since the converter current reaches its rated value, there is no room for the active-power injection, and hence the active-power flow from the converter stays at zero. This results from the choice of prioritizing reactive power injection over active power made in (3.16). Since it's a matter of choice only, it is possible to reduce the reactive power injection if an inertial support is desired from the converter during limitation. It can also be observed that after the fault is cleared, the reactive power immediately returns to its initial operating point. Furthermore, the inertial response of the converter becomes evident from a decrease in the inertial power of the converter from the moment the frequency transient ends.

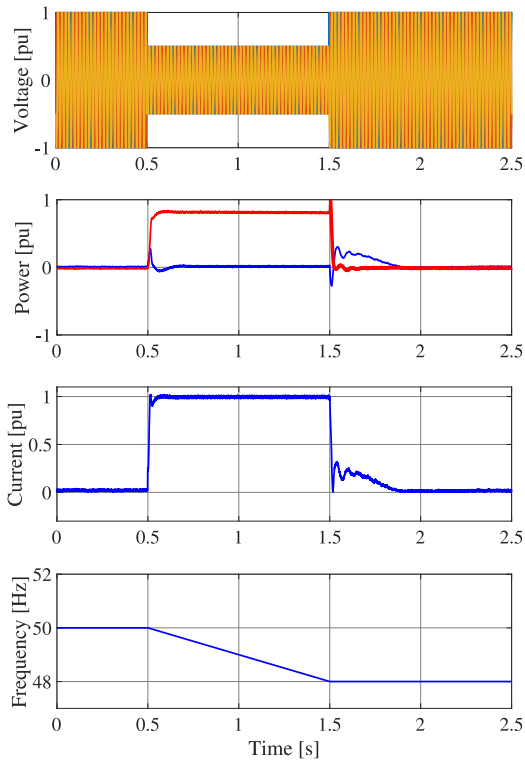

Figure 3.10: Dynamic response of GFM converter to a balanced three-phase voltage dip accompanied by a frequency disturbance. Top: three-phase source voltage; top-middle: measured active (blue curve) and reactive power (red curve); bottom-middle: measured converter-current magnitude; bottom: frequency disturbance imposed by the controllable AC power source.

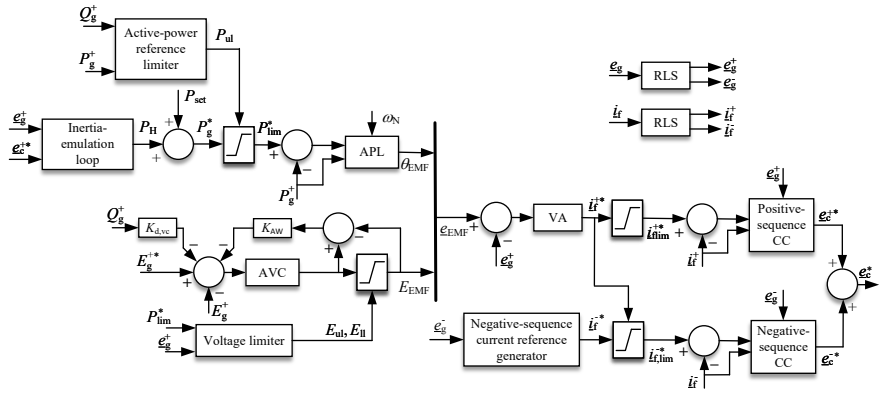

Figure 3.11: Block diagram of proposed control structure for GFM converters with adaptations for unbalanced grid conditions.

3.5 Controller modifications for unbalanced grid conditions

According to the latest reports from the ENTSO-e, GFM converters should act as a sink for unbalances in the grid voltage [7]. This means that in case of unbalanced grid conditions (for example, during unbalanced faults), the converter must offer an inductive behaviour towards the grid for the negative-sequence components. As an example, the recent VDE-AR-N 4120 Technical Connection Rules establishes requirements for the negative-sequence current injection from the grid-connected converter systems [91]. In particular, for an unbalanced voltage dip the converter should absorb a negative-sequence current proportional to the negative-sequence grid voltage, following the relation

$$I_{\mathrm{f}}^{-} = k_{\mathrm{n}} V_{\mathrm{g}}^{-}, \; 2 \leq k_{\mathrm{n}} \leq 6 \tag{3.19}$$

where the gain k_{n} specifies the relation between the magnitude of the negative-sequence component in the grid voltage, E_{g}^{-}, and the corresponding negative-sequence converter current I_{f}^{-}. During current limitation, prioritizing positive- or negative-sequence current depends upon the system requirements. This implies that we should be able to effectively control and limit both the positive- and negative-sequence currents individually. Figure 3.11 shows the modifica-

tions made to the controller for this purpose, where a negative-sequence CC has been added to the original control structure. It generates a negative-sequence reference voltage for the converter, $\underline{e}_{\mathrm{c}}^{-\star}$, which is added to the positive-sequence reference voltage, $\underline{e}_{\mathrm{c}}^{+\star}$, generated by the original control structure.

During unbalanced grid conditions, the magnitude of the voltage and current vectors, as well as the instantaneous active and reactive powers will present oscillations at twice the fundamental frequency. This will lead to double-frequency oscillations in both the internal frequency of the converter and magnitude of the virtual back-EMF. To prevent this, positive-sequence components of the measured voltages and currents are used as inputs in the APL and AVC, while the negative-sequence components for the negative-sequence CC. A Recursive Least Square (RLS) algorithm based method is used here to separate the voltage and current vectors into their respective sequence components [92]. To adapt to the changes in the grid frequency, the internal frequency of the converter is used as an input to the RLS-based sequence separator.

In accordance with the relation between negative-sequence voltage and current provided in (3.19), the converter should exhibit negative-sequence reactance, $X_{\mathrm{n}} = k_{\mathrm{n}}^{-1}$. Therefore, the reference for the negative-sequence CC, $\underline{i}_{\mathrm{f}}^{-\star}$, is calculated as

$$\underline{i}_{\mathrm{f}}^{-\star} = \frac{\underline{e}_{\mathrm{g}}^{-}}{jX_{\mathrm{n}}}, \tag{3.20}$$

where $\underline{e}_{\mathrm{g}}^{-}$ represents the negative-sequence component of the PCC-voltage vector. The factor, k_{n}, is selected here equal to 2. Circular limitation is used for the negative-sequence current in order to keep the total converter current within its rated value, I_{N}. Giving positive-sequence current priority for active and reactive-power support, the upper and lower limits for the magnitude of the negative-sequence current reference, denoted by $I_{\mathrm{f,ul}}^{-}$ and $I_{\mathrm{f,ll}}^{-}$, respectively, are calculated as

$$\begin{aligned} I_{\mathrm{f,ul}}^{-} &= I_{\mathrm{N}} - I_{\mathrm{f}}^{+\star}, \\ I_{\mathrm{f,ll}}^{-} &= -I_{\mathrm{f,ul}}^{-}. \end{aligned} \tag{3.21}$$

$I_{\mathrm{f}}^{+\star}$ denotes the magnitude of the positive-sequence current reference and is calculated as $I_{\mathrm{f}}^{+\star} = \sqrt{(i_{\mathrm{f,d}}^{+\star})^2 + (i_{\mathrm{f,q}}^{+\star})^2}$. During limitation, the magnitude

of the negative-sequence current reference, $I_{\mathrm{f}}^{-\star}$, is saturated at its upper or lower limit according to (3.21). On the other hand, its phase angle, i.e., $\angle \underline{i}_{\mathrm{f}}^{-\star}$ is kept unchanged and is determined using (3.20).

3.5.1 Experimental validation under unbalanced grid conditions

The following test cases validate the effectiveness of the proposed limitation strategy during unbalanced grid conditions. The set point for the active-power flow from the converter is zero for the case studies presented here.

Dynamic performance in case of a small unbalance

In order to investigate the dynamic performance of the converter during a small unbalance, the magnitude of the source voltage in phase B and C is reduced by 30% for a duration of 1.0 s. Figure 3.12 shows the dynamic response of converter system for this case.

It can be observed from the figure that following the specified disturbance, the converter injects reactive power (red curve) to boost the positive-sequence voltage at the PCC. Since $k_{\mathrm{n}} = 2$, the converter exhibits a negative-sequence reactance of 0.5 pu (calculated by dividing the measured negative-sequence voltage with resulting negative-sequence current during unbalance), hence allowing the negative-sequence current to flow. Furthermore, the positive sign of negative-sequence reactance confirms the inductive behaviour of the converter to counter unbalance in the PCC voltage.

Dynamic performance in case of a severe unbalance

In order to investigate the dynamic performance of the converter against a severe unbalance, the magnitude of the source voltage in phase B and C is reduced by 80% for a duration of 1.0 s. Figure 3.13 shows the dynamic response of converter system for this case. It can be observed from the figure that giving positive-sequence current priority over the negative sequence results in an injection of maximum reactive power (red curve) from the converter. Since the converter current reaches its rated value, there is no room left for the negative-sequence current to flow, i.e, $\underline{i}_{\mathrm{f}}^{-\star}$ is automatically set to zero from (3.21). Consequently, the measured converter current is composed of positive-

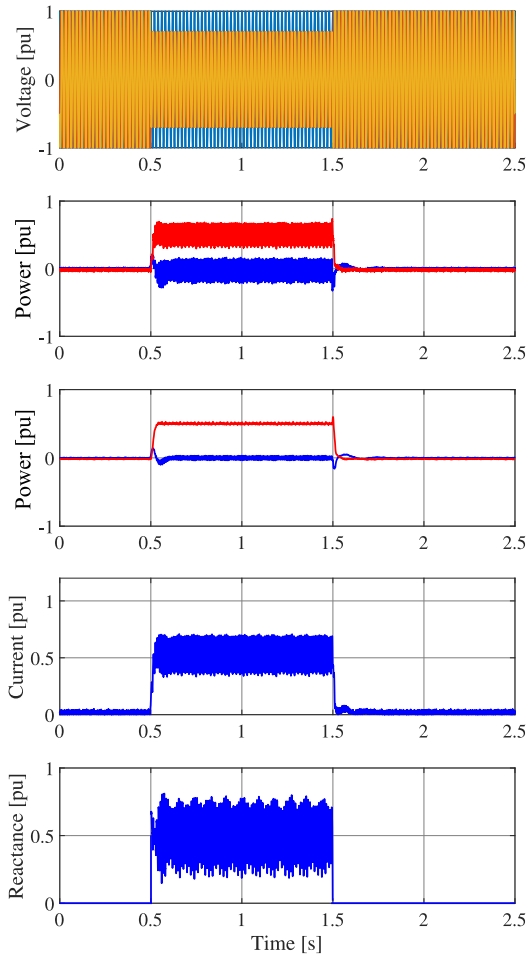

Figure 3.12: Dynamic response of GFM converter to a shallow unbalanced voltage dip. From top to bottom: three-phase source voltage, measured active (blue curve) and reactive power (red curve), measured positive-sequence active (blue curve) and reactive (red curve) power, measured converter-current magnitude, measured negative-sequence reactance of the converter.

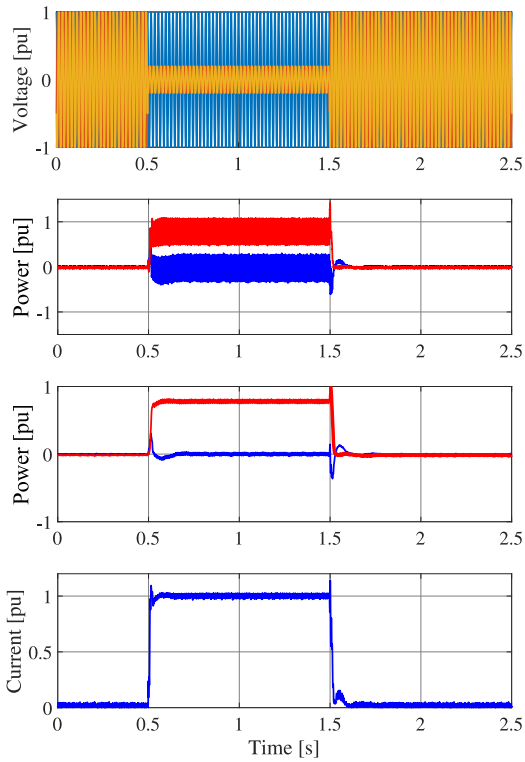

Figure 3.13: Dynamic response of GFM converter to a severe unbalanced voltage dip. From top to bottom: three-phase source voltage, measured active (blue curve) and reactive power (red curve), measured positive-sequence active (blue curve) and reactive (red curve) power, measured converter-current magnitude.

sequence component only unlike the current in Fig. 3.12, where the 100.0 Hz oscillation due to negative-sequence component is evident.

3.6 Summary

In this chapter, a novel current limitation strategy for GFM converters has been presented. The causes for instability in case of large disturbances with existing current limitation strategies for GFM converters have been discussed. In order to guarantee converter's stability and at the same time preserve its GFM behaviour also during current limitation, a novel limitation strategy has been presented. In the proposed strategy, current limitation is achieved by dynamically limiting the virtual back-EMF vector. Experimental results show the ability to effectively limit the current output of the converter to the desired value for several system events, without the need to activate the reference-current limiter at the input of the CC. Furthermore, modifications to cope with unbalanced grid conditions and fulfill the related grid codes have been presented.

CHAPTER 4

Grid-forming wind power plants

4.1 Introduction

In the previous chapter, the proposed GFM control strategy for a generic grid-connected converter has been presented. This chapter focuses more on the application of this control strategy in wind power plants (WPPs). There has been a rapid increase in the number of wind power installations over the past two decades. According to the data from GWEC, onshore wind capacity has grown from 178 GW in 2010 to 774 GW in 2021; whereas, offshore wind has grown proportionately more, i.e., from 3.1 GW in 2010 to 55.7 GW in 2021 with a forecast to rise over 380 GW by 2030 [93], [94]. This substantial increase in the offshore wind power is mainly driven by its higher generation capacity and more stable wind conditions as compared to its onshore counterpart. Furthermore, with the advancement in modern technologies such as static synchronous compensator (STATCOM) and STATCOM integrated with energy storage system (here referred as ES-STATCOM) [95]–[99], it has become technically possible to use High Voltage Alternating Current (HVAC) solutions for the grid connection of wind farms that are located far from the shore [65], [100]–[107]. Avoiding the use of High Voltage Direct Current (HVDC)

technology for power transmission and grid-code fulfillment and expanding the potential of HVAC technology instead, significantly reduces the cost of installation for wind power plants (WPPs) [108], [109]. Consequently, there is a growing interest among system operators and wind power plant owners for such system configurations. Some examples of the ac connected offshore wind farms include Hornsea One and Two in the UK with their 120 km and 90 km distance from the shore, respectively [110], [111].

However, use of the long power transmission cables in HVAC-WPPs, may result in a low SCR at the WT terminals, thereby making the offshore grid weaker. Furthermore, interaction between the WTs and shunt compensators, which are typically used in such systems to provide reactive power compensation, can induce undesirable resonances, thereby posing challenges for a stable system operation [112], [113]. The study performed in this chapter is aimed at assessing the potential of an ES-STATCOM operated using the proposed GFM control strategy to improve the dynamic performance of a WPP during weak grid conditions and offer a certain degree of the GFM capability to the overall WPP[1]. In order to take into account various resonances occurring due to the long ac cables and various shunt compensators, the model of a realistic WPP is considered here and first presented. This is followed by a description of the control strategy used for the WTs. Furthermore, the GFM capability of the considered WPP is assessed by evaluating the dynamic performance of the WPP in response to various grid disturbances stated in Section 2.2, using EMT simulations. Finally, using the Network Frequency Perturbation (NFP) plots, the GFM behaviour of the WPP is verified.

4.2 Description of the investigated system

Figure 4.1 shows the single-line diagram of the investigated system, which is based on the Hornsea Two offshore WPP [114]–[116]. The considered WPP has 54 WT units rated 8 MW, 690 V and 0.9 power factor. The WT units are aggregated into 6 groups, each comprising of 9 WT units. There are two 270 MVA, 66/220 kV step-up transformers at the collector bus. Each transformer has three 66 kV collector feeders with a total of 27 WT units connected. The 66 kV collector feeders are represented by an equivalent series

[1]The total system comprising of the WTs, ac export cable network and associated shunt compensators and the ES-STATCOM is referred here as the WPP.

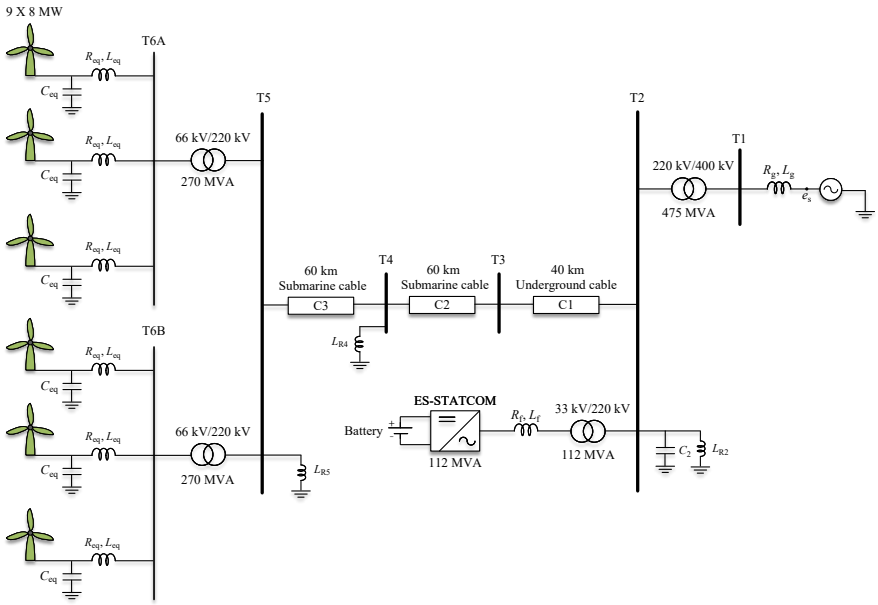

Figure 4.1: Single-line diagram of the considered WPP.

impedance of resistance, $R_{\text{eq}} = 0.68\ \Omega$, inductance, $L_{\text{eq}} = 5.2$ mH, and shunt capacitance, $C_{\text{eq}} = 5.1\ \mu$F, on the WT side. The 220 kV export cable network comprises of 40 km long underground cable (C1) in flat layout and two sections of submarine cables (C2 and C3) each 60 km long. The submarine cables have a trefoil layout inside a pipe. There is a 300 MVAr shunt reactor and 80 MVAr shunt capacitor at the bus T2, 170 MVAr shunt reactor at the bus T4 and 90 MVAr shunt reactor at the bus T5 providing reactive power compensation. In addition, a 112 MVA, 33 kV ES-STATCOM connected at the bus T2 through a 112 MVA, 33/220 kV step-up transformer is used to regulate the bus voltage. The WPP is connected to the 400 kV onshore grid through a 475 MVA 220/400 kV step-up transformer. The onshore ac grid is represented by its Thévenin's equivalent, comprising of a 400 kV ideal-voltage source behind a grid impedance. The grid impedance is set in accordance to the desired SCR at the grid terminals. The leakage reactance of all the transformers is selected as 0.1 pu.

In order to retain as much of the transient response characteristics as possi-

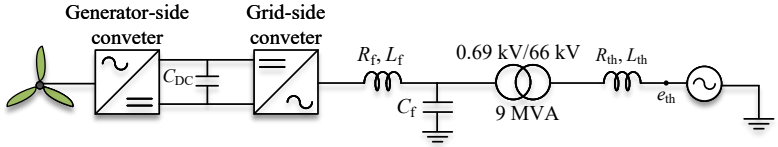

Figure 4.2: Single-line diagram of the considered WT system.

ble, the 220 kV export cables are modelled using the cable modelling toolbox in PSCAD and the data available from the industrial partners is utilized for the geometrical core and layout details of the cables. Furthermore, the magnetic saturation of the transformer core is modelled in terms of the magnetizing current (which is assumed to be 0.5%), air-core reactance (assumed to be twice the leakage reactance), and the knee point voltage (which is assumed to be 1.17 pu).

4.3 Description of the wind turbine controller

The WT system considered here is constituted by a rotating machine (which could be a classical wound rotor or permanent magnet synchronous machine, or squirrel cage induction machine) connected to the grid through a back-to-back converter, as depicted in Fig. 4.2. As the dc-link of the back-to-back converter decouples the machine-side ac system from the grid under normal system operations, the equivalent circuit in Fig. 4.3 can be employed for analysis purpose, where a variable current source is used to represent the machine side and the rectifier stage of the WT [79]. The main control loops of the WT as shown in Fig. 4.3 are implemented in the rotating *dq*-reference frame, which is defined using the estimated grid-voltage angle obtained from the PLL, $\hat{\theta}_{\mathrm{g}}$, and is aligned with the measured grid-voltage vector. Therefore, the estimated angle from the PLL is given by

$$\hat{\theta}_{\mathrm{g}} = \frac{1}{s}(K_{\mathrm{p,PLL}} + \frac{K_{\mathrm{i,PLL}}}{s})\tan^{-1}(\frac{e_{\mathrm{g}}^{q}}{e_{\mathrm{g}}^{d}}) + \frac{\omega_{\mathrm{N}}}{s}, \tag{4.1}$$

where $K_{\mathrm{p,PLL}}$ and $K_{\mathrm{i,PLL}}$ represent the proportional and integral gains of the PLL, respectively. With α_{PLL} denoting the loop bandwidth of the synchronization algorithm, these gains are selected as $K_{\mathrm{p,PLL}} = 2\alpha_{\mathrm{PLL}}$ and

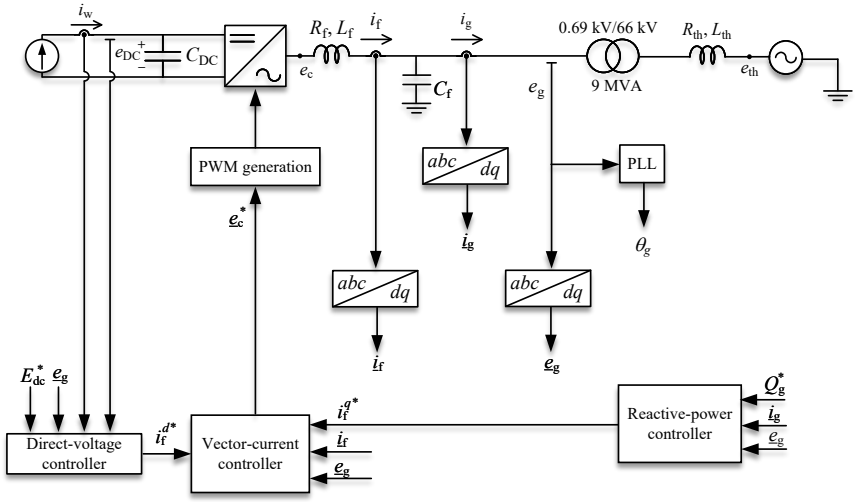

Figure 4.3: WT main circuit diagram and control system.

$K_{\mathrm{i,PLL}} = \alpha_{\mathrm{PLL}}^2$ [79].

As shown in Fig.4.3, the control algorithm for WT has a cascade structure, with an inner ac-current controller and two outer-loop controllers, namely, the reactive-power controller and dc-voltage controller. The reactive-power and dc-voltage controllers generate the reference reactive- and active-current components, respectively, for the inner vector-current controller that calculates the converter voltage reference, $\underline{e}_{\mathrm{c}}^{\star}$, for the modulation stage of the converter. A similar structure of the current controller as the one described in Section 2.4.1 is used here.

The reactive-power controller is used to regulate the reactive power, Q_{g}, injected by the WT to the grid. It calculates the reference reactive-current component, $i_{\mathrm{f}}^{q\star}$, as

$$i_{\mathrm{f}}^{q\star} = \frac{K_{\mathrm{i,qc}}}{s} \frac{(Q_{\mathrm{g}}^{\star} - Q_{\mathrm{g}})}{H_{\mathrm{qc}} E_{\mathrm{g}}}, \tag{4.2}$$

where $Q_{\mathrm{g}}^{\star}$ denotes the reference reactive power. H_{qc} is the transfer function of a low-pass filter for the measured instantaneous grid-voltage magnitude. With α_{qc} denoting the closed-loop bandwidth of the reactive-power controller, the

integral gain is selected using the loop-shaping approach as $K_{\mathrm{i,qc}} = -\alpha_{\mathrm{qc}}$ [79].

The dc-voltage controller is used to regulate the direct voltage, E_{dc}, of the converter, which is measured across the dc capacitance, C_{dc}. It calculates the reference active-current component, $i_{\mathrm{f}}^{d\star}$, as [82]

$$i_{\mathrm{f}}^{d\star} = \frac{K_{\mathrm{p,dc}}(E_{\mathrm{dc}}^{\star 2}/2 - E_{\mathrm{dc}}^{2}/2) + H_{\mathrm{dc}}P_{\mathrm{w}}}{H_{\mathrm{dc}}E_{\mathrm{g}}}, \tag{4.3}$$

where $E_{\mathrm{dc}}^{\star}$ is the reference dc voltage of the converter. The power from the machine-side converter in the WT, $P_{\mathrm{w}} = E_{\mathrm{dc}}I_{\mathrm{w}}$ (see Fig.4.3), is filtered using a low-pass filter represented by the transfer function H_{dc} and added as a feed-forward term in (4.3) to enhance the system dynamics. With α_{dc} denoting the closed-loop bandwidth of the dc-voltage controller, the proportional gain is selected as $K_{\mathrm{p,dc}} = -\alpha_{\mathrm{dc}}C_{\mathrm{dc}}$ [82].

4.4 Evaluation of the grid-forming capability of the wind power plant

In this section, the GFM capability of the WPP shown in Fig. 4.1 is assessed, when the proposed GFM control strategy (see Fig. 3.11) is adopted for the ES-STATCOM, while the conventional GFL control described in the previous section is implemented for the WTs. Several case studies are presented showing the dynamic performance of the WPP in response to various grid disturbances. These case studies are mainly motivated by the recently issued guidelines from the German VDE FNN [117], which specifies test case scenarios for the verification of the GFM behaviour of the converter systems. The following scenarios are examined for the verification of conformity:

- Phase-angle jump in the onshore grid.
- Linear frequency change in the onshore grid.
- Voltage jump in the onshore grid.
- Presence of a negative-sequence component in the onshore grid.
- Change in the grid impedance.

Table 4.1: System and control parameters for the WT system

System parameters		Control parameters	
S_{N}	8.89 MVA (1.0 pu)	α_{cc}	$2\pi500$ rad/s
E_{N}	0.69 kV (1.0 pu)	α_{ff}	$2\pi500$ rad/s
ω_{N}	314.16 rad/s	α_{dc}	$2\pi5$ rad/s
R_{f}	0.012 pu	α_{qc}	$2\pi5$ rad/s
L_{f}	0.12 pu	α_{PLL}	$2\pi5$ rad/s
C_{f}	0.02 pu		

Table 4.2: System and control parameters for the ES-STATCOM

System parameters		Control parameters	
S_{N}	112 MVA (1.0 pu)	$R_{\mathrm{v}} = 0.25$ pu	$L_{\mathrm{v}} = 0.5$ pu
E_{N}	33 kV (1.0 pu)	α_{pc}	$2\pi5$ rad/s
ω_{N}	314.16 rad/s	$H = 5.0$ s	$\zeta = 0.707$
L_{f}	0.05 pu	$\alpha_{\mathrm{cc}} = 2\pi500$ rad/s	$\alpha_{\mathrm{ff}} = 2\pi500$rad/s
R_{f}	0.005 pu	$\alpha_{\mathrm{vc}} = 2\pi1$ rad/s	$K_{\mathrm{d,vc}} = 0.05$ pu

In order to investigate the dynamic performance of the WPP, a detailed time-domain simulation model of the test network shown in Fig. 4.1 has been implemented in PSCAD. The system and control parameters used for the WTs and ES-STATCOM are listed in Table 4.1 and 4.2, respectively. For all the test cases, the following conditions apply unless stated explicitly; the WPP is operated at half of its nominal value, the reactive power set-point of the WTs and active power set-point of the ES-STATCOM is zero, and the voltage at the bus 'T2' of the WPP is regulated at its rated value by the ES-STATCOM. Furthermore, SCR of 4.0 is selected at the onshore grid terminal. Accordingly, the magnitude of the grid impedance is calculated as, $Z_{\mathrm{g}} = \frac{400^2}{4*432} = 92.59\ \Omega$, and a grid-impedance angle of 88° is assumed. Finally, all the case studies assume a stiff dc voltage for the ES-STATCOM, which implies assuming that a battery bank of sufficient capacity is connected at its input.

4.4.1 Phase-angle jump in the onshore grid

In order to evaluate the dynamic performance of the WPP during phase-angle jumps, the phase angle of the source voltage, ϕ_{s}, is changed from 0° to -10° at 0.5 s, from -10° to -40° at 2.5 s, and from -40° to -100° at 4.5 s. Figure 4.4

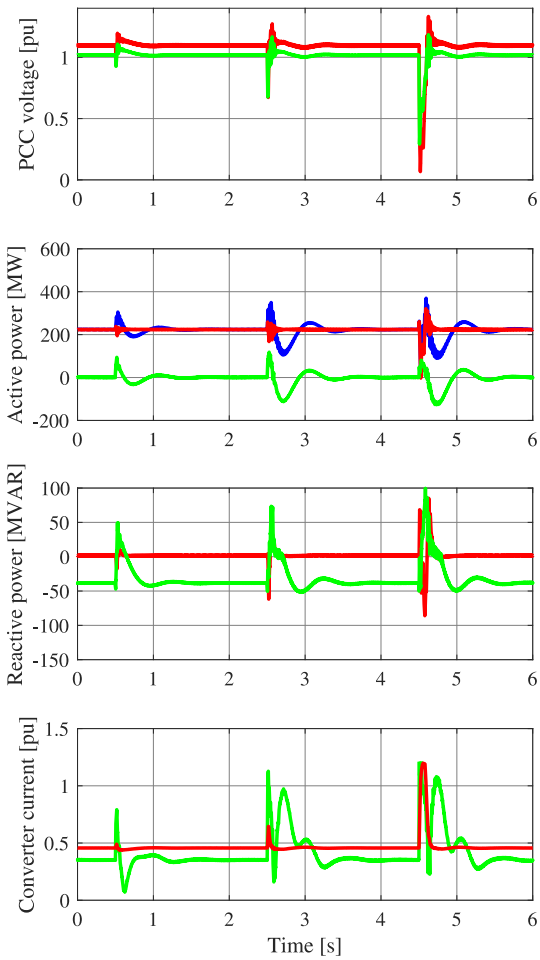

Figure 4.4: Dynamic response of the WPP to phase-angle jumps. From top to bottom: voltage magnitude on the LV side of the WT transformer (red curve) and HV side of the ES-STATCOM transformer (green curve); active power output of the WTs (red curve), ES-STATCOM (green curve) and WPP (blue curve); reactive power output of the WT (red curve) and ES-STATCOM (green curve); output current of the WT converter (red curve) and ES-STATCOM (green curve).

shows the dynamic performance of the WPP for the specified event. It can be observed from the figure that following the grid disturbance, WTs (red curves) do not inject any significant amount of active power to the grid. This is because the PLL in the WT converter tracks the change in the grid-voltage angle within a few ms, thereby letting the current controller keep the active current (hence the active power) at its reference value. On the other hand, the ES-STATCOM (green curves) instantaneously injects active power to resist to the changes in the phase angle of the grid. Based on its dynamics, the APL finally drives the active power back to its initial value. Due to presence of virtual inertia ($H = 5.0$ s) in the ES-STATCOM, a power swing can be observed in the active power output of the converter and consequently in the active power output of the WPP (blue curve). Thanks to the proposed tuning criteria of the IEL and APL of the ES-STATCOM, the power swing is well damped.

Furthermore, following a phase-angle jump in the onshore grid, a voltage drop on the low-voltage (LV) side of the WT transformer as well as on the high-voltage (HV) side of the ES-STATCOM transformer (controlled side) can be observed from the plots of the PCC voltage. As a consequence, the ES-STATCOM instantaneously injects reactive power to boost the voltage, thereby supporting operation of the WPP. Since a larger phase-angle jump results in a larger voltage drop, a higher reactive-power injection from the ES-STATCOM takes place for larger angular jumps. By virtue of the proposed control structure and current-limitation strategy for the ES-STATCOM, the WPP is able to successfully ride-through large phase-angle jumps of -30° and -60° in the onshore grid without losing stability or exceeding the current limit of any of the converters, and supporting the grid to its full potential.

4.4.2 Linear frequency change in the onshore grid

In order to investigate the dynamic performance of the WPP during a RoCoF event, the frequency, f_s, of the source voltage is varied from 50.0 Hz to 48.0 Hz at a rate of -2.0 Hz/s between 0.5 s and 1.5 s, and from 48.0 Hz to 50.0 Hz at a rate of 2.0 Hz/s between 2.5 s and 4.0 s. Figure 4.5 shows the dynamic performance of the WPP during this event. It can be observed from the figure that due to the fast tracking behaviour of the PLL, there is no change in the active-power response of the WTs during frequency disturbance. On the other hand, it can be seen from the figure that immediately after the frequency drop

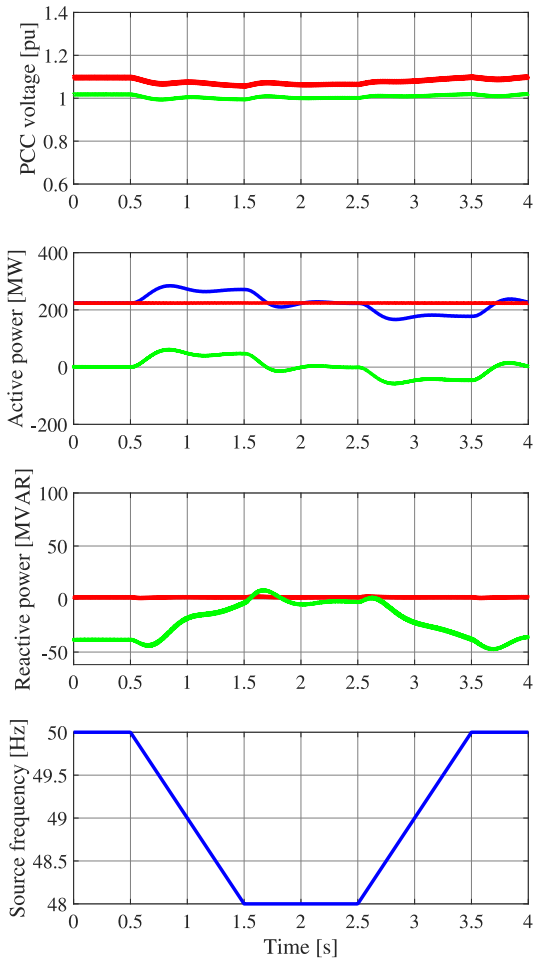

Figure 4.5: Dynamic response of the WPP to a frequency disturbance. From top to bottom: voltage magnitude on the LV side of the WT transformer (red curve) and HV side of the ES-STATCOM transformer (green curve); active power output of the WTs (red curve), ES-STATCOM (green curve) and WPP (blue curve); reactive power output of the WT (red curve), ES-STATCOM (green curve); applied variation in the source frequency.

in the grid, the ES-STATCOM injects active power proportional to the RoCoF (inertial power), thus contributing to the total system inertia. Since the virtual-inertia constant of the ES-STATCOM is $H = 5.0$ s, the inertial power in this case corresponds to $P_{\mathrm{H}} = \frac{2H}{\omega_{\mathrm{N}}} \frac{d\omega}{dt} S_{\mathrm{N}} = 45$ MW. Furthermore, since the frequency drop results in an increase of the equivalent shunt capacitive reactance of the cable network, there is a decrease in the reactive power generated by the cable network. Correspondingly, the reactive power absorbed by the ES-STATCOM is reduced in order to regulate the voltage. As expected, an opposite behavior can be observed from the WPP during frequency rises.

4.4.3 Voltage jump in the onshore grid

In order to evaluate the dynamic performance of the WPP during a voltage jump in the onshore grid, the magnitude of the source voltage is reduced to 0.8 pu at 0.5 s for a duration of 1.0 s. Figure 4.6 shows the dynamic response of the WPP in response to the applied grid disturbance. From the obtained results it can be observed that due to the intrinsic voltage-source behaviour of the ES-STATCOM, an instantaneous injection of reactive power takes place without relying on any control action. The ac-voltage controller of the ES-STATCOM comes into action only after a few ms. Due to the proposed current-limitation approach and in accordance with (3.16) and (3.17), the injection of reactive power from the ES-STATCOM takes place to its maximum value (limited by the current rating of the converter and the available voltage at the PCC). Accordingly, the voltage at the terminals of the WPP is restored close to its rated value. However, as mentioned in Chapter 3, the controller can also be designed in such a way that the reactive-power injection follows the grid codes. The speed of restoration of the voltage is dictated by the closed-loop bandwidth of the ac-voltage controller of the ES-STATCOM, which in this case is set to 2π rad/s.

4.4.4 Presence of a negative-sequence component in the onshore grid

In order to evaluate the dynamic performance of the WPP in case of an unbalance in the onshore grid, a negative-sequence voltage of magnitude 0.02 pu is superimposed with the ideal-voltage source starting at 0.5 s. Figure 4.7 compares the variation in the voltage magnitude of the source (blue curve)

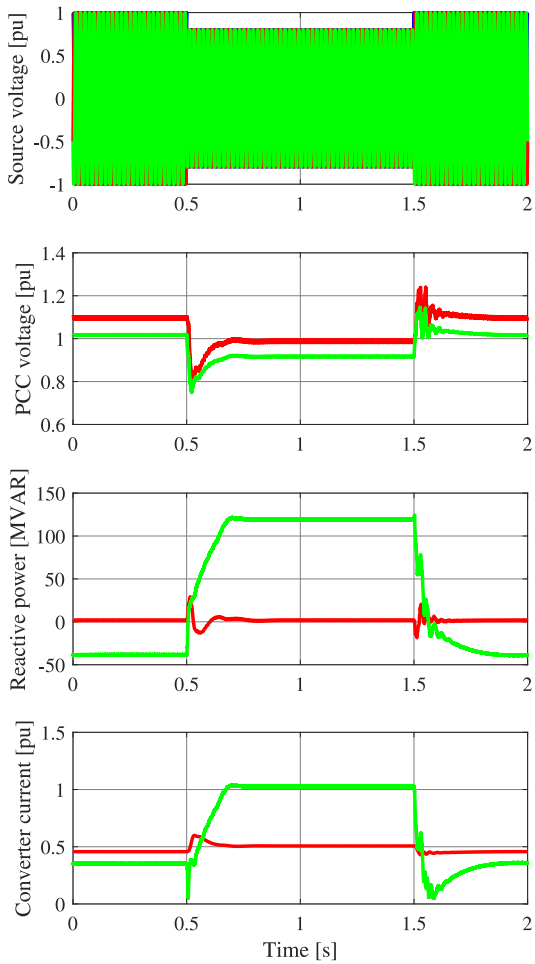

Figure 4.6: Dynamic response of the WPP to a voltage jump. From top to bottom: three-phase source voltage; voltage magnitude on the LV side of the WT transformer (red curve) and HV side of the ES-STATCOM transformer (green curve); reactive power output of the WT (red curve) and ES-STATCOM (green curve); output current of the WT converter (red curve) and ES-STATCOM (green curve).

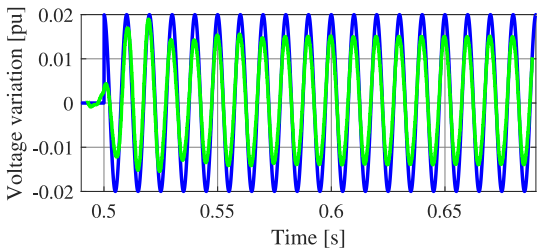

Figure 4.7: Variation in the voltage magnitude of the source (blue curve) and at the HV side of the ES-STATCOM transformer (green curve) following an unbalance in the onshore grid.

and at the HV side of the ES-STATCOM transformer (green curve). Lower variation in the voltage magnitude at the onshore connection point of the WPP indicates an improvement in the voltage quality. This is mainly due to the inductive behaviour of the ES-STATCOM, which confirms the ability of the WPP to act as a sink to counter harmonics and unbalances in the grid.

4.4.5 Change in the grid impedance

In order to investigate the dynamic performance of the WPP during variation in the grid strength, the SCR of the grid is changed dynamically from 4.0 to 2.67 at 0.5 s and from 2.67 to 1.33 one second later. Figure 4.8 shows the dynamic performance of the WPP in response to the applied disturbance. Since the grid reactance increases with a decrease in the SCR, it can be observed from the figure that there is an instantaneous decrease in the active power output of the WPP. This results in an instantaneous absorption of active power in the ES-STATCOM. Based on its dynamics, the APL of the ES-STATCOM drives the active power back to its initial value. The power swing observed in the figure is once again a resultant of the virtual inertia in the ES-STATCOM. Due to an increase in the grid reactance, the network becomes more and more inductive resulting in a decrease of the reactive power absorbed by the ES-STATCOM, and consequently a decrease in the output current of the ES-STATCOM during steady state. Moreover, a stable operation of the WPP is observed during sudden changes in the grid strength.

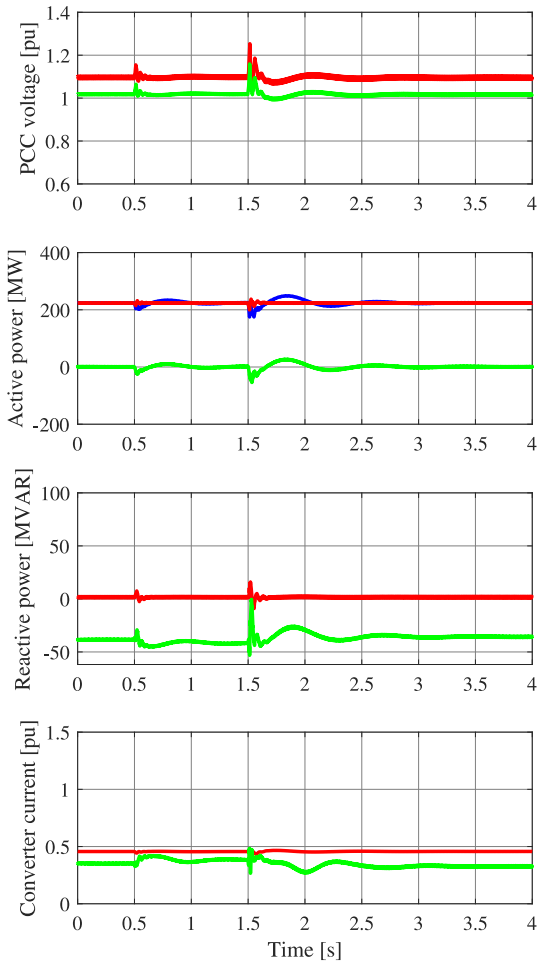

Figure 4.8: Dynamic response of the WPP to changes in the grid strength. From top to bottom: voltage magnitude on the LV side of the WT transformer (red curve) and HV side of the ES-STATCOM transformer (green curve); active power output of the WTs (red curve), ES-STATCOM (green curve) and WPP (blue curve); reactive power output of the WT (red curve) and ES-STATCOM (green curve); output current of the WT converter (red curve) and ES-STATCOM (green curve).

4.5 Network Frequency Perturbation (NFP) plot

The simulation tests performed in the previous section indicate a GFM behaviour of the WPP. To further verify this property, the NFP plots described here are used. The NFP plot was first introduced in [118]. It graphically shows the amplitude and phase of the active-power response of a device under testing (DUT), when the voltage waveform of the distant upstream "infinite bus" is frequency modulated with subsynchronous frequencies from 0 Hz to 20 Hz or optionally close to the fundamental [118]. Therefore, the NFP plot essentially indicates the frequency response of the closed-loop transfer function from the input grid-frequency variation to the output active-power variation of a device. The Bode type plots obtained from this method give a graphical insight of various GFM properties of a device, such as its contribution towards damping and total system inertia, as described in this section. The NFP plot is here used to asses the GFM behaviour of the considered WPP.

4.5.1 Methodology to generate the NFP plot and its interpretation

The NFP plot can be obtained from either a time-domain simulation, followed by the Fourier analysis, or from the linear analysis of the system and obtaining a closed-loop transfer function from the input grid-frequency variation to the output active-power variation of a device (or system). In order to generate the NFP plot from time-domain simulation, the DUT is placed in a test network as shown in Fig. 4.9. The frequency of the source voltage, f_{s}, is modulated in a sinusoidal fashion around the nominal frequency, f_{N}, with a small frequency deviation of amplitude Δf_{s} applied at frequency f_{NFP}. This can be expressed as

$$f_{\mathrm{s}}(t) = f_{\mathrm{N}} + \Delta f_{\mathrm{s}} \cos(2\pi f_{\mathrm{NFP}} t + \phi_{\Delta \mathrm{f_s}}), \tag{4.4}$$

where $\phi_{\Delta \mathrm{f_s}}$ represents the phase of the applied modulation. The amplitude of the frequency modulation, Δf_{s}, should be kept small such that saturation of neither of the control loops is triggered. The modulation frequency, f_{NFP}, is swept across a broad range, from approximately 10^{-2} Hz to 20 Hz or optionally close to the fundamental frequency of the ac network. The DUT responds to

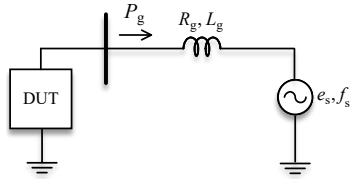

Figure 4.9: Test network for generating the NFP plot.

this changing frequency with a modulated active-power output given by

$$P_g(t) = P_{set} + \Delta P_g \cos(2\pi f_{NFP} t + \phi_{\Delta P_g}). \tag{4.5}$$

It shall be noted here that the power is in pu, while the frequency is in Hz.

Using the stimulus (4.4) and the measured active power output of the DUT as in (4.5), the NFP response, $\underline{R}_{NFP}$, can be calculated as

$$\underline{R}_{NFP} = \frac{\Delta P_g \angle \phi_{\Delta P_g}}{\frac{\Delta f_s}{f_N} \angle \phi_{\Delta f_s}}, \tag{4.6}$$

where the amplitude and phase of the active-power variation, i.e., ΔP_g (in pu) and $\phi_{\Delta P_g}$, respectively, are calculated from the Fourier analysis of the response. The amplitude and phase of the stimulus, i.e., Δf_s and $\phi_{\Delta f_s}$, respectively, are also calculated from the Fourier analysis so that the NFP response is correctly determined. The frequency of the stimulus is normalized to obtain the overall amplitude response in pu. The NFP amplitude plot shows $|R_{NFP}|$ (in pu) on the y-axis and modulation frequency, f_{NFP} (in Hz), on the x-axis. The plot is best made by plotting both axes in the logarithmic scale. The y-axis is interpreted as the amplitude of the sinusoidal variation in the active power output of the device (in pu) in response to a 1.0 pu amplitude sinusoidal grid-frequency modulation at f_{NFP}. Similarly, the NFP phase plot shows $\angle R_{NFP}$ (in °) on the y-axis and f_{NFP} (in Hz) on the x-axis.

As mentioned earlier, it is possible to obtain the NFP plot from the classical linear analysis of the system. To exemplify this, the classical model of a SG as the one shown in Fig 4.10 is considered. From the swing equation

$$M \frac{d\omega_r}{dt} = P_m - P_g - P_d; \quad M = \frac{2H}{\omega_N}, \tag{4.7}$$

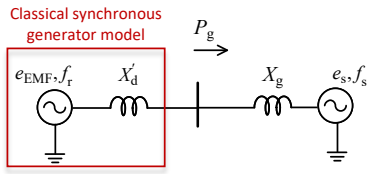

Figure 4.10: Considered system model comprising of a synchronous generator to obtain the NFP plot from linear analysis.

where H and $\omega_r = 2\pi f_r$ denote the inertia time-constant (in s) and rotor angular frequency (in rad/s) of the SG, respectively. P_m is the mechanical power input to the SG while P_d represents the damping power that can be expressed as

$$P_d = \frac{K_D}{\omega_N}(\omega_r - \omega_s), \tag{4.8}$$

where $\omega_s = 2\pi f_s$ represents the stator angular frequency (in rad/s) and K_D is the mechanical damping coefficient (in pu). Assuming a reactive transmission network and neglecting the impact of the excitation system, the active power output of the SG can be approximated as

$$P_g \approx \frac{E_{EMF} E_s}{X'_d + X_g} \sin\delta = P_{max} \sin\delta; \quad \delta = \frac{1}{s}(\omega_r - \omega_s), \tag{4.9}$$

where X'_d represents the transient reactance of the SG and δ denotes the load angle between the SG and the ideal-voltage source, which is constant in steady state. Assuming an ideal governor action, the mechanical power input to the SG is given by

$$P_m = P_{set} + \frac{D}{\omega_N}(\omega_N - \omega_r), \tag{4.10}$$

where P_{set} denotes the active power set-point of the SG and D represents the frequency-droop gain (in pu). The active power set-point of the SG is set to zero for the analysis made here. Taking the small-signal models of (4.7)-(4.10), the transfer function from the variation in the angular frequency of the grid

to the variation in the active power output of the SG can be obtained as

$$R_{\mathrm{SG}} = \frac{\Delta P_{\mathrm{g}}}{\Delta \omega_{\mathrm{s}}} = \frac{-P_{\max}(Ms + \frac{D}{\omega_{\mathrm{N}}})}{Ms^2 + \frac{K_{\mathrm{D}}+D}{\omega_{\mathrm{N}}}s + P_{\max}}. \tag{4.11}$$

The NFP plot can now be obtained from the Bode diagram of the transfer function, R_{SG}, which is shown with solid light-blue curves in Fig. 4.11 for an example SG of the same size ($S_{\mathrm{N}} = 112$ MVA) and inertia constant ($H = 5$ s) as that of the ES-STATCOM considered in the previous section. In the same figure, the NFP plot of a synchronous condenser[2] (SC) is shown with solid-blue curves for comparison. The transfer function for a SC, R_{SC}, is obtained by setting $D = 0$ in (4.11). Accordingly,

$$R_{\mathrm{SC}} = \frac{\Delta P_{\mathrm{g}}}{\Delta \omega_{\mathrm{s}}} = \frac{-P_{\max}(Ms)}{Ms^2 + \frac{K_{\mathrm{D}}}{\omega_{\mathrm{N}}}s + P_{\max}}. \tag{4.12}$$

Several key features of a device can be identified from the NFP plot. The first is the identification of a droop behaviour for the devices configured with a governor. The droop behaviour of an ideal SG is evident from Fig. 4.11 when the modulation frequency $f_{\mathrm{NFP}} \to 0$. This is characterized by a magnitude response equal to D and a 180° phase (due to the inverse relationship between active-power and grid-frequency variation) in the NFP plot. This can be easily understood by substituting $s = 0$ in (4.11). The droop behaviour of the devices is dominant in the lower frequency region (typically between 0 and 0.2 Hz) marked by the red color in Fig. 4.11. Due to the absence of a turbine (and hence the governor), droop behaviour is absent for the SC and the magnitude response decreases towards zero in the lower frequency region.

The second key feature is that the mid-range modulation frequencies marked by the yellow color in Fig. 4.11 allow the evaluation of the inertial response and damping provided by the device. The inertial response can be identified by using the inertia asymptote (shown with dashed-black curve in Fig. 4.11). The inertia asymptote, R_{H}, is obtained by ignoring the impact of the droop response, rotor resonance and damping, i.e., by ignoring the contribution of

[2] A synchronous condenser is a synchronous machine whose shaft is not connected to a turbine but spins freely.

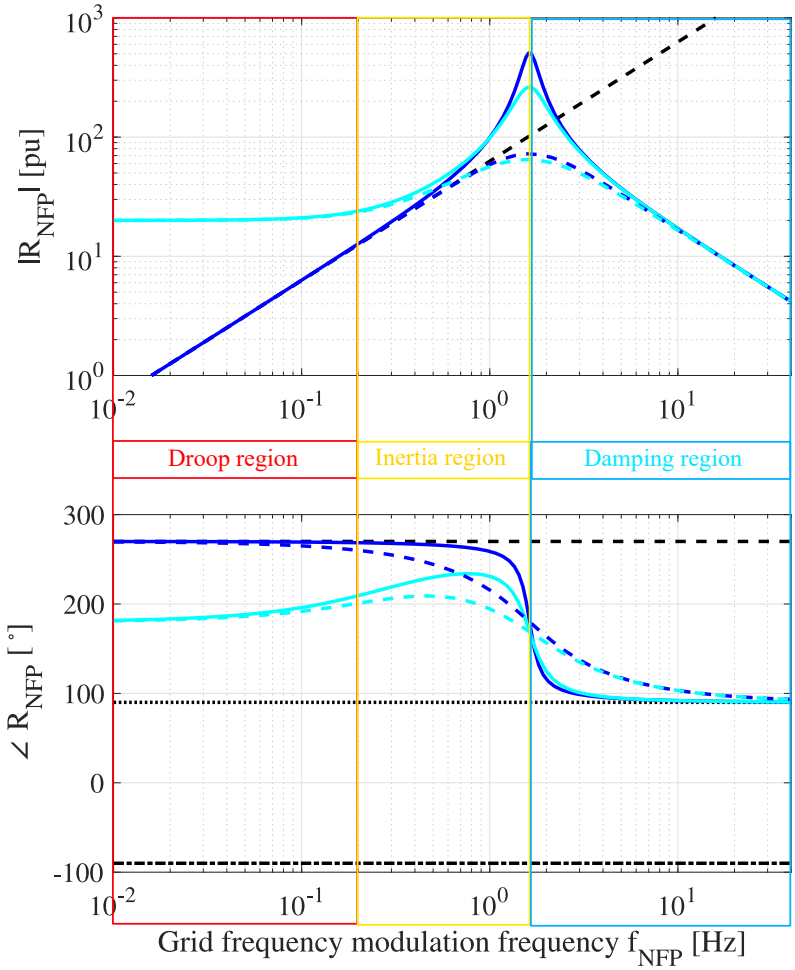

Figure 4.11: The NFP plot of an ideal SG (light-blue curves) and SC (blue curves). The dashed curves are obtained by increasing the value of damping coefficient by 7× of its initial value (solid curves).

the s^2 term in (4.12) and substituting $K_\mathrm{D} = 0$. Accordingly,

$$R_\mathrm{H} = \frac{\Delta P_\mathrm{g}}{\Delta \omega_\mathrm{s}} = -Ms. \tag{4.13}$$

It can be observed from Fig. 4.11 and (4.13) that the inertia asymptote has a 270° phase and a magnitude response that increases linearly with an increase in the modulation frequency. The NFP plot of any device that claims to provide a true inertial response should approach the inertia asymptote both in terms of magnitude and phase, over a range of modulation frequencies (typically between 0.2 and 2.0 Hz) at which the rotor inertial response is dominant over the droop and damping responses. As seen from Fig. 4.11, both the SG and SC follow the inertia asymptote in this frequency region as expected. Similar to the case of a SG, any device which provides both droop and inertial responses, there must be a noticeable shift from the 180° phase of the droop response to a more advanced phase towards 270° for demonstrating dominance of an inertial response over the relevant range of modulation frequencies.

The third key feature is that for any device that intercepts the inertia asymptote, R_H, there must be a resonance that occurs at the characteristic frequency of the second-order response in (4.11) or (4.12). The typical frequency region of this resonance is between 1 and 3 Hz, depending upon the inertia time-constant, damping coefficient and the total reactance between the DUT and the ideal-voltage source, as observed for both SG and SC in Fig. 4.11. The high resonance peak in the magnitude response is resulting from a low value of the damping coefficient, K_D, which typically is the case in a real SG or SC. On the contrary, this parameter can be selected freely in converter systems emulating an inertial response. The impact of increasing K_D to seven times of its original value is shown in Fig. 4.11 by the dashed light-blue and the dashed-blue curves for the case of an ideal SG and SC, respectively. It can be observed from the figure that the damping coefficient influences the response in both inertia and damping region[3] (marked by the blue color in Fig. 4.11). Increasing K_D significantly reduces the resonance peak in the magnitude response. Furthermore, a better contribution towards system damping with increasing K_D is evident from the movement of the phase plot close to 180° for both SG and SC in the inertia and damping region. This behavior can

[3]In this region, damping provision from the synchronous machine is dominant over the droop and inertial responses

be explained from the small-signal model of (4.8); where, the damping power component is characterized by the component of the active-power variation in anti-phase with the variation in the angular frequency of the grid.

The fourth and the final key feature that can be identified from the NFP plot of a device in the damping region (typically above 1.5 Hz) is the response of the device to fast changes in the grid frequency or phase-angle jumps. As observed from Fig. 4.11, the response in this region is characterized by a continuous decrease of the amplitude response with an increase in the modulation frequency. Furthermore, for an ideal SG and SC, the phase starts to decline below 180° and levels off at 90° as the modulation frequency approaches the fundamental grid frequency. This implies a reduction in the damping power component of the device and a positive synchronizing power component. From the small-signal model of (4.9), the synchronizing power component is characterized by the component of the active-power variation in phase with the variation in the load angle (which is equivalent to a phase advance of 90° with respect to variation in the grid frequency). It is particularly important for a device claiming GFM behaviour to follow the distinctive amplitude and phase trajectories of synchronous machines (SG or SC) in the damping region, which is characterized by a positive synchronizing power component.

As from the analyses above, the NFP plot can be used as a tool to identify the characteristic behaviour of a GFM converter system and thereby distinguish it from a GFL one. This is exemplified in Fig. 4.12, where the NFP plots of an individual converter system with the GFM control strategy (as in Fig. 3.11) and the conventional GFL control (as in Fig. 4.3) are shown with green and red colors, respectively. For comparison, the NFP plot of the SC from the previous example is shown in the same figure. The ratings of the converter for both cases are kept the same as that of the SC and for a fair comparison, the active power set-point of the converter is set to zero. Since the magnitude response of the GFL converter is very small as compared to that of the SC and GFM converter, it is not displayed in this figure.

It can be observed from the red curve in Fig. 4.12 that for the GFL converter, the phase continues to decrease in the damping region and does not level off with an increase in the modulation frequency as in the case of a SC (blue curves). Moreover, beginning around 10 Hz, the phase becomes negative (the sudden change in the phase plot is the wrapped phase which is displayed in the range of 0 to 360°), meaning that both damping and synchronizing power

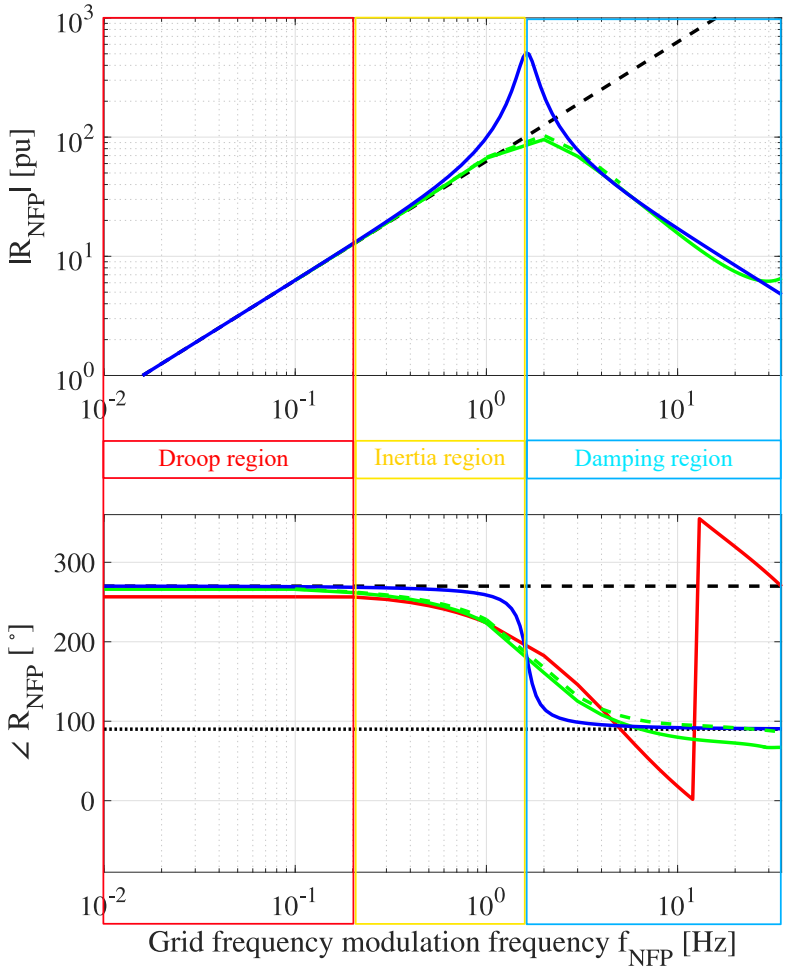

Figure 4.12: The NFP plot of an ideal SC (blue curves), a GFL converter (red curve) and a GFM converter with its virtual impedance made 0.5× (dashed-green curves) of its original value (solid-green curves).

components become negative in this region. This indicates a risk of instability if an oscillation is triggered in this frequency region. The risk for instability increases when the connecting grid becomes weak. This can be understood from the NFP plot of the GFL converter in a weak grid shown in Fig. 4.13, where an increase in the magnitude response can be observed in the frequency region where the phase response is negative.

On the other hand, the NFP plot of the GFM converter (solid-green curves in Fig. 4.12) is similar to that of a SC in all the three regions. A higher damping provision from the GFM converter as compared to the SC is evident from a reduced resonance peak in the magnitude response, as well as from the movement of the phase plot closer to 180° in both inertia and damping regions. Furthermore, in contrary to the converter system with GFL control, the GFM converter does not exhibit phase wrapping, meaning that the synchronizing power component remains positive throughout the upper-frequency region. However, it can be observed from the figure that in contrast to the phase response of an ideal SC, in case of the GFM converter, the phase plot goes below 90°, implying a negative damping power component at high modulation frequencies. This behaviour is mainly due to the choice made earlier to select a high value for the virtual impedance, and is similar to the special case reported in [119], [120], where the excitation system of a SG with high armature resistance and transient reactance introduces a negative damping torque component when operating at light load conditions. If desired, by reducing the value of virtual impedance, the phase response of the GFM converter at high modulation frequencies can be made similar to an ideal SC as shown by the dashed green-curves in Fig. 4.12. However, this is a compromise between the benefits of a large virtual impedance mentioned earlier and the resulting negative damping power component at high modulation frequencies.

4.5.2 NFP plot of the offshore wind power plant

In this section, the NFP plot is used to evaluate the GFM behaviour of the considered WPP shown in Fig. 4.1. For this, frequency perturbation is applied at the onshore terminal 'T1' (see Fig. 4.1), while the wind farm is operated at half of its rated power. For the ease of comparison with the previous case study and a better visual representation, the measured output active-power variation at the terminal 'T1' is normalized with respect to the rated power of the ES-STATCOM, which is 112 MVA. Figure 4.14 shows the NFP plot of the

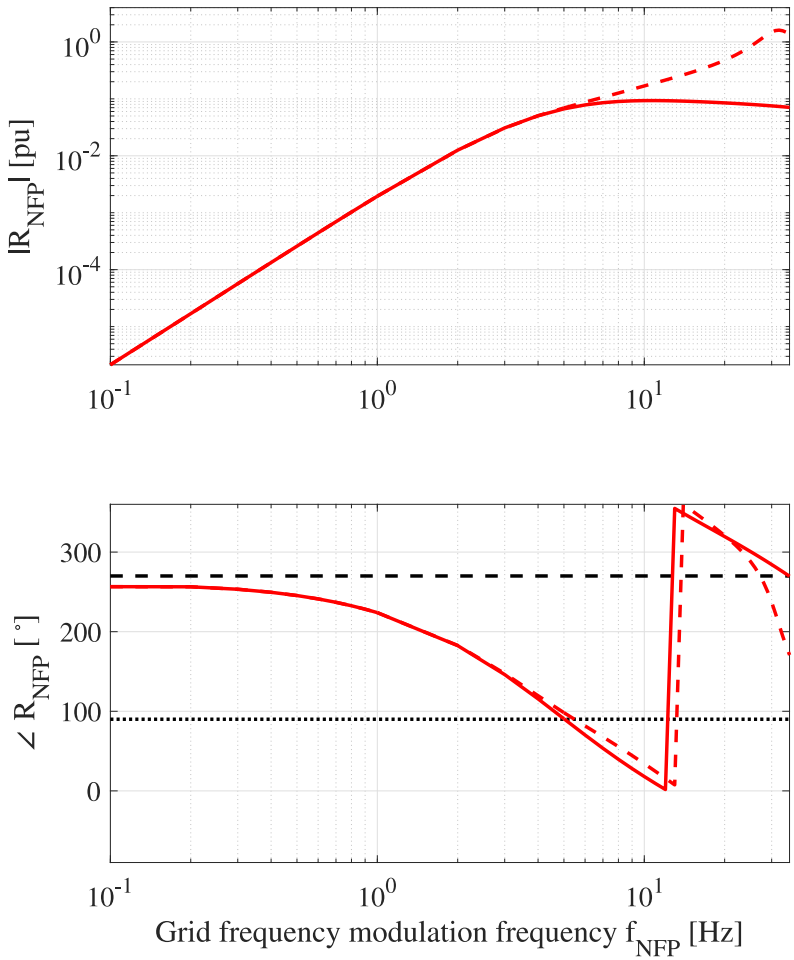

Figure 4.13: The NFP plot of a GFL converter in a strong grid (solid-red curves) and weak grid (dashed-red curves).

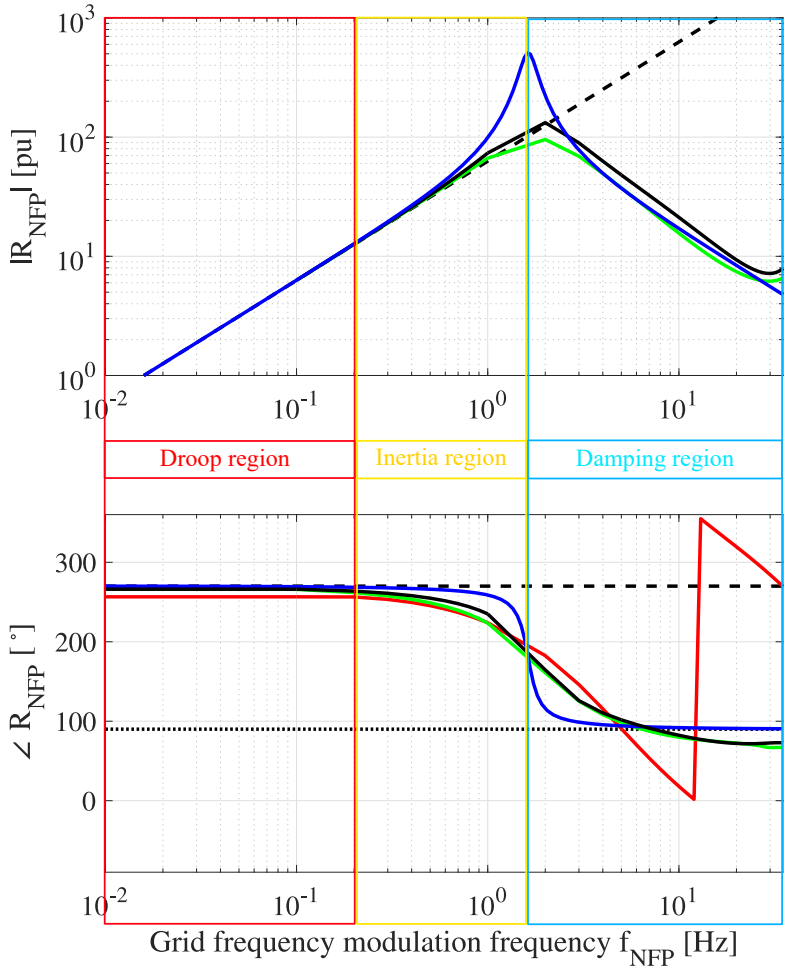

Figure 4.14: The NFP plot of an ideal SC (blue curves), a GFL converter (red curve), a GFM converter (green curves) and the considered WPP (black curves).

WPP with solid-black curves. The NFP plot of an ideal SC (blue curves), the GFL (red curve) and GFM converters (green curves) from the previous case study are also shown in the same figure for comparison. It can be observed from the figure that the NFP plot of the WPP closely follows the magnitude and phase response of GFM converter in all the three regions, confirming the GFM behaviour of the considered WPP. Furthermore, emulation of the desired amount of inertia from the WPP is also confirmed from its magnitude response in the droop and inertia regions, which closely follows the inertia asymptote (dashed-black curves).

The impact of the WPP's operating point on its GFM behaviour is investigated next. It can be observed from Fig. 4.15 that operating point of the WPP has no major impact on the GFM behaviour of the WPP. Nevertheless, reducing the operating point slightly reduces the damping provision from the WPP at high modulation frequencies. This behaviour agrees well with the explanation made earlier for the GFM converter/SG operated under light load conditions. Finally, the impact of reducing the size of the ES-STATCOM on the GFM behaviour of the WPP is shown in Fig. 4.16. It can be observed from the figure that with a reduction in the size of the ES-STATCOM, the phase plot of the WPP (black curves) advances towards the phase plot of the GFL converter (red curve) in the upper-frequency region. As expected, this indicates a reduction in the GFM behaviour of the WPP. Furthermore, a decrease in the inertia contribution of the WPP is evident from the movement of the magnitude response downwards with a reduction in the size of the ES-STATCOM.

4.6 Summary

In this chapter, the dynamic performance of a realistic WPP has been shown for various grid disturbances. It has been shown that adopting the proposed GFM control strategy for the ES-STATCOM aids the operation of the WPP during weak grid conditions and provides the GFM capability to the WPP. Furthermore, the concept of NFP has been introduced and the interpretation of the NFP plot has been presented in detail. Finally, using the NFP plot, the GFM behaviour of the considered WPP has been validated.

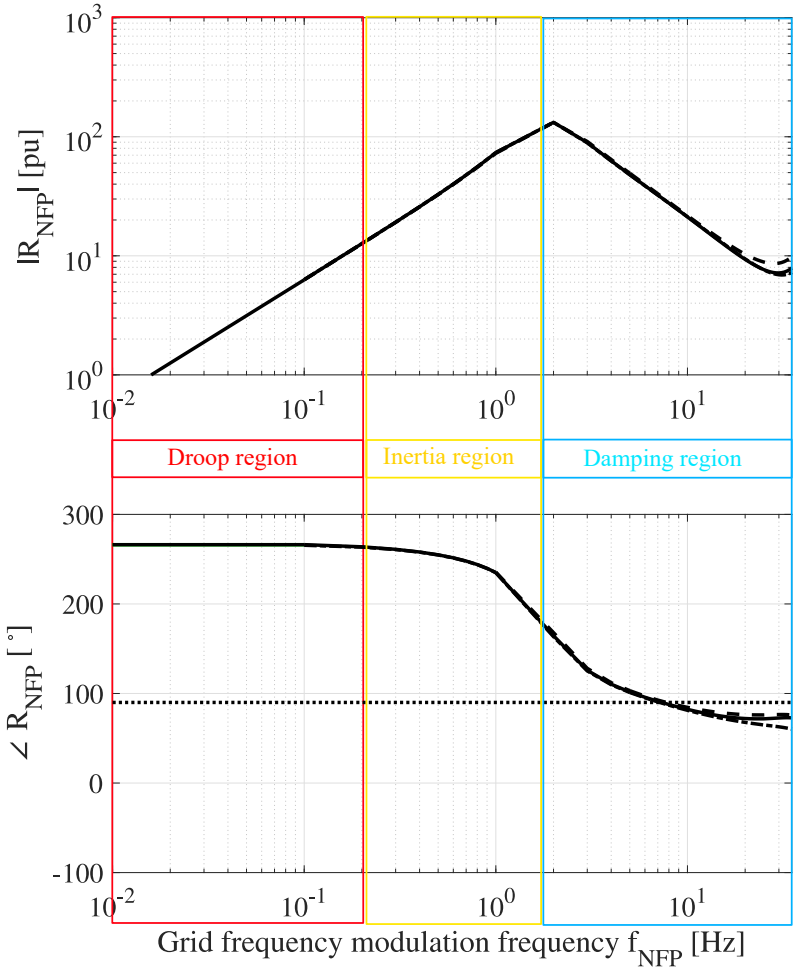

Figure 4.15: The NFP plot of the considered WPP operating at 0.9 pu (dashed-black curves), 0.5 pu (solid-black curves) and 0.2 pu (dashed-dotted black curves).

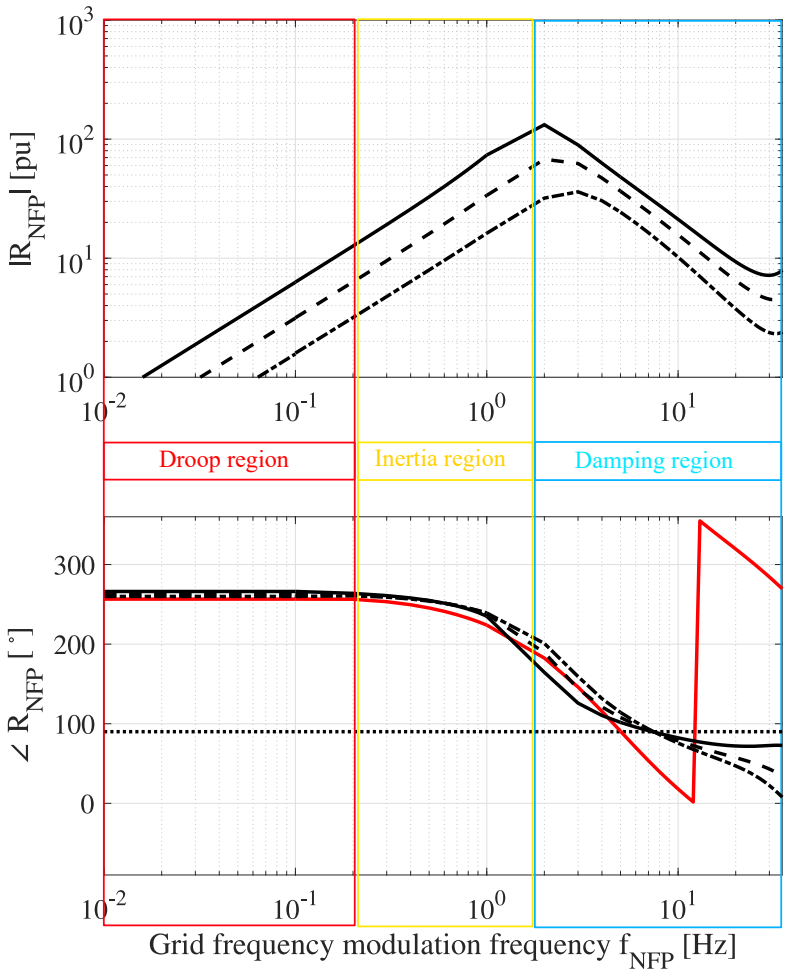

Figure 4.16: The NFP plot of a converter system with the classical GFL control (red curve) and the considered WPP with size of the ES-STATCOM reduced by 50% (dashed-black curves) and 75% (dashed-dotted black curves) as compared to its original value (solid-black curves).

CHAPTER 5

Energy-storage system for wind power applications

5.1 Introduction

In the previous chapter, the role of the ES-STATCOM in providing the GFM capabilities to a WPP has been investigated. This includes the ability of the WPP to provide ancillary services such as active-power support to damp low-frequency oscillations as well as in case of frequency disturbances and phase-angle jumps in the grid. This chapter presents an overview of various energy storage technologies (ESTs) suitable for the ES-STATCOM for this purpose. Differences in the power and energy densities of the considered ESTs are briefly discussed to identify what type of energy storage is feasible for a specific ancillary service. With focus on the two most suitable ESTs, i.e., batteries and supercapacitors, recommendations are given for design and sizing of the energy storage system (ESS) for a given application. In addition, the equivalent models of battery energy storage system (BESS) and supercapacitor-based energy storage system (SCESS) suitable for power systems dynamic's studies are presented and discussed. Finally, an alternative control strategy for the GFM converters with SCESS is presented, which allows a provision of synthetic inertia from the converter system without compromising the speed of

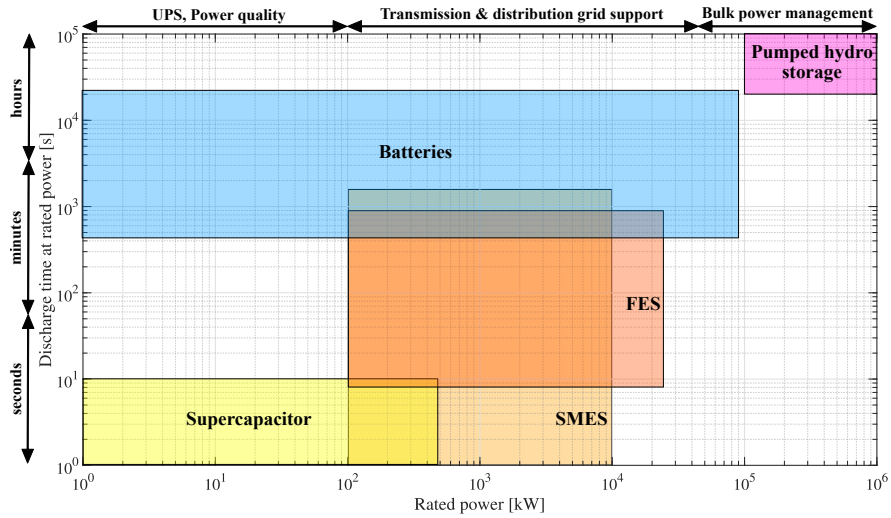

Figure 5.1: Comparison of discharge time and power ratings of different ESTs for various ancillary services in power systems [121], [122].

response of the dc-voltage controller.

5.2 Energy storage technologies for ancillary services

Ancillary services refer to functions and services that help system operators to maintain a stable and reliable operation of the power grid by maintaining a continuous power flow, addressing imbalances between supply and demand, and helping the system recover after a disturbance. To asses what type of EST is best suited for a given ancillary service, it is necessary to familiarize with the characteristics of individual storage technologies. Figure 5.1 shows the classification of various ESTs based on their rated power output and discharge time [121], [122]. It can be inferred from the data presented in Fig. 5.1 that supercapacitor, super conducting magnetic energy storage (SMES), flywheel energy storage (FES) and batteries provide the most suitable match in terms of the required power and energy levels for the services related to the grid support (at both transmission and distribution levels) and hence the GFM

Table 5.1: Storage characteristics of the most suitable ESTs.

Parameters	Supercap	SMES	FES	Batteries
Specific energy (Wh/kg)	2.5-15	0.5-75	5-100	75-200
Specific power (W/kg)	500-10000	500-2000	400-1500	150-2000
Cyclic efficiency (%)	85-97	95-98	90-95	90-97
Self discharge (%/day)	5-40	10-15	100	0.1-0.3
Discharge time	ms-s	ms-min	s-min	min-h

capabilities of a converter system.

Apart from power and energy levels, there are other parameters such as specific power, specific energy and efficiency that must also be considered to assess the suitability of an EST for a given ancillary service. Based on the data available in [122], Table 5.1 presents a comparison[1] of some of these parameters for different ESTs. Specific power relates to the EST's ability to provide instantaneous power. A higher specific power indicates that the EST can discharge a large amount of power on demand. On the other hand, specific energy reflects the ability of the EST to provide continuous energy over a period of time. A high specific energy indicates that the EST can discharge energy for long periods. Ideally, it is desirable that an EST features both high specific power and energy. However, as it can be observed from Table. 5.1, ESTs with highest specific power tend to have lower specific energy; i.e, they can discharge large amounts of power, but only for a short time. Likewise, ESTs with highest specific energy tend to have lower specific power; i.e., they can discharge energy for a long time, but cannot provide massive amounts of power immediately. Accordingly, for ancillary services that require high power for short time, such as provision of synthetic inertia support or Fast Frequency Reserve[2] (FFR), supercapacitors are the preferred choice owing to their highest specific power.

On the other hand, for black start and applications related to frequency regulation in larger time frames, such as Frequency Containment Reserve (FCR) or Frequency Restoration Reserve (FRR), batteries are the preferred choice

[1]Note that the values presented in the table are of general nature and can vary depending upon the maturity of the technology.

[2]FFR provision in the Nordic Synchronous Area requires a full response to be delivered within 1 s and maintained for a minimum duration of 5 s.

Table 5.2: Comparison of power and energy densities of various battery technologies [121].

Battery technology	Specific energy (Wh/kg)	Specific power (W/kg)
Li-ion	90-260	150-2000
Lead-acid	30-50	75-300
Nickel-metal hydride	60-120	∼1000
Nickel-cadmium	45-80	150-300
Sodium-sulfur	100-240	150-230
Flow batteries	10-30	170

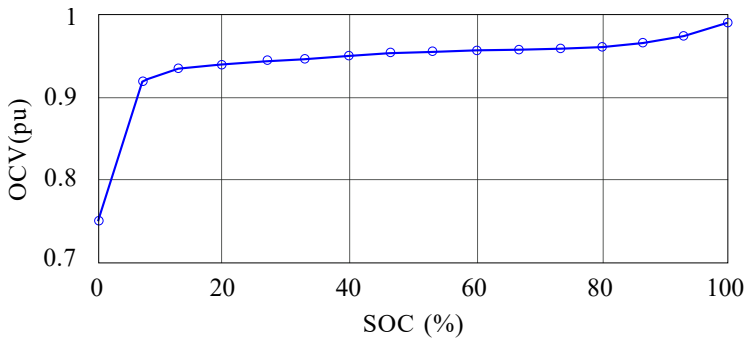

Figure 5.2: Typical OCV versus SOC relationship for Li-ion batteries [123].

owing to their highest specific energy and low self-discharge rate. Furthermore, for selecting the most suitable battery technology among the various alternatives, a comparison of different battery technologies is made based on their specific power and energy as illustrated in Table 5.2. It can be inferred from Table 5.2 that owing to their high specific power and specific energy, Li-ion batteries present a superior behaviour over other battery technologies. Moreover, the open circuit voltage (OCV) versus state of charge (SOC) relationship for Li-ion batteries is quite flat, with around 5% OCV variation between 10% and 90% battery SOC (see Fig. 5.2). This offers a significant advantage over other technologies with regard to less variations in the dc-link voltage of the converter system. Hence, Li-ion batteries are considered for BESS in this chapter.

The basic structure of a BESS or SCESS typically consists of a battery or supercapacitor bank linked to a VSC. The topology of the VSC plays

an important role in designing of an ESS. Typically, the STATCOMs used in WPPs are based on modular multilevel converters (MMCs) [98]. In this context, an ESS can be integrated with the STATCOM by either distributing the energy storage units in the converter's submodules, or alternatively placing a centralized energy storage (CES) at the dc-link of the converter. Among the two alternatives, it is found in [124] that a CES is the most feasible solution for the ES-STATCOM, as it offers design flexibility, low storage volume and small silicon area. Accordingly, double star bridge cell-centralized energy storage (DSBC-CES) topology is considered here for the realization of ES-STATCOM as shown in Fig. 5.3. The double star topology of the MMC presents dc-link terminals necessary for the connection of CES. Furthermore, the full-bridge cells allow a varying pole-to-pole dc-link voltage as they can generate both positive and negative voltages. Consequently, the operation of the converter does not depend upon a minimum dc-link voltage [125], which means that the ESS can be designed for a lower voltage rating.

5.3 Design and modelling of BESS

The design and modelling of a BESS for ES-STATCOM is presented in this section. As shown in Fig. 5.3, a BESS typically consists of several battery modules connected in series to form a battery string, and parallel connection of several battery strings to form the overall battery bank. The number of battery modules connected in series and parallel-connected battery strings depends upon the dc-link voltage, active power and energy requirements of the converter, as well as on the storage capacity, maximum C-rate[3], minimum/maximum allowed voltages, and minimum/maximum allowed state-of-charge (SOC) levels of each battery module as described below.

5.3.1 Design of BESS

The design methodology presented in this section neglects power losses in the BESS for simplicity, and assumes the same C-rate during the charging and discharging process of the battery. The first step is to determine the voltage

[3]C-rate is a measure of the rate at which a battery is charged/discharged relative to its maximum capacity. For example, if the capacity of a battery is 100 Ah and the C-rate is 0.5, it means that the battery can be charged/discharged with a maximum current of 50 A.

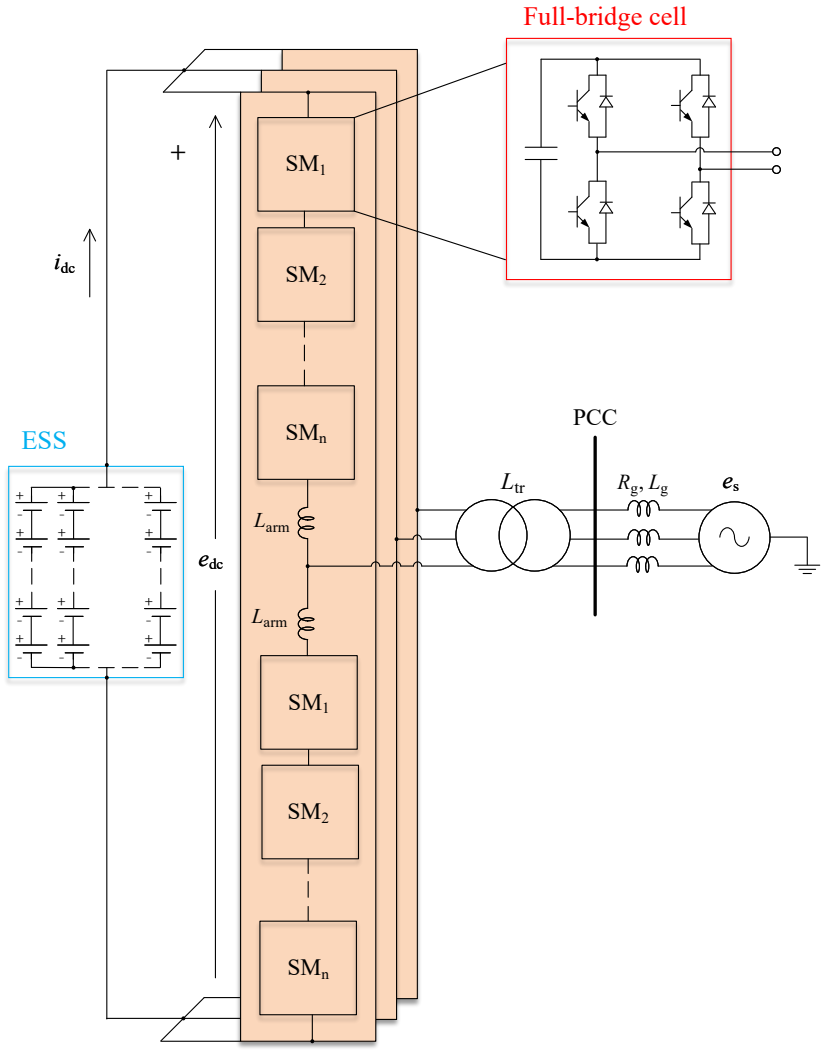

Figure 5.3: Schematic of Double-star bridge cell MMC with centralized energy storage (DSBC-CES).

rating of the battery bank. Following the recommendations in [123], [124] this can be calculated based on the required dc-link voltage, E_{dc}, and considering sinusoidal modulation as

$$E_{\mathrm{dc}} = \frac{2\sqrt{2}}{k_{\mathrm{om}}\sqrt{3}} 1.05 E_{\mathrm{g}}(1 + \Delta E_{\mathrm{g}} + X_{\mathrm{eq}}), \tag{5.1}$$

where E_{g} denotes the RMS line to line grid voltage, ΔE_{g} is the maximum assumed grid-voltage variations in pu, and k_{om} is the over-modulation index. X_{eq} represents the equivalent reactance between the converter and PCC in pu. In (5.1), a 5% margin is considered to guarantee a proper dynamic performance of the current controller [98], and a rated output reactive current (1.0 pu) from the converter to the grid is assumed.

Thanks to the bridge cells in DSBC-CES topology, the output voltage is not limited by the dc-link voltage and the converter can handle dc-link voltage variations. Accordingly, the number of series-connected battery modules, $N_{\mathrm{s,b}}$, can be computed as

$$N_{\mathrm{s,b}} = \mathrm{ceil}\left(\frac{E_{\mathrm{dc}}}{E_{\mathrm{b,max}}}\right), \tag{5.2}$$

where $E_{\mathrm{b,max}}$ is the maximum voltage of a battery module.

The total number of parallel-connected battery strings is based on two criteria that the BESS must fulfill [123], [124]. The first criterion is that the battery bank must have a capacity to fulfill the active-power requirement, P_{n}. Accordingly,

$$N_{\mathrm{p1}} = \mathrm{ceil}\left(\frac{P_{\mathrm{n}}}{P_{\mathrm{str,min}}}\right), \tag{5.3}$$

where $P_{\mathrm{str,min}}$ is the minimum power that can be provided by a battery string which is given as

$$P_{\mathrm{str,min}} = N_{\mathrm{s,b}} E_{\mathrm{b,min}} C_{\mathrm{r}} C_{\mathrm{b}}. \tag{5.4}$$

In (5.4), $E_{\mathrm{b,min}}$, C_{r} and C_{b} denote the minimum voltage, maximum recommended C-rate and capacity of a battery module, respectively. The second criterion is that the battery bank must fulfill energy requirement, W_{n}, of the

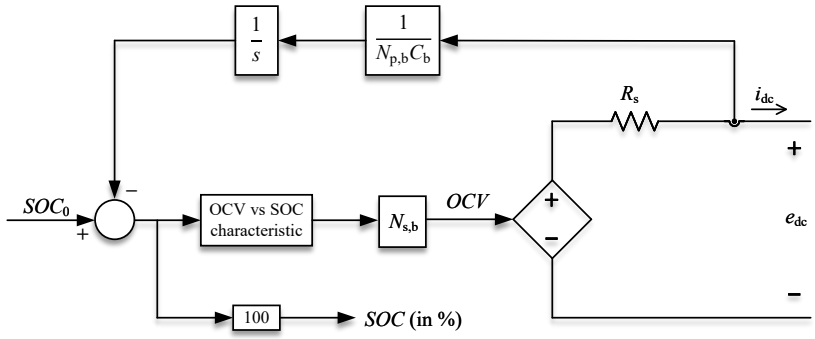

Figure 5.4: Electrical equivalent model of the battery bank.

application. Accordingly,

$$N_{\mathrm{p2}} = \mathrm{ceil}\left(\frac{W_{\mathrm{n}}}{N_{\mathrm{s,b}} E_{\mathrm{b,N}} C_{\mathrm{b}} (SOC_{\max} - SOC_{\min})}\right), \tag{5.5}$$

where $E_{\mathrm{b,N}}$ denotes the rated voltage of a battery module, and $SOC_{\max}$, $SOC_{\min}$ are the maximum and minimum allowed SOC of a battery module (in pu), respectively. Finally, the number of parallel-connected battery strings, $N_{\mathrm{p,b}}$, is given by

$$N_{\mathrm{p,b}} = \max\left(N_{\mathrm{p1}}, N_{\mathrm{p2}}\right). \tag{5.6}$$

5.3.2 Modelling of BESS

Figure. 5.4 shows the electrical equivalent model of the battery bank suitable for dynamic studies in power systems [123]. It consists of an ideal-voltage source in series with a constant equivalent internal resistance, R_{s}. The ideal-voltage source is used to represent the OCV of the battery bank. The OCV versus SOC characteristic is included through a look-up table. The series resistance accounts for the voltage drop or rise at the terminals of the battery bank, when the bank is discharged or charged. It also accounts for the power losses in the battery bank. This resistance is the so-called equivalent series resistance (ESR), which is typically measured through empirical tests.

Despite of its simplicity, this aggregated model computes the battery bank's current and voltage. An interesting feature of this model is that its complexity

does not depend on $N_{s,b}$ and $N_{p,b}$. The model also provides an estimation of the equivalent SOC of the battery bank. The SOC approximation is given by

$$SOC = SOC_0 - \int_0^t \frac{i_{\mathrm{dc}}}{N_{\mathrm{p,b}} C_{\mathrm{b}}} dt \tag{5.7}$$

i_{dc} is the instantaneous current flowing through the battery bank.

5.4 Design and modelling of SCESS

In the recent years, supercapacitors or ultracapacitors have attracted considerable attention thanks to their high power density, high charge/discharge rates, and long life cycle performance [126]–[128]. The main difference between the conventional electrolytic capacitor and a supercapacitor is that in the conventional electrolytic capacitor, the electrodes are separated by a solid dielectric material, while a supercapacitor uses a separator [129], [130]. Basically, the separator is an ion permeable membrane that can provide insulation and exchange of ions of electrolyte between the electrodes. Electrochemical double layer capacitors (EDLCs) are the most commonly used supercapacitors in applications demanding high peak power for short duration [131]. Owing to the presence of electric double layer, the EDLC exhibits significantly higher capacitance rating (in the range of kF) as compared to the conventional electrolytic capacitor (in the range of mF/μF) [129], [132].

5.4.1 Design of SCESS

Similar to the case of BESS, the first step here is to determine the voltage rating of the supercapacitor bank. For this, the operating dc-link voltage, E_{dc0}, or the nominal voltage of the bank is calculated as in (5.1). However, unlike Li-ion batteries, which present a relatively flat voltage profile with varying SOC, the energy stored in a supercapacitor is proportional to the square of the voltage across it (like any other capacitor). This implies that if an ES-STATCOM with SCESS provides active-power support to the system, the voltage at the dc link of the ES-STATCOM will vary quite significantly. This will result in an increase or decrease of the current on the dc side and ultimately the arm currents of the converter. The peak value of the arm

current, $\hat{I}_{\mathrm{arm}}$, in the DSBC-CES topology is given as [125]

$$\hat{I}_{\mathrm{arm}} = \frac{\hat{I}_{\mathrm{g}}}{2} + \frac{P_{\mathrm{n}}}{3E_{\mathrm{dc}}}, \tag{5.8}$$

where $\hat{I}_{\mathrm{g}}$ denotes the peak value of the output converter current. During the discharging phase of the SCESS, the voltage at the dc link of the converter, E_{dc}, reduces for the given active-power requirement, P_{n}, resulting in a substantial increase of the arm current. Hence, the SCESS should be designed in such a way that for a given active-power requirement, the arm current does not exceed its maximum permissible value, I_{max} (maximum allowed current through the semiconductor devices in each submodule of the converter). Accordingly, the minimum dc-link voltage, $E_{\mathrm{dc,min}}$, can be calculated using (5.8) as

$$E_{\mathrm{dc,min}} = \frac{2}{3}\frac{P_{\mathrm{n}}}{2I_{\mathrm{max}} - \hat{I}_{\mathrm{g}}}. \tag{5.9}$$

Hence, the energy available from the supercapacitor bank during its discharge phase, $W_{\mathrm{discharge}}$, is given by

$$W_{\mathrm{discharge}} = \frac{1}{2}C_{\mathrm{eq}}(E_{\mathrm{dc0}}^2 - E_{\mathrm{dc,min}}^2), \tag{5.10}$$

where C_{eq} is the equivalent capacitance of the supercapacitor bank. Similarly, to allow an active-power flow into the supercapacitor bank, an energy buffer should be allocated for the charging phase, W_{charge}. If the energy buffer in the supercapacitor bank is kept the same for its charging and discharging phases, i.e., $W_{\mathrm{discharge}} = W_{\mathrm{charge}}$, the maximum dc-link voltage, $E_{\mathrm{dc,max}}$, can be calculated as

$$E_{\mathrm{dc,max}} = \sqrt{2E_{\mathrm{dc0}}^2 - E_{\mathrm{dc,min}}^2}. \tag{5.11}$$

The supercapacitor bank should be designed to withstand this maximum voltage. Accordingly, the number of series-connected supercapacitor modules, $N_{\mathrm{s,c}}$, can be computed as

$$N_{\mathrm{s,c}} = \mathrm{ceil}\left(\frac{E_{\mathrm{dc,max}}}{E_{\mathrm{c,N}}}\right), \tag{5.12}$$

where $E_{\mathrm{c,N}}$ denotes the rated voltage of a supercapacitor module.

Similar to the case of BESS, the total number of parallel-connected supercapacitor strings is based on two criteria that the SCESS must fulfill. The first criterion is that the supercapacitor bank must be able to fulfill the active-power requirement. Accordingly,

$$N_{\mathrm{pc1}} = \mathrm{ceil}\left(\frac{P_{\mathrm{n}}}{E_{\mathrm{dc,min}} I_{\mathrm{c}}}\right), \tag{5.13}$$

where I_{c} is the current rating of a supercapacitor module. The second criterion is that the supercapacitor bank must fulfill the energy requirements. Accordingly,

$$N_{\mathrm{pc2}} = \mathrm{ceil}\left(\frac{N_{\mathrm{s,c}} C_{\mathrm{eq}}}{C}\right), \tag{5.14}$$

where C_{eq} and C denote the equivalent capacitance of the bank and the capacitance of a supercapacitor module, respectively. Finally, the number of parallel-connected supercapacitor strings, $N_{\mathrm{p,c}}$, is given by

$$N_{\mathrm{p,c}} = \max\left(N_{\mathrm{pc1}}, N_{\mathrm{pc2}}\right). \tag{5.15}$$

The term C_{eq} can be calculated based on the energy requirements of the application. For instance, if the intended use of the supercapacitor bank is for synthetic inertia support, C_{eq} can be obtained by equating the energy requirements during a RoCoF event for the worst-case scenario and the maximum energy that can be provided/absorbed by the SCESS, i.e.,

$$\frac{1}{2} C_{\mathrm{eq}} (E_{\mathrm{dc0}}^2 - E_{\mathrm{dc,min}}^2) = \frac{2 H S_{\mathrm{N}} \Delta\omega_{\mathrm{max}}}{\omega_{\mathrm{N}}} = \frac{1}{2} C_{\mathrm{eq}} (E_{\mathrm{dc,max}}^2 - E_{\mathrm{dc0}}^2), \tag{5.16}$$

where S_{N} denotes the rated power of the converter, ω_{N} is the rated angular frequency of the system, H is the inertia time-constant to be emulated from the converter, and $\Delta\omega_{\mathrm{max}}$ is the maximum deviation in the angular frequency of the system from its rated value. Accordingly,

$$C_{\mathrm{eq}} = \frac{4 H S_{\mathrm{N}} \Delta\omega_{\mathrm{max}}}{\omega_{\mathrm{N}} (E_{\mathrm{dc0}}^2 - E_{\mathrm{dc,min}}^2)} = \frac{4 H S_{\mathrm{N}} \Delta\omega_{\mathrm{max}}}{\omega_{\mathrm{N}} (E_{\mathrm{dc,max}}^2 - E_{\mathrm{dc0}}^2)}. \tag{5.17}$$

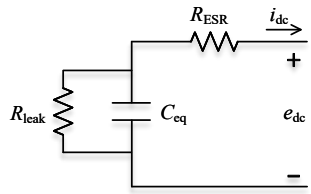

Figure 5.5: Electrical equivalent model of supercapacitor bank.

5.4.2 Modelling of SCESS

Figure 5.5 shows the electrical equivalent model of the supercapacitor bank suitable for dynamics studies in a power system [133], [134]. It consists of three main elements: the equivalent capacitance of the bank, equivalent series resistance, R_{ESR}, and equivalent leakage resistance, R_{leak}. The equivalent series resistance is an equivalent of the electrical resistance of the electrodes and the ionic resistance of the electrolyte; whereas, the equivalent leakage resistance represents the total leakage in the supercapacitor bank that takes place through different leakage mechanisms [135]. To maintain the supercapacitor-bank voltage at its nominal value, a small leakage current must continuously flow into the bank.

5.5 Control of SCESS-based grid-forming converters

As mentioned in the previous section, if a GFM converter with SCESS is providing temporary active-power support, the voltage at its dc link will vary quite significantly. Hence, it is of importance to effectively regulate the dc-link voltage, especially during the support period. Typically, in a GFM control strategy, the dc-link voltage controller is added as an outer loop in cascade to the active-power controller [30] as shown in Fig. 5.6. In converter systems emulating inertia, the dc-link voltage controller should be kept slow as compared to the active-power controller so that the desired inertial response is delivered. This is due to the fact that the two controllers have counteractive actions. For instance, consider a case of negative RoCoF in the grid. In this case, the GFM converter system will increase its active-power output to resist to changes in

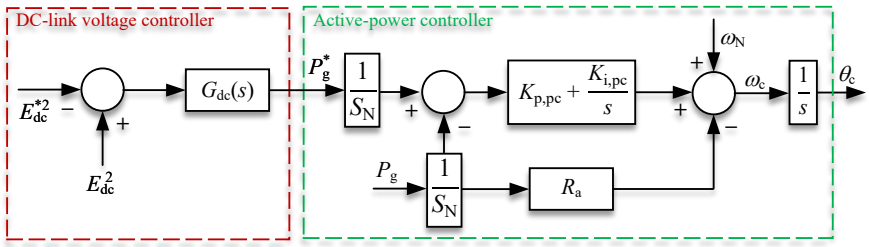

Figure 5.6: Classical cascaded structure of the dc-link voltage and active-power controllers.

the grid frequency. This will result in a discharge of the supercapacitor bank and correspondingly a decrease in the dc-link voltage of the converter system. At the same time, the dc-link voltage controller will try to keep the dc-link voltage at its nominal value by decreasing the active-power reference. Hence, if both controllers have a similar speed of response, inertia support cannot be delivered. Furthermore, being the two controllers in cascade, similar loop bandwidths might lead to control instability.

In this section, an alternative approach to regulate the dc-link voltage of the GFM converters integrated with SCESS is presented, which allows the provision of virtual inertia without the need to slow down the speed of response of the dc-link voltage controller.

5.5.1 Alternative structure for the dc-link voltage controller

Figure 5.7 shows the block scheme of the alternative structure for the dc-link voltage controller. As shown in the figure, the time integral of the inertial power obtained from the IEL presented in Chapter 3 is used to estimate the required energy variation, ΔW_{sc}, in the supercapacitor bank to provide the desired inertial response from the converter system during a frequency excursion in the grid. The required energy variation along with the energy stored in the supercapacitor bank at the operating dc-link voltage, W_{sc0}, and the equivalent capacitance of the bank are used to calculate the reference value for the dc-link voltage controller, $E_{dc}^{\star 2}$, as

$$E_{dc}^{\star 2} = \frac{2(W_{sc0} - \Delta W_{sc})}{C_{eq}}. \tag{5.18}$$

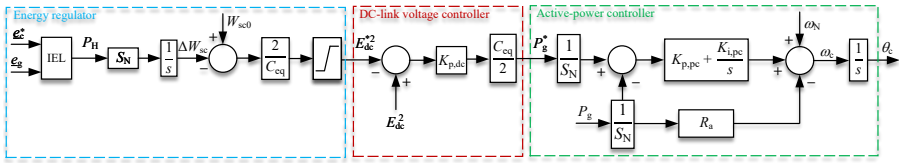

Figure 5.7: Block scheme of the alternative structure for the dc-link voltage controller.

As shown in Fig. 5.7, a hard limiter is used to keep the reference value between $E^2_{\mathrm{dc,min}}$ and $E^2_{\mathrm{dc,max}}$.

Finally, a proportional controller is used to drive the square of the dc-link voltage, E^2_{dc}, to its reference value, $E^{\star 2}_{\mathrm{dc}}$, and calculate the reference power, $P^\star_{\mathrm{g}}$, for the APL as

$$P^\star_{\mathrm{g}} = \frac{C_{\mathrm{eq}}}{2S_{\mathrm{N}}} K_{\mathrm{p,dc}}[E^2_{\mathrm{dc}} - E^{\star 2}_{\mathrm{dc}}], \tag{5.19}$$

where $K_{\mathrm{p,dc}}$ denotes the gain of the proportional controller. Having the dimension angular frequency, $K_{\mathrm{p,dc}}$ can be considered as the ideal dc-link control-loop bandwidth. Thanks to the proposed control structure, the dc-link voltage control loop can be as fast as the APL. Accordingly, the proportional gain of the dc-link voltage controller can be selected as

$$K_{\mathrm{p,dc}} = \alpha_{\mathrm{pc}}. \tag{5.20}$$

5.5.2 Simulation verification

In order to validate the effectiveness of the proposed control structure, a detailed simulation model of the grid-connected converter system shown in Fig. 5.8 is implemented in PSCAD. The dc-side of the converter, which comprises of a SCESS, is designed in such a way that the converter emulating $H = 5.0$ s is able to fulfill the active-power requirement during ± 2.0 Hz/s RoCoF event, without exceeding the current through semiconductor devices above the maximum permissible value[4]. The equivalent model shown in

[4]The value of I_{max} selected here is based on the data available for ABB IGBTs from the StakPak series [136]

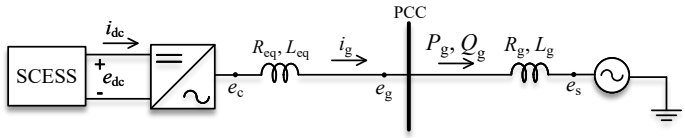

Figure 5.8: Single-line diagram of a grid-connected VSC integrated with SCESS.

Table 5.3: System, control and SCESS design parameters

System parameters		Control parameters		SCESS design parameters	
S_N	112 MVA	L_v	0.5 pu	k_{om}	1.86
E_N	33 kV	R_v	0.25 pu	E_g	33 kV
ω_N	314.16 rad/s	α_{pc}	$2\pi5$ rad/s	ΔE_g	0.1 pu
L_{eq}	0.17 pu	H	5.0 s	X_{eq}	0.17 pu
R_{eq}	0.017 pu	α_{vc}	$2\pi1$ rad/s	I_{max}	2 kA
SCR	3	α_{cc}	$2\pi500$ rad/s	$\Delta\omega_{max}$	$2\pi3$ rad/s

Fig. 5.5, is used to model the SCESS. Table 5.3 describes the system and control parameters, as well as the design parameters of SCESS used for the case study presented here.

The dynamic performance of the ES-STATCOM is evaluated during a frequency excursion in the grid. For this, starting at 0.5 s, the frequency of the ideal-voltage source is varied from 50.0 Hz to 47.0 Hz at a rate of -2.0 Hz/s. Figure 5.9 show the plots of various ac-side quantities of the converter for the specified event. It can be observed from the figure that following the grid disturbance, the internal frequency of the converter (blue curve) closely follows the declining grid frequency (light-blue curve), i.e, the converter stays in synchronism with the ac grid. Immediately after the disturbance, the active-power output of the converter (blue curve) starts to increase and reaches the value corresponding to inertial power, $P_n = P_H = \frac{2H}{\omega_N}\frac{d\omega}{dt} = 0.4$ pu, in steady state. Correspondingly, an increase in the output current of the converter can be observed during the grid disturbance.

Furthermore, it can seen from Fig. 5.10 that throughout the period of inertia support from the converter, the dc-link voltage (blue curve) decreases continuously following its reference value (dashed-red curve). This results in a continuous increase of the current on the dc-side of the converter. Based on the design of the SCESS, the dc-link voltage and current reach their minimum

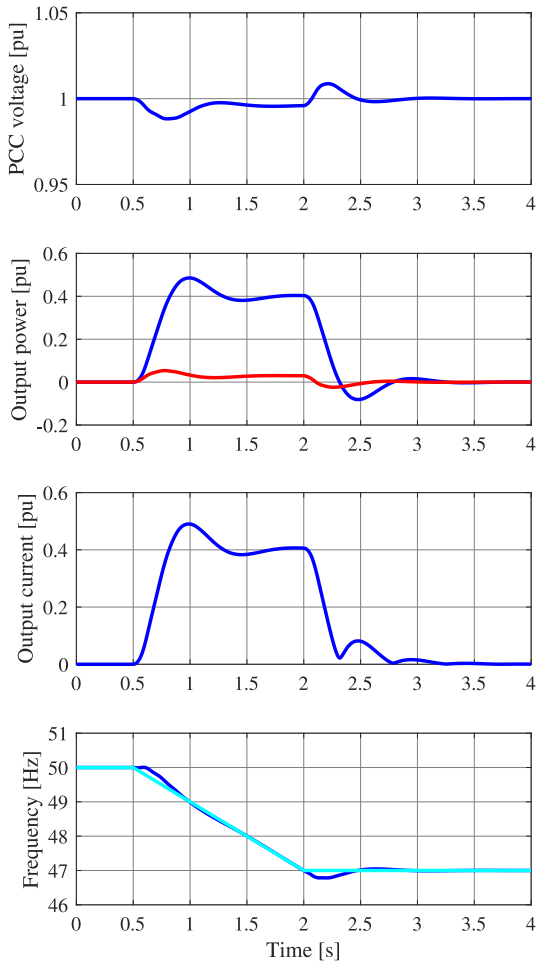

Figure 5.9: Dynamic response at the ac side of the SCESS-based GFM converter during a RoCoF event. From top to bottom: voltage magnitude at the PCC; active power (blue curve) and reactive power (red curve) output of the converter; magnitude of the converter output current; applied variation in the source frequency (light-blue curve), internal frequency of the converter (blue curve).

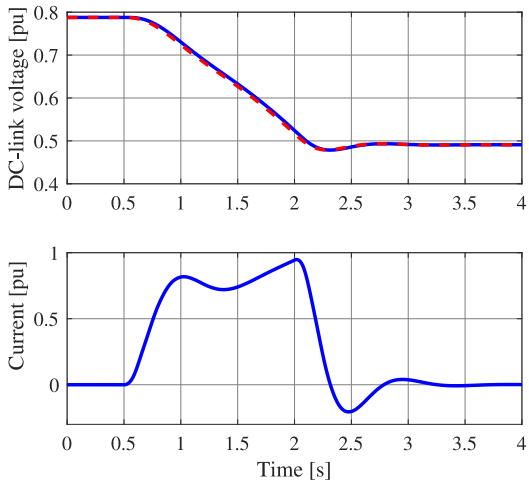

Figure 5.10: Dynamic response at the dc side of the SCESS-based GFM converter during a RoCoF event. Top: dc-link voltage of the converter; bottom: current output of the supercapacitor bank.

and maximum values, respectively, when the grid-frequency reaches 47.0 Hz.

5.6 Summary

In this chapter, the design and modelling of the two most suitable ESTs for the ES-STATCOM, namely, BESS and SCESS has been presented. Furthermore, an alternative control strategy for the GFM converters with SCESS has been proposed, which allows the provision of synthetic inertia support from the converter system without the need to slow down the dc-link voltage controller. The effectiveness of the control strategy and design of the SCESS have been verified using time-domain simulations in PSCAD.

CHAPTER 6

Coordination of wind power plants and synchronous generators

6.1 Introduction

Power systems are designed to operate at a nominal frequency; however, the actual frequency continuously fluctuates around its nominal value due to momentary imbalances between power generation and demand. In order to ensure a safe and reliable operation of the power system, it is necessary that the system frequency lies within a predefined range and does not deviate too far from its nominal value. In case of large frequency deviations protection systems must be activated, causing disconnection of the conventional SGs and loads from the grid. This may lead to widespread power outages and jeopardize the operation of the power system.

In order to regulate the frequency and maintain its quality[1], the frequency control reserves take balancing actions following a mismatch between electricity production and consumption. In this chapter, an overview of frequency

[1]The maximum instantaneous frequency deviation and RoCoF are the key indicators of the frequency quality [137].

control reserves in the Nordic power system is first presented. This is followed by a description of the proposed frequency controller for the ES-STATCOM, which facilitates the provision of frequency support from WPPs. Under the consideration that the future RES-dominated power systems will sill include conventional SGs (for hydro-power production, for instance), the need for a coordinated frequency support from WPPs with the one offered by SGs is motivated next. Finally, the tuning criteria for the proposed frequency controller is presented, which facilitates a natural coordination between WPPs and SGs without a need of any communication signal. The effectiveness of the proposed control strategy is validated in the well-known Kundur's four-machines/two-area system.

6.2 Frequency regulation in the Nordic power system

The Nordic power system is dominated by SGs whose rotational speed dictates the frequency of the system. At present, the kinetic energy stored in the rotating mass of the SGs constitute the largest portion of the power system inertia. In case of small power imbalances, occurring due to stochastic variations in the generation and demand for instance, the inertia prevents sudden changes in the system frequency. During larger imbalances, resulting from disconnection of a generating unit or a system fault, the inertia limits the initial RoCoF, which gives the frequency control reserves a buffer time to act, thereby reducing the risk of potentially large frequency deviations. As the frequency continues to drop, reserves are activated to bring the system frequency back to its nominal value.

The frequency control reserves in the Nordic power system are broadly classified into three categories, namely Frequency Containment Reserve (FCR), Fast Frequency Reserve (FFR) and Frequency Restoration Reserve (FRR) [138]. The FCR is used to stabilize and maintain the frequency within the prescribed limits in case of power imbalances. It activates automatically and responds proportionally to the frequency deviation within certain intervals. FCR is further subdivided into two categories: Frequency Containment Reserve for Normal Operation (FCR-N) and Frequency Containment Reserve for Disturbances (FCR-D). FCR-N is linearly activated within the standard frequency range of 49.9–50.1 Hz [138]. It activates continuously as the fre-

quency fluctuates around 50.0 Hz due to small variations in production and consumption that occur during normal operation. On the other hand, the purpose of the FCR-D is to contain the frequency during disturbances and it is linearly activated between 49.5–49.9 Hz and 50.1–50.5 Hz [138].

With a continuous increase in the penetration level of wind power and a consequent reduction of system inertia in the Nordics, it is anticipated that the response time of the FCR-D may not be fast enough to keep the frequency above a minimum threshold[2] following a dimensioning incident (also referred as a reference or N-1 incident) [138], [139]. Consequently, the FFR was introduced to handle this problem and was implemented in May 2020. FFR provides a very fast active-power support for a short duration, which contributes to containing the frequency until FCR-D is activated. FFR is triggered when the frequency drops below a certain activation threshold which is set at 49.5 Hz, 49.6 Hz or 49.7 Hz. The full activation time of the support is 0.7–1.3 s depending upon the activation threshold. The minimum support duration is either 5 s or 30 s, depending upon how fast the FFR providing unit deactivates its response.

The FRR is used to restore the frequency back to its nominal value of 50.0 Hz after a deviation, thereby relieving FCRs and restoring their capacity. FRR is subdivided further into two categories: automatic FRR (aFRR) and manual FRR (mFRR). Though similar in purpose, the two FRR categories differ in terms of their activation modes. As the name suggests, aFRR is activated automatically and its activation is based on a control signal sent every 10 s by the TSO [138]. On the other hand, the activation of mFRR is ordered by the TSO to reduce existing imbalances or due to forecast of imbalances in the near future.

For a better understanding, Fig. 6.1 shows the operating zones of various frequency control reserves during a fictitious frequency dip in the Nordic power system.

[2]The threshold for minimum instantaneous frequency (i.e. frequency nadir) in the Nordic power system is 49.0 Hz [139]

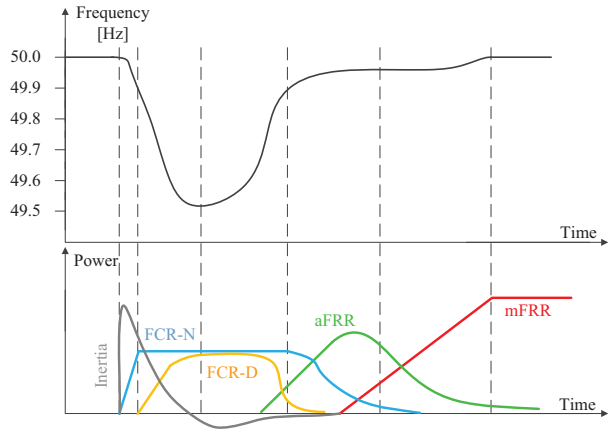

Figure 6.1: Operating zones of various frequency control reserves during a fictitious frequency dip in the Nordic power system [140].

6.3 Proposed structure of the frequency controller and problem formulation

So far in the previous chapters, only the provision of synthetic inertia from the WPP has been considered. In order to provide the FFR provision from the WPP, a frequency controller can be added in parallel to the IEL of the ES-STATCOM as shown in Fig. 6.2. The frequency controller takes the estimated frequency deviation as an input, which is then passed through a high-pass filter having cut-off frequency, α_{hpf}, and gain K_{g}. The triggering function, F_{T}, activates the frequency controller only when the grid frequency drops below a certain threshold set in accordance with the grid codes. Together with the IEL, the frequency controller provides an input to the energy regulator of the ES-STATCOM. Thanks to the high-pass filter, the frequency support from the WPP is provided during transients only. The support is automatically withdrawn when the system frequency reaches a new steady state following a grid disturbance, i.e., when the input frequency deviation to the frequency controller becomes almost constant.

When providing the FFR provision from a converter system, it is essential to coordinate its frequency support with the one offered by the FCR providing units. A coordinated control prevents the reaction time of the FCR providing

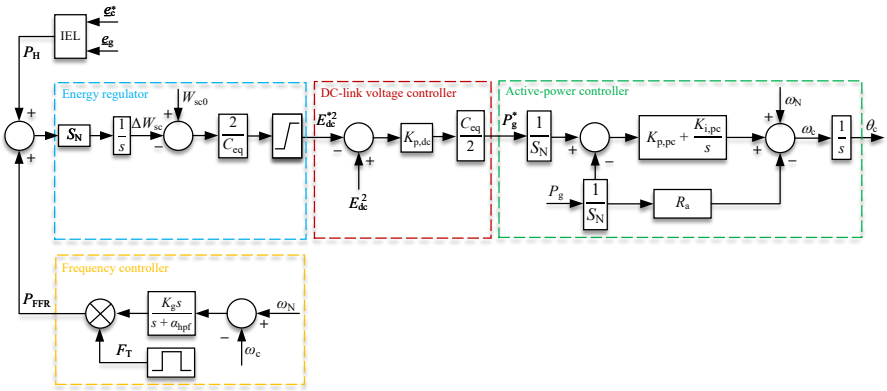

Figure 6.2: Block scheme of the proposed frequency controller.

units from slowing down and reduces the peak-active power as well as energy storage requirements for the converter system. By a careful selection of the parameters for the frequency controller (as described later in Section 6.4), a natural coordination between the FFR and FCR providing units can be achieved. This is exemplified using the test network shown in Fig. 6.3, where a WPP comprising of the WT system and ES-STATCOM is connected to an ac grid via a circuit breaker 'CB1'. For the case studies presented in this section, the synchronous generator 'G2' is kept disconnected. The grid comprises of a constant active-power load 'L1' and a synchronous generator 'G1' connected through a transformer 'T1' and grid impedance of resistance, R_g, and inductance, L_g.

As this study is focused around the Nordic power system in which the hydro units are the main source of FCR [138], a well-established hydro governor model from the Nordic 32 system [141]–[143] is implemented for 'G1', to enable the FCR provision from the SG (see Fig. 6.4). In the considered hydro governor model, the terms τ_w, τ_g and τ_f represent the time constant of the penstock, actuator and frequency-measurement filter, respectively; whereas, R denotes the steady-state frequency droop. $K_{p,g}$ and $K_{i,g}$ are the proportional[3] and integral gains of the hydro governor, respectively, and are selected

[3]The proportional gain is also referred as the transient- or the temporary-droop gain [141], [144].

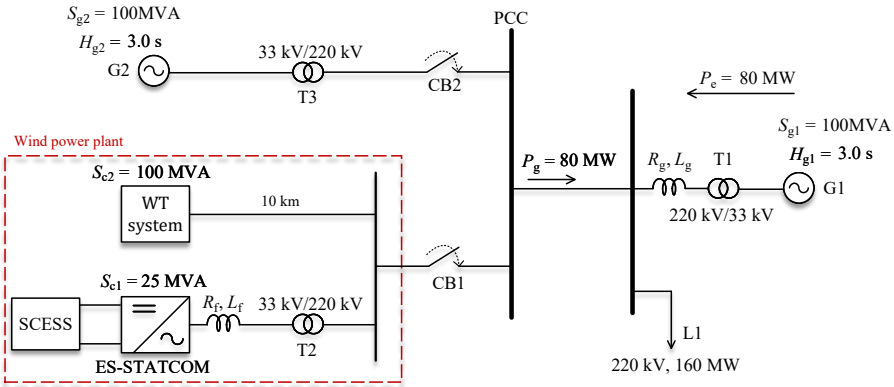

Figure 6.3: Single-line diagram of the test network used to exemplify the need of coordination.

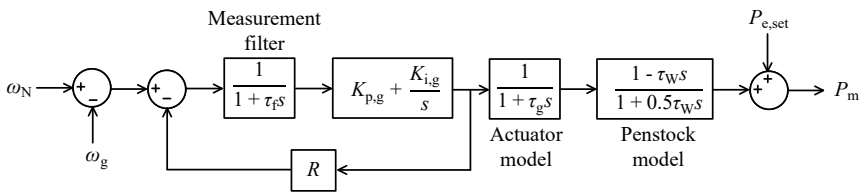

Figure 6.4: Block scheme of the implemented hydro governor model.

as [141], [144]

$$K_{\mathrm{p,g}} = \frac{1}{r_{\mathrm{g}}};\ K_{\mathrm{i,g}} = \frac{1}{r_{\mathrm{g}}\tau_{\mathrm{r,g}}}, \tag{6.1}$$

where r_{g} and $\tau_{\mathrm{r,g}}$ denote the temporary (transient) droop and time constant of the hydro governor, respectively. Some of the typical values for the parameters of the hydro governor model can be found in [141], [144]. Here, $r_{\mathrm{g}} = 0.8$ pu, $\tau_{\mathrm{r,g}} = 5$ s, $\tau_{\mathrm{w}} = 1$ s, $\tau_{\mathrm{g}} = 0.2$ s, $\tau_{\mathrm{f}} = 0.05$ s and $R = 0.04$ pu are selected.

The ratings of various system components as well as the operating point of 'G1' and the WPP considered for the case studies presented here are shown in Fig. 6.3. A frequency disturbance in the grid is simulated by performing a step increase of 3% in the load. The dynamic response of the system following the example disturbance is shown in Fig. 6.5 for the following cases[4]:

- Case A: High value of K_{g} and low value of α_{hpf}: solid-black curves.
- Case B: High value of K_{g} and high value of α_{hpf}: dashed-magenta curves.
- Case C: Low value of K_{g} and low value of α_{hpf}: dotted-blue curves.
- Case D: Low value of K_{g} and high value of α_{hpf}: dashed-dotted green curves.

It can be observed from the bottom figure in Fig. 6.5 that with Case A, the ES-STATCOM supports the increased power demand by injecting a higher amount of active power to the grid for a longer duration as compared to the other cases. Hence, a relatively high frequency nadir (top figure) is obtained as compared to the other cases at the cost of high energy storage requirements for the ES-STATCOM. Furthermore, since the ES-STATCOM supports the increased power demand by injecting a higher active power during the initial stages, the disturbance seen by the SG is small, which results in a slower ramping of its input mechanical power (middle figure). A slower increase in the mechanical power input to the SG indicates a slower contribution from this unit to the frequency regulation and vice versa.

[4] As the primary aim here is to motivate the need of coordination, the parameters of the frequency controller for the ES-STATCOM are selected by trial and error in such a way that either a similar frequency minimum or a similar peak-active power output of the converter is obtained for the considered cases.

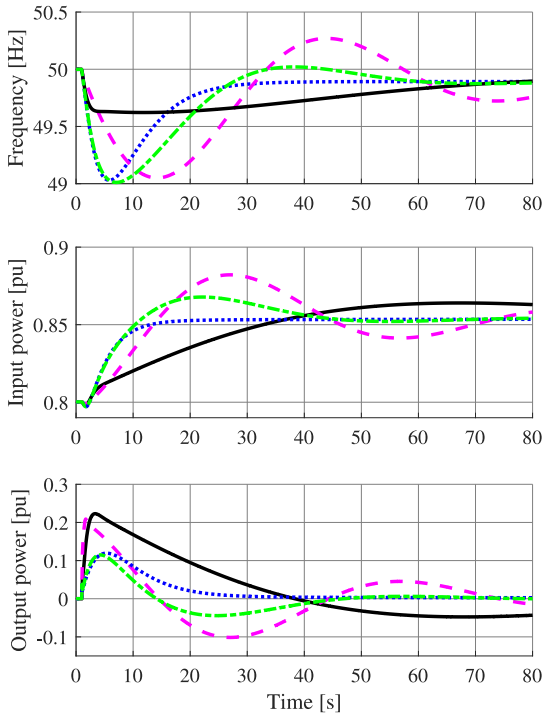

Figure 6.5: Response of the system following a step increase in the load for four different settings of the frequency controller: Case A (solid black), Case B (dashed magenta), Case C (dotted blue), and Case D (dashed-dotted green). From top to bottom: rotor angular speed of 'G1', mechanical power input to 'G1', active power output of the ES-STATCOM.

Increasing α_{hpf} (Case B) results in a quicker removal of the active-power support from the ES-STATCOM as compared to Case A. Although the energy storage requirements in this case are almost half of the previous case, a faster removal of the active-power support from the ES-STATCOM results in a lower frequency nadir and a less damped response close to the steady state. In addition, ramping of the mechanical power input to the SG is still slow; this can be improved further by reducing the value of K_{g} (Cases C & D). Reducing the value of K_{g} reduces the active-power support from the ES-STATCOM during the initial stages, allowing the SG to see a larger disturbance. Consequently, ramping of the mechanical power input to the SG is faster as compared to both Cases A & B. Furthermore, a lower value of K_{g} reduces the peak power of the ES-STATCOM, while still keeping the frequency nadir similar to Case B. A low value of α_{hpf} in Case C provides frequency support from the ES-STATCOM for a longer duration as compared to both Cases B & D. This results in a very-well damped response close to the steady state at the cost of higher energy storage requirements for the ES-STATCOM.

The results from this study reveal that both the FFR and FCR providing units in the power system must work in harmony to provide the necessary frequency support to the system following an electrical disturbance. This not only prevents the full-activation time of the FCR providing units from slowing down, but also reduces the active-power requirements of the FFR providing unit for frequency support, both in terms of peak value and duration. For this, a proper tuning criteria for the two parameters, K_{g} and α_{hpf}, is proposed in the next section, which facilitates a natural coordination between the FFR and FCR providing units in the system.

6.4 Modeling of system frequency dynamics and design of coordinated control

In this section, frequency dynamics of a system comprising of the conventional SGs only is first modeled. The analysis performed using this model serves as the basis for deriving the tuning criterion for the frequency controller of the ES-STATCOM.

6.4.1 Frequency dynamics of a system comprising of synchronous generators only

In order to derive the frequency dynamics of a system comprising of the conventional SGs only, once again the test network shown in Fig. 6.3 is considered. However, in this case, the WPP is disconnected and the synchronous generator 'G2' having an inertia constant, $H_{\mathrm{g2}} = H_{\mathrm{g1}} = 3$ s, and a rated power, $S_{\mathrm{g2}} = S_{\mathrm{g1}} = 100$ MVA, is connected at the PCC. To keep the analysis simple, the same governor model (see Fig. 6.4) and control parameters are used for both the SGs. The frequency dynamics of the system can be understood from a single machine equivalent dynamic model, in which the angular frequency, ω, and inertia constant, H_{COI}, corresponding to the center-of-inertia (COI) of the system are used and expressed as [145], [146]

$$\omega = \frac{\omega_{\mathrm{g1}} H_{\mathrm{g1}} S_{\mathrm{g1}} + \omega_{\mathrm{g2}} H_{\mathrm{g2}} S_{\mathrm{g2}}}{H_{\mathrm{g1}} S_{\mathrm{g1}} + H_{\mathrm{g2}} S_{\mathrm{g2}}}; \quad H_{\mathrm{COI}} = \frac{H_{\mathrm{g1}} S_{\mathrm{g1}} + H_{\mathrm{g2}} S_{\mathrm{g2}}}{S_{\mathrm{N}}}. \tag{6.2}$$

ω_{g1} and ω_{g2} represent the angular frequency of 'G1' and 'G2', respectively, whereas S_{N} denotes the rated power of the system and is expressed as the sum of the rated power of the two SGs for this case, i.e., $S_{\mathrm{N}} = S_{\mathrm{g1}} + S_{\mathrm{g2}}$. Accordingly, the variation in the angular frequency of the system can be expressed using the swing equation in its per-unit form as

$$2H_{\mathrm{COI}} s \Delta\omega = \Delta P_{\mathrm{m}} - \Delta P_{\mathrm{e}}, \tag{6.3}$$

where ΔP_{e} represents the variation in the active power of the electrical load or the input electrical disturbance. ΔP_{m} denotes the total variation in the mechanical power of the system, which by using the governor model of the two SGs can be expressed as

$$\begin{aligned} \Delta P_{\mathrm{m}} = & -\frac{(K_{\mathrm{p,g1}} \frac{S_{\mathrm{g1}}}{S_{\mathrm{N}}} + K_{\mathrm{p,g2}} \frac{S_{\mathrm{g2}}}{S_{\mathrm{N}}}) s + (K_{\mathrm{i,g1}} \frac{S_{\mathrm{g1}}}{S_{\mathrm{N}}} + K_{\mathrm{i,g2}} \frac{S_{\mathrm{g2}}}{S_{\mathrm{N}}})}{s} \\ & . \frac{(-\tau_{\mathrm{w}} s + 1)}{(0.5\tau_{\mathrm{w}} s + 1)} \frac{1}{(\tau_{\mathrm{g}} s + 1)} \Delta\omega. \end{aligned} \tag{6.4}$$

It shall be noted here that in (6.4), the time constant of the frequency-measurement filter has not been considered, due to its negligible impact on the time-scale of interest for frequency support. Furthermore, due to its small

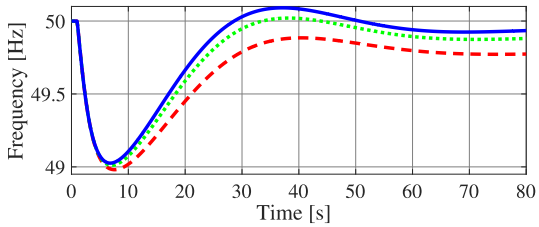

Figure 6.6: Impact of the permanent droop of the governor on frequency dynamics of the system following a step increase in the load for $R = 0.08$ pu (dashed red), 0.04 pu (dotted green), and 0.02 pu (solid blue).

impact during dynamic conditions, the steady-state frequency droop is not included in (6.4). In order to validate this claim, Fig. 6.6 shows the frequency dynamics of the system following a step increase of 3% in the load for three different values of the steady-state droop R. It can be observed that varying R has a very little influence on the initial RoCoF and the frequency nadir, and it only affects the steady-state value of the system frequency following an electrical disturbance.

Using (6.3), (6.4) and denoting by $G(s)$, the transfer function from the input electrical disturbance to the variation in the angular frequency of the system is given by

$$G(s) = \frac{\Delta\omega}{\Delta P_{\mathrm{e}}} = \frac{-1}{2H_{\mathrm{COI}}s + D(s)}. \tag{6.5}$$

$D(s)$ represents the transfer function from the variation in the angular frequency of the system to the total variation in the mechanical power of the system, which using (6.4) is given by

$$\begin{aligned} D(s) = -\frac{\Delta P_{\mathrm{m}}}{\Delta\omega} = \frac{(K_{\mathrm{p,g1}}\frac{S_{\mathrm{g1}}}{S_{\mathrm{N}}} + K_{\mathrm{p,g2}}\frac{S_{\mathrm{g2}}}{S_{\mathrm{N}}})s + (K_{\mathrm{i,g1}}\frac{S_{\mathrm{g1}}}{S_{\mathrm{N}}} + K_{\mathrm{i,g2}}\frac{S_{\mathrm{g2}}}{S_{\mathrm{N}}})}{s} \\ \cdot\frac{(-\tau_{\mathrm{w}}s+1)}{(0.5\tau_{\mathrm{w}}s+1)}\frac{1}{(\tau_{\mathrm{g}}s+1)}. \end{aligned} \tag{6.6}$$

The impact of changing the system inertia and control parameters of one of the two governors on the frequency dynamics of the system following an electrical disturbance is investigated next. This is used as a starting point

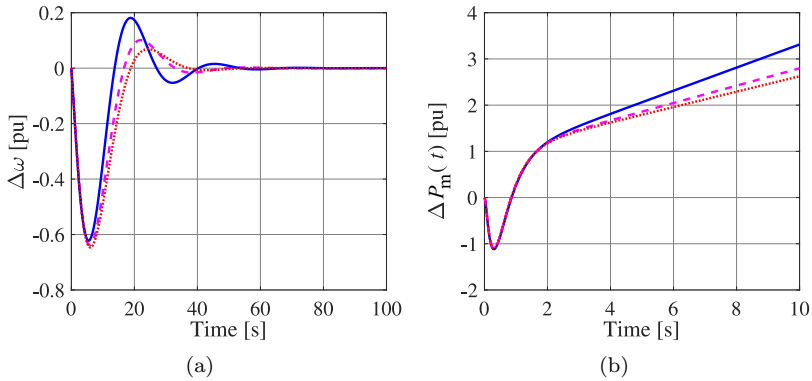

Figure 6.7: Impact of the integral gain of the governor on (a) frequency dynamics of the system following a unit-step disturbance (b) variation in the total mechanical power following a unit step frequency change; for $\tau_{\mathrm{r,g2}} = 2\times$ (dashed magenta), $3\times$ (dotted red) of its initial value (solid blue).

to derive the parameters of the frequency controller for the ES-STATCOM, when one of the conventional SGs is replaced by the WPP.

Influence of the integral gain on the frequency dynamics

The influence of the integral gain on the frequency dynamics is investigated by varying the governor time-constant, $\tau_{\mathrm{r,g2}}$, of the generator 'G2' and plotting the time-domain response of the variation in the angular frequency of the system, $\Delta\omega(t)$, for a unit-step disturbance using (6.5) and (6.6). Fig. 6.7(a) shows the frequency dynamics of the system for three different values of $\tau_{\mathrm{r,g2}}$. It can be observed that varying $\tau_{\mathrm{r,g2}}$ (or alternatively $K_{\mathrm{i,g2}}$) has a very little influence on the frequency nadir, and a significant impact on the recovery of the system frequency. The recovery is slowed down with a decrease in the value of $K_{\mathrm{i,g2}}$. This behaviour can be understood by plotting the time-domain response of the variation in the total mechanical power of the system, $\Delta P_{\mathrm{m}}(t)$, for a unit-step (negative) frequency variation using (6.6). As seen from Fig. 6.7(b), varying $K_{\mathrm{i,g2}}$ has a negligible impact on the total mechanical-power variation of the system during the initial phase of the transient, thus on the frequency nadir following an electrical disturbance. The impact of

reducing $K_{\mathrm{i,g2}}$ is visible only during the later phase of the transient, in terms of a reduced integral action of the governor, leading to a slow recovery of the system frequency.

It shall be noted that in Fig. 6.7(b), the total mechanical-power variation initially decreases instead of increasing. This is resulting from the non-minimum phase property of the hydro turbines. Inside a hydro turbine, when the guide vane is opened after the disturbance to increase the water inflow (so that the power output increases), the water pressure initially drops. Due to this water pressure drop, initially the power output slightly decreases and then increases [145].

Influence of the transient-droop gain on the frequency dynamics

The influence of the transient-droop gain on the frequency dynamics is investigated by varying r_{g2}. Figure 6.8(a) shows the frequency dynamics of the system for three different values of r_{g2}. It can be observed that varying r_{g2} has a significant impact on the frequency nadir, speed of recovery, and damping. The frequency nadir improves when decreasing r_{g2}, or in other words increasing $K_{\mathrm{p,g2}}$. In addition, both the speed of recovery and damping increase when decreasing r_{g2}. This behaviour can be explained by once again plotting $\Delta P_{\mathrm{m}}(t)$. As it can be seen from (6.6) and Fig. 6.8(b), increasing $K_{\mathrm{p,g2}}$ increases the effective transient-droop gain, K_{tr}, which is defined as

$$K_{\mathrm{tr}} = K_{\mathrm{p,g1}} \frac{S_{\mathrm{g1}}}{S_{\mathrm{N}}} + K_{\mathrm{p,g2}} \frac{S_{\mathrm{g2}}}{S_{\mathrm{N}}}. \tag{6.7}$$

This explains for the improvement in the frequency nadir and damping when increasing $K_{\mathrm{p,g2}}$. Furthermore, it can be observed from (6.1), (6.6) and Fig. 6.8(b) that the integral action of the governor also increases when decreasing r_{g2}, leading to a faster recovery of the system frequency.

Influence of the system inertia on the frequency dynamics

Finally, the influence of the system inertia on the frequency dynamics is investigated by varying the inertia constant, H_{coi}. Figure 6.9 shows the frequency dynamics of the system for three different values of H_{coi}. It can be observed that increasing the system inertia improves the frequency nadir; however, as expected, it leads to a slower recovery and a decreased damping.

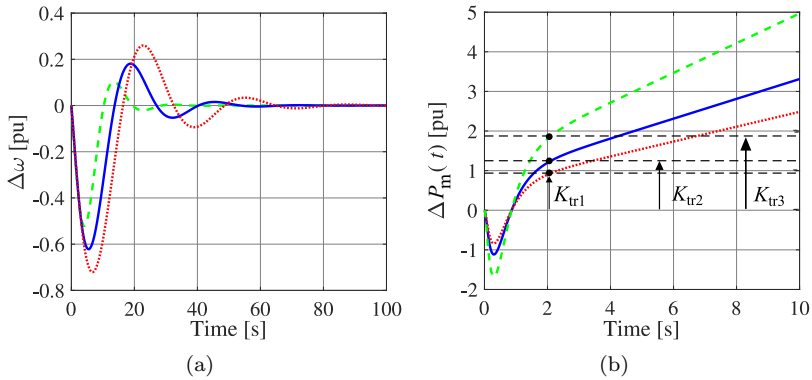

Figure 6.8: Impact of the effective transient-droop gain on (a) frequency dynamics of the system following a unit-step disturbance (b) variation in the total mechanical power following a unit step frequency change; for $r_{g2} = 0.5\times$ (dashed green), $2\times$ (dotted red) of its initial value (solid blue).

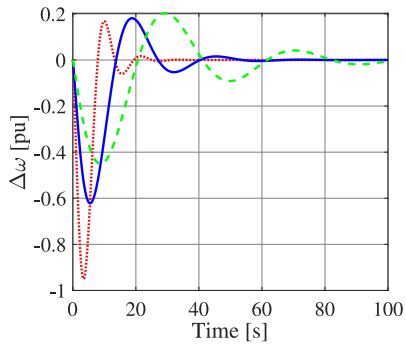

Figure 6.9: Impact of the system inertia on the frequency dynamics following a unit-step disturbance for $H_{coi} = 2.0\times$ (dashed green), $0.5\times$ (dotted red) of its initial value (solid blue).

6.4.2 Frequency dynamics of a system comprising of synchronous generator and WPP

The synchronous generator 'G2' in Fig. 6.3 is now disconnected and replaced by the WPP. In general, this can be seen as the case when a non-environmental friendly power plant is replaced by RES-based power plant. Furthermore, it is considered that the hydro units are still meant to be the main providers of FCR. As the primary goal here is to obtain a tuning criterion for the frequency controller, it is assumed that the inertia emulation from the ES-STATCOM (with $H = 15.0$ s) is accurate to keep the H_{coi} unchanged. In analogy to the previous case of two SGs, the transfer function from the input electrical disturbance to the variation in the angular frequency of the system for this case, $G'(s)$, can be expressed as

$$G'(s) = \frac{\Delta\omega(s)}{\Delta P_{\mathrm{e}}(s)} = \frac{-1}{2H_{\mathrm{coi}}s + D'(s)}, \tag{6.8}$$

with

$$\begin{aligned} D'(s) = -\frac{\Delta P_{\mathrm{m}}}{\Delta\omega} = &\frac{(K_{\mathrm{p,g1}}\frac{S_{\mathrm{g1}}}{S'_{\mathrm{N}}})s + (K_{\mathrm{i,g1}}\frac{S_{\mathrm{g1}}}{S'_{\mathrm{N}}})}{s}\frac{(-\tau_{\mathrm{w}}s+1)}{(0.5\tau_{\mathrm{w}}s+1)}\frac{1}{(\tau_{\mathrm{g}}s+1)} \\ &+ \frac{(K_{\mathrm{g}}\frac{S_{\mathrm{c1}}}{S'_{\mathrm{N}}})s}{(s+\alpha_{\mathrm{hpf}})}. \end{aligned} \tag{6.9}$$

The rated power of the system for this case is expressed as, $S'_{\mathrm{N}} = S_{\mathrm{g1}} + S_{\mathrm{c1}} + S_{\mathrm{c2}}$, with S_{c1} and S_{c2} denoting the rated power of the ES-STATCOM and WT system, respectively.

From the analysis performed in the previous section, it is known that the frequency nadir is greatly influenced by the system inertia and effective transient-droop gain. Since H_{coi} is kept unchanged, to obtain a similar or better performance in terms of the frequency nadir, the effective transient-droop gain for this case, K'_{tr}, should be

$$K'_{\mathrm{tr}} = K_{\mathrm{g}}\frac{S_{\mathrm{c1}}}{S'_{\mathrm{N}}} + K_{\mathrm{p,g1}}\frac{S_{\mathrm{g1}}}{S'_{\mathrm{N}}} \geq K_{\mathrm{tr}}. \tag{6.10}$$

Accordingly, from (6.7) and (6.10), $K_{\mathrm{g}} \geq \frac{K_{\mathrm{p,g1}}S_{\mathrm{g1}}+K_{\mathrm{p,g2}}S_{\mathrm{g2}}}{S_{\mathrm{c1}}}\frac{S'_{\mathrm{N}}}{S_{\mathrm{N}}} - \frac{K_{\mathrm{p,g1}}S_{\mathrm{g1}}}{S_{\mathrm{c1}}}$. In addition, removal of the frequency support from the converter system should

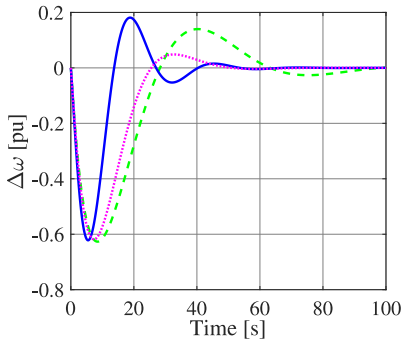

Figure 6.10: Frequency dynamics of the system following a unit-step disturbance for Case A (solid blue), Case B (dashed green), and Case C (dotted magenta).

not take place faster than the increment in the support from the synchronous generator 'G1', which is dictated by the integral gain of its governor. For this, the value of α_{hpf} should be selected smaller than or equal to the integral gain of the hydro governor, i.e., $\alpha_{\text{hpf}} \leq K_{\text{i,g1}} \frac{S_{\text{g1}}}{S'_{\text{N}}}$. The upper limit of K_{g} depends upon the power rating of the ES-STATCOM and capacity of the energy storage, whereas the lower limit of α_{hpf} depends upon the capacity of the energy storage only.

Figure 6.10 shows the frequency dynamics of the test network shown in Fig. 6.3 following a unit-step disturbance for the following three cases:

- Case A: Two synchronous generators in the system (base case): solid-blue curve.
- Case B: One synchronous generator and a WPP in the system with $K_{\text{g}} = 5K_{\text{p,g2}}$ and $\alpha_{\text{hpf}} = 0.44K_{\text{i,g1}}$: dashed-green curve.
- Case C: One synchronous generator and a WPP in the system with $K_{\text{g}} = 5K_{\text{p,g2}}$ and $\alpha_{\text{hpf}} = 0$. This is equivalent to the conventional droop-based frequency controller: dotted-magenta curve.

It can be observed from Fig. 6.10 that in Case B the frequency nadir is very close to that in the base case. However, both the speed of recovery and damping are reduced. These phenomena can be explained by plotting $\Delta P_{\text{m}}(t)$. From Fig. 6.11 it can be observed that the effective transient-droop gains are

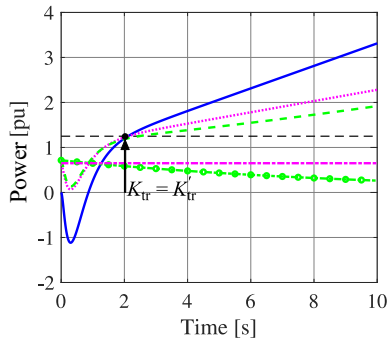

Figure 6.11: Variation in the total mechanical power following a unit step frequency change for Case A (solid blue), Case B (dashed green) and Case C (dotted magenta). Variation in the FFR power of the ES-STATCOM following a unit step frequency change for Case B (green curve with round markers) and Case C (dashed-dotted magenta).

similar for both Cases A & B, i.e., $K_{\mathrm{tr}} = K'_{\mathrm{tr}}$. This explains for a similar frequency nadir in these two cases. It can also be observed from the dashed-green curve in Fig. 6.11 that the integral action is reduced in Case B, which explains for the slower recovery of the system frequency. Furthermore, it can be seen from the green curve with round markers in Fig. 6.11 that the frequency support from the converter decreases over time in Case B, leading to a reduced damping. A decrease in the value of α_{hpf} (Case C) will provide a better damping and an increase in the speed of recovery, as can be visualized from the dotted-magenta curve in Fig. 6.10. However, this is at the cost of an increase in the energy storage requirements of the converter system (dashed-dotted magenta curve in Fig. 6.11).

The tuning criterion for the proposed frequency controller can be generalized as follows: in order to prevent a deterioration of the frequency nadir following a given electrical disturbance, the gain K_{g} of the high-pass filter should be selected such that the effective transient-droop gain after the replacement of the conventional SG is at least equal to the effective transient-droop gain before. Furthermore, the cut-off frequency of the high-pass filter, α_{hpf}, should be at most equal to the effective integral gain of the remaining SGs in the network.

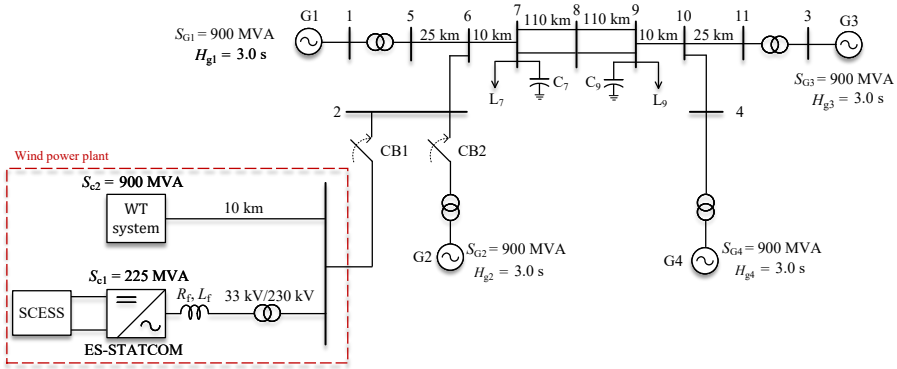

Figure 6.12: Two-area system used to verify the proposed coordination between the wind power plant and hydro generators.

6.5 Simulation verification

As a proof of the concept, the proposed design for the frequency controller of the ES-STATCOM is tested in the well-known Kundur's four-machines/two-area system shown in Fig. 6.12, using detailed time-domain simulation in PSCAD. The ratings of the various system components and the operating point of the SGs are kept the same as in the original model [119]. The inertia constant of 3.0 s and hydro-governor model shown in Fig. 6.4 is implemented for all the SGs. The system model with all four synchronous generators connected is selected as the base-case scenario for comparison purpose. It is found that when a step-increase of 113 MW (corresponding to approximately 4% of the total system load) is applied to the load connected at Bus 7, the frequency nadir of 49.0 Hz is obtained for the base-case scenario. Hence, this is selected as the dimensioning incident in the system.

The synchronous generator 'G2' is now disconnected and replaced by a WPP comprising of a WT system of similar ratings as 'G2' and an ES-STATCOM. The ES-STATCOM is used to regulate the ac voltage at Bus 2 and provide synthetic inertia and frequency support to the system. In order to tune the frequency controller, the relations derived in the previous section are used

here. Accordingly, the values of K_{g} and α_{hpf} are selected as

$$K_{\mathrm{g}} = \frac{K_{\mathrm{p,g1}} S_{\mathrm{g1}} + K_{\mathrm{p,g2}} S_{\mathrm{g2}} + K_{\mathrm{p,g3}} S_{\mathrm{g3}} + K_{\mathrm{p,g4}} S_{\mathrm{g4}}}{S_{\mathrm{c1}}} \frac{S'_{\mathrm{N}}}{S_{\mathrm{N}}} - \frac{K_{\mathrm{p,g1}} S_{\mathrm{g1}} + K_{\mathrm{p,g3}} S_{\mathrm{g3}} + K_{\mathrm{p,g4}} S_{\mathrm{g4}}}{S_{\mathrm{c1}}};$$

$$\alpha_{\mathrm{hpf}} = \frac{K_{\mathrm{i,g1}} S_{\mathrm{g1}} + K_{\mathrm{i,g3}} S_{\mathrm{g3}} + K_{\mathrm{i,g4}} S_{\mathrm{g4}}}{S'_{\mathrm{N}}},$$

with $S_{\mathrm{N}} = S_{\mathrm{g1}} + S_{\mathrm{g2}} + S_{\mathrm{g3}} + S_{\mathrm{g4}}$ and $S'_{\mathrm{N}} = S_{\mathrm{g1}} + S_{\mathrm{c1}} + S_{\mathrm{c2}} + S_{\mathrm{g3}} + S_{\mathrm{g4}}$.

Figure 6.13 shows the frequency dynamics of the system, mechanical power input to 'G1', active power output of the ES-STATCOM and output of its frequency controller (referred as FFR power in the figure), following the dimensioning incident in the system. It can be observed from the figure that providing neither inertia nor frequency support from the WPP leads to a deterioration of the frequency nadir below the acceptable limit. Furthermore, providing only inertia support from the WPP improves the frequency nadir; however, it is still below the acceptable limit. On the other hand, providing both inertia and frequency support makes the frequency nadir in this case equal to the one obtained in the base-case scenario. Thanks to the proposed tuning criterion for the frequency controller, the ramping of the frequency support from the SGs is not deteriorated. This is evident from the plot of mechanical power input to 'G1' with blue and green colors, which have a similar rise time. However, as expected from the theoretical analysis, the recovery of the system frequency in this case is slower than the base case. It shall be noted that in order to fulfill the grid code requirements for the FFR provision, the frequency support from the WPP starts when the system frequency drops below 49.5 Hz in this case, and not directly at the beginning of the transient.

The case studies presented in this section validate the effectiveness of the proposed tuning criterion for the frequency controller of the ES-STATCOM.

6.6 Summary

A coordinated control strategy between the WPP and hydro generators is proposed in this chapter. The fast dynamic properties of the converter system

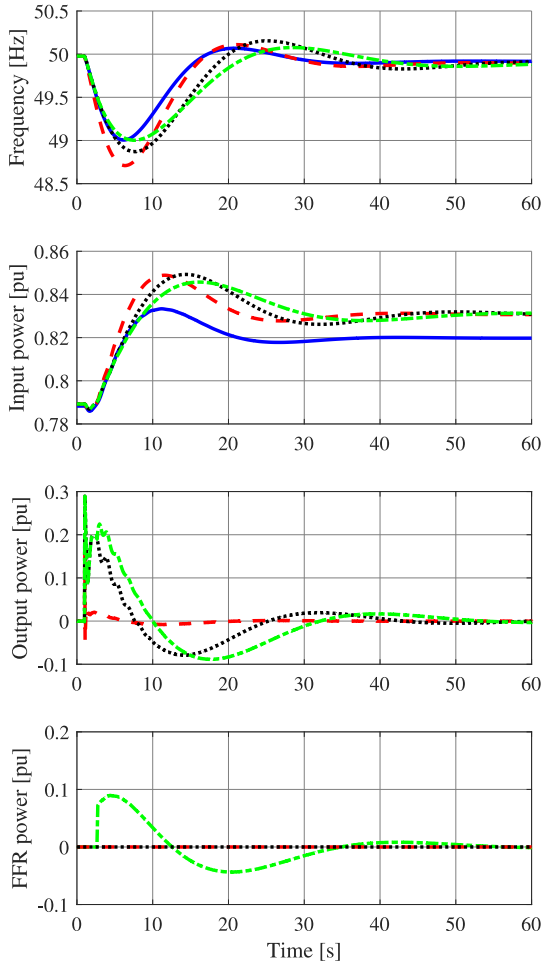

Figure 6.13: Response of the system following the dimensioning incident for four different cases: base-case (solid blue); WPP providing neither inertia nor frequency support (dashed red), inertia support only (dotted black), inertia support as well as frequency support (dashed-dotted green). From top to bottom: frequency corresponding to the COI, mechanical power input to 'G1', acitve power output of the ES-STATCOM, output of the proposed frequency controller.

are utilized to keep the instantaneous frequency following an electrical disturbance within the prescribed limits, without deteriorating the performance of the remaining synchronous generators in the system. This not only improves the frequency quality of the system, but also minimizes the energy storage requirements for the converter system. It is shown that with the proposed tuning criterion for the frequency controller of the ES-STATCOM, a natural coordination can be achieved between the WPP providing the FFR provision and SGs providing the FCR provision. The effectiveness of the proposed coordination is validated in the Kundur's four-machines/two-area system using detailed time-domain simulation in PSCAD.

CHAPTER 7

Conclusions and future Work

7.1 Conclusions

This thesis has dealt with the application of GFM control strategies in WPPs. In particular, the focus of the thesis has been on developing an effective control strategy for the ES-STATCOM that supports the operation of the WPP for different grid conditions, as well as provide the GFM capability to the WPP.

To start with, a PI-regulator based active-power controller with an active damping has been developed for the GFM converters in Chapter 2. This type of control structure prevents the coupling between the damping factor and steady state frequency-droop characteristic of the converter, and also improves the dynamic performance of the converter during variations in the active-power reference. From the comparison of various GFM control strategies made in this chapter, it has been found that the VABC outperforms the other variants in terms of providing more natural response; less control action taking place; less need for fast controllers. Furthermore, due to its resistive-inductive nature, the virtual admittance provides reference-current filtering (through virtual reactance) and damping (through virtual resistance). It also helps in preserving the converter's dynamic performance under varying grid

strengths by reducing the impact of grid impedance on the total impedance variation.

To address the transient-stability problem of the GFM converters during current limitation, a novel limitation strategy and an overall control structure for the GFM converters has been proposed in Chapter 3. From the theoretical analysis performed in this chapter, it has been found that severe grid disturbances resulting in a high RoCoF can cause an instability in GFM converters providing synthetic inertia during current limitation. This is mainly due to the inability of the slow active-power controller to follow the grid-voltage angle during current limitation, thereby resulting in a loss of synchronizm. Consequently, a cascaded structure for the active-power controller consisting of an IEL and a fast APL has been proposed, which effectively decouples the control elements responsible for providing synthetic inertia and grid synchronization in the GFM converters. This gives the flexibility to limit and achieve a fast control over the active-power injection from the converter and ultimately the resulting phase of the virtual back-EMF, when the current limit of the converter is reached. Furthermore, by limiting the magnitude of the virtual back-EMF, the reactive-power injection from the converter can be limited. In this way, current limitation is achieved by dynamically limiting the virtual-back EMF vector without relying on the current limiter. This not only limits the converter current to a desired value, but also preserves the GFM behaviour of the converter even during current limitation. The effectiveness of the proposed current-limitation strategy has been verified using experimental tests.

The GFM capability of a WPP comprising of the WTs in GFL mode and an ES-STATCOM in GFM mode has been investigated in Chapter 4. For this, a detailed time-domain simulation model of a realistic WPP has been developed and the GFM control structure proposed in Chapter 3 has been adopted for the ES-STATCOM. In order to assess the GFM behaviour, the dynamic performance of the WPP in response to various grid disturbances has been analyzed. The simulation tests in this chapter have been performed in accordance with the conformity testing procedures provided by the German VDE FNN. Moreover, the NFP plots have been utilized to further verify the GFM behaviour of the WPP. It has been shown using both simulation results as well as the NFP plots that the ES-STATCOM of an appropriate size, which is operated using the proposed GFM control strategy, has a potential to offer

a certain degree of the GFM capability to the overall WPP. Furthermore, it aids in the operation of the WPP during weak grid conditions.

An overview of various ESTs has been provided in Chapter 5. Recommendations have been made for design and sizing of the two most suitable ESTs, i.e., BESS and SCESS, for providing ancillary services from the WPPs. Furthermore, a modified control strategy for the SCESS-based GFM converters has been presented, which allows the provision of synthetic inertia or FFR from the converter without compromising the speed of response of the dc-voltage controller. This is achieved by varying the reference for the dc-voltage controller based on the energy requirements of the given application.

Finally, a coordinated control strategy between the WPP and SGs in the grid has been proposed in Chapter 6, which enables the FFR provision from the WPP. Thanks to the proposed coordinated control, the fast dynamic properties of the converter can be utilized to improve the frequency quality of the power system, without deteriorating the performance of the remaining SGs in the grid. Furthermore, a coordinated control reduces the energy storage requirements for the converter system. It has been shown that by properly tuning the frequency controller of the ES-STATCOM, a natural coordination between the FFR provision from the WPP and the FCR provision from the SGs can be achieved. The effectiveness of the proposed tuning criterion has been validated using detailed EMT simulations.

7.2 Future work

The main focus of this thesis has been on developing an effective GFM control strategy for ESS used in WPPs. With the proposed GFM control structure, the grid synchronization of the converter is realized through the active-power controller, while the dc-link voltage controller generates the active-power reference. It can be of interest to analyze the possibility to provide grid synchronization directly from the dc-link voltage controller and investigate its impact on the stability of the converter compared to the power-based synchronization approach, especially when the energy storage is limited. In addition, analyzing the impact of the IEL and dc-link voltage controller on the small-signal dynamics of the converter could be an interesting task. Furthermore, expanding the concept of NFP for systems without SGs and relating it to the passivity behaviour can be useful to analyze stability of the future power

systems. Finally, it could be interesting to develop a centralized controller for the WPP that provides set points to the converter systems in WTs as well as ES-STATCOM to distribute various grid support services such as fast-fault current injection and inertia provision, and investigate its impact on the GFM behaviour of the WPP.

References

[1] United Nations Framework Convention on Climate Change, "Adoption of the Paris Agreement," 2015.

[2] B. Kroposki, B. Johnson, Y. Zhang, *et al.*, "Achieving a 100% renewable grid: Operating electric power systems with extremely high levels of variable renewable energy," *IEEE Power and Energy Magazine*, vol. 15, no. 2, pp. 61–73, 2017.

[3] GWEC, "Global Wind Report 2022," 2022.

[4] H. Urdal, R. Ierna, J. Zhu, C. Ivanov, A. Dahresobh, and D. Rostom, "System strength considerations in a converter dominated power system," *IET Renewable Power Generation*, vol. 9, no. 1, pp. 10–17, 2015.

[5] F. Milano, F. Dörfler, G. Hug, D. J. Hill, and G. Verbič, "Foundations and Challenges of Low-Inertia Systems (Invited Paper)," in *2018 Power Systems Computation Conference (PSCC)*, 2018, pp. 1–25.

[6] M. G. Dozein, P. Mancarella, T. K. Saha, and R. Yan, "System Strength and Weak Grids: Fundamentals, Challenges, and Mitigation Strategies," in *2018 Australasian Universities Power Engineering Conference (AUPEC)*, 2018, pp. 1–7.

[7] ENTSO-e, "High penetration of power electronic interfaced power sources and the potential contribution of grid forming converters," 2020.

[8] B. Shakerighadi, N. Johansson, R. Eriksson, *et al.*, "An overview of stability challenges for power-electronic-dominated power systems: The grid-forming approach," *IET Generation, Transmission & Distribution*, vol. 17, no. 2, pp. 284–306, 2023.

[9] M. Tsili and S. Papathanassiou, "A review of grid code technical requirements for wind farms," *IET Renewable Power Generation*, vol. 3, no. 3, pp. 308–332, 2009.

[10] "IEEE Standard for Interconnection and Interoperability of Distributed Energy Resources with Associated Electric Power Systems Interfaces," *IEEE Std 1547-2018 (Revision of IEEE Std 1547-2003)*, pp. 1–138, 2018.

[11] E. Nycander and L. Söder, "Review of european grid codes for wind farms and their implications for wind power curtailments," in *17th International Wind Integration Workshop Stockholm, Sweden/ 17–19 October 2018*, 2018.

[12] T. K. Vrana, A. Attya, and L. Trilla, "Future-oriented generic grid code regarding wind power plants in Europe," *International Journal of Electrical Power & Energy Systems*, vol. 125, p. 106 490, 2021, ISSN: 0142-0615.

[13] European Commission, "COMMISSION REGULATION (EU) 2016/1447 - establishing a network code on requirements for grid connection of high voltage direct current systems and direct current-connected power park modules," *Official Journal of the European Union*, vol. 1447, pp. 1–65, 2016.

[14] Energimarknadsinspektionen, "Energimarknadsinspektionens föreskrifter om fastställande av generellt tillämpliga krav för nätanslutning av system för högspänd likström och likströmsanslutna kraftparksmoduler," 2019.

[15] Verband der Elektrotechnik Elektronik Informationstechnik e. V., "Technical requirements for grid connection of high voltage direct current systems and direct current-connected power park modules (VDE-AR-N 4131 TAR HVDC)," 2019.

[16] "IEEE Standard for Interconnection and Interoperability of Inverter-Based Resources (IBRs) Interconnecting with Associated Transmission Electric Power Systems," *IEEE Std 2800-2022*, pp. 1–180, 2022.

[17] National Grid ESO, "Grid Code (GC) GC0137: Minimum Specification Required for Provision of GB Grid Forming (GBGF) Capability (formerly Virtual Synchronous Machine (VSM) Capability) (GC0137).," 2022.

[18] T. Ackermann, T. Prevost, V. Vittal, A. J. Roscoe, J. Matevosyan, and N. Miller, "Paving the Way: A Future Without Inertia Is Closer Than You Think," *IEEE Power and Energy Magazine*, vol. 15, no. 6, pp. 61–69, 2017.

[19] Y. Lin, J. H. Eto, B. B. Johnson, *et al.*, "Research roadmap on grid-forming inverters," National Renewable Energy Lab.(NREL), Golden, CO (United States), Tech. Rep., 2020.

[20] S. A. Khan, M. Wang, W. Su, G. Liu, and S. Chaturvedi, "Grid-Forming Converters for Stability Issues in Future Power Grids," *Energies*, vol. 15, no. 14, 2022, ISSN: 1996-1073.

[21] R. Musca, A. Vasile, and G. Zizzo, "Grid-forming converters. a critical review of pilot projects and demonstrators," *Renewable and Sustainable Energy Reviews*, vol. 165, p. 112 551, 2022, ISSN: 1364-0321.

[22] L. Huang, C. Wu, D. Zhou, L. Chen, D. Pagnani, and F. Blaabjerg, "Challenges and potential solutions of grid-forming converters applied to wind power generation system—An overview," *Frontiers in Energy Research*, vol. 11, pp. 1–14, 2023, ISSN: 2296-598X.

[23] J. Matevosyan, B. Badrzadeh, T. Prevost, *et al.*, "Grid-Forming Inverters: Are They the Key for High Renewable Penetration?" *IEEE Power and Energy Magazine*, vol. 17, no. 6, pp. 89–98, 2019.

[24] R. H. Lasseter, Z. Chen, and D. Pattabiraman, "Grid-Forming Inverters: A Critical Asset for the Power Grid," *IEEE Journal of Emerging and Selected Topics in Power Electronics*, vol. 8, no. 2, pp. 925–935, 2020.

[25] K. De Brabandere, B. Bolsens, J. Van den Keybus, A. Woyte, J. Driesen, and R. Belmans, "A Voltage and Frequency Droop Control Method for Parallel Inverters," *IEEE Transactions on Power Electronics*, vol. 22, no. 4, pp. 1107–1115, 2007.

[26] S. D'Arco, J. A. Suul, and O. B. Fosso, "A Virtual Synchronous Machine implementation for distributed control of power converters in SmartGrids," *Electric Power Systems Research*, vol. 122, pp. 180–197, 2015, ISSN: 0378-7796.

[27] B. B. Johnson, M. Sinha, N. G. Ainsworth, F. Dörfler, and S. V. Dhople, "Synthesizing Virtual Oscillators to Control Islanded Inverters," *IEEE Transactions on Power Electronics*, vol. 31, no. 8, pp. 6002–6015, 2016.

[28] P. Rodríguez, C. Citro, J. I. Candela, J. Rocabert, and A. Luna, "Flexible Grid Connection and Islanding of SPC-Based PV Power Converters," *IEEE Transactions on Industry Applications*, vol. 54, no. 3, pp. 2690–2702, 2018.

[29] C. Arghir, T. Jouini, and F. Dörfler, "Grid-forming control for power converters based on matching of synchronous machines," *Automatica*, vol. 95, pp. 273–282, 2018, ISSN: 0005-1098.

[30] L. Harnefors, M. Hinkkanen, U. Riaz, F. M. M. Rahman, and L. Zhang, "Robust Analytic Design of Power-Synchronization Control," *IEEE Transactions on Industrial Electronics*, vol. 66, no. 8, pp. 5810–5819, 2019.

[31] M. Ndreko, S. Rüberg, and W. Winter, "Grid forming control scheme for power systems with up to 100% power electronic interfaced generation: a case study on Great Britain test system," *IET Renewable Power Generation*, vol. 14, no. 8, pp. 1268–1281, 2020.

[32] H.-P. Beck and R. Hesse, "Virtual synchronous machine," in *2007 9th international conference on electrical power quality and utilisation*, IEEE, 2007, pp. 1–6.

[33] L. Zhang, L. Harnefors, and H.-P. Nee, "Power-Synchronization Control of Grid-Connected Voltage-Source Converters," *IEEE Transactions on Power Systems*, vol. 25, no. 2, pp. 809–820, 2010.

[34] Q.-C. Zhong and G. Weiss, "Synchronverters: Inverters That Mimic Synchronous Generators," *IEEE Transactions on Industrial Electronics*, vol. 58, no. 4, pp. 1259–1267, 2011.

[35] S. D'Arco and J. A. Suul, "Virtual synchronous machines — Classification of implementations and analysis of equivalence to droop controllers for microgrids," in *2013 IEEE Grenoble Conference*, 2013, pp. 1–7.

[36] P. Rodriguez, I. Candela, C. Citro, J. Rocabert, and A. Luna, "Control of grid-connected power converters based on a virtual admittance control loop," in *2013 15th European Conference on Power Electronics and Applications (EPE)*, 2013, pp. 1–10.

[37] H. Bevrani, T. Ise, and Y. Miura, "Virtual synchronous generators: A survey and new perspectives," *International Journal of Electrical Power & Energy Systems*, vol. 54, pp. 244–254, 2014, ISSN: 0142-0615.

[38] Q.-C. Zhong, P.-L. Nguyen, Z. Ma, and W. Sheng, "Self-Synchronized Synchronverters: Inverters Without a Dedicated Synchronization Unit," *IEEE Transactions on Power Electronics*, vol. 29, no. 2, pp. 617–630, 2014.

[39] D. Remon, A. M. Cantarellas, E. Rakhshani, I. Candela, and P. Rodriguez, "An active power synchronization control loop for grid-connected converters," in *2014 IEEE PES General Meeting | Conference & Exposition*, 2014, pp. 1–5.

[40] R. Rosso, X. Wang, M. Liserre, X. Lu, and S. Engelken, "Grid-Forming Converters: Control Approaches, Grid-Synchronization, and Future Trends — A Review," *IEEE Open Journal of Industry Applications*, vol. 2, pp. 93–109, 2021.

[41] Enstore, "Enstore updated guide for GB Grid Forming Converters – V-005," Tech. Rep., 2021.

[42] NERC, "Grid Forming Technology - Bulk Power System Reliability Considerations," Tech. Rep., 2021.

[43] National Grid ESO, "NOA Stability Pathfinder Phase 3 - Technical Performance Requirements," Tech. Rep., 2022.

[44] T. Qoria, F. Gruson, F. Colas, X. Kestelyn, and X. Guillaud, "Current limiting algorithms and transient stability analysis of grid-forming VSCs," *Electric Power Systems Research*, vol. 189, p. 106 726, 2020, ISSN: 0378-7796.

[45] B. Fan, T. Liu, F. Zhao, H. Wu, and X. Wang, "A Review of Current-Limiting Control of Grid-Forming Inverters Under Symmetrical Disturbances," *IEEE Open Journal of Power Electronics*, vol. 3, pp. 955–969, 2022.

[46] Q.-C. Zhong and G. C. Konstantopoulos, "Current-Limiting Droop Control of Grid-Connected Inverters," *IEEE Transactions on Industrial Electronics*, vol. 64, no. 7, pp. 5963–5973, 2017.

[47] I. Sadeghkhani, M. E. Hamedani Golshan, J. M. Guerrero, and A. Mehrizi-Sani, "A Current Limiting Strategy to Improve Fault Ride-Through of Inverter Interfaced Autonomous Microgrids," *IEEE Transactions on Smart Grid*, vol. 8, no. 5, pp. 2138–2148, 2017.

[48] M. G. Taul, X. Wang, P. Davari, and F. Blaabjerg, "Current Limiting Control With Enhanced Dynamics of Grid-Forming Converters During Fault Conditions," *IEEE Journal of Emerging and Selected Topics in Power Electronics*, vol. 8, no. 2, pp. 1062–1073, 2020.

[49] A. D. Paquette and D. M. Divan, "Virtual Impedance Current Limiting for Inverters in Microgrids With Synchronous Generators," *IEEE Transactions on Industry Applications*, vol. 51, no. 2, pp. 1630–1638, 2015.

[50] X. Lu, J. Wang, J. M. Guerrero, and D. Zhao, "Virtual-Impedance-Based Fault Current Limiters for Inverter Dominated AC Microgrids," *IEEE Transactions on Smart Grid*, vol. 9, no. 3, pp. 1599–1612, 2018.

[51] B. Wang, R. Burgos, and B. Wen, "Grid-Forming Inverter Control Strategy with Improved Fault Ride Through Capability," in *2022 IEEE Energy Conversion Congress and Exposition (ECCE)*, 2022, pp. 1–8.

[52] H. Xin, L. Huang, L. Zhang, Z. Wang, and J. Hu, "Synchronous Instability Mechanism of P-f Droop-Controlled Voltage Source Converter Caused by Current Saturation," *IEEE Transactions on Power Systems*, vol. 31, no. 6, pp. 5206–5207, 2016.

[53] L. Huang, H. Xin, Z. Wang, L. Zhang, K. Wu, and J. Hu, "Transient Stability Analysis and Control Design of Droop-Controlled Voltage Source Converters Considering Current Limitation," *IEEE Transactions on Smart Grid*, vol. 10, no. 1, pp. 578–591, 2019.

[54] K. V. Kkuni and G. Yang, "Effects of current limit for grid forming converters on transient stability: analysis and solution," *arXiv preprint arXiv:2106.13555*, 2021.

[55] Z. Jin and X. Wang, "A DQ-Frame Asymmetrical Virtual Impedance Control for Enhancing Transient Stability of Grid-Forming Inverters," *IEEE Transactions on Power Electronics*, vol. 37, no. 4, pp. 4535–4544, 2022.

[56] L. Huang, C. Wu, D. Zhou, and F. Blaabjerg, "A Power-Angle-Based Adaptive Overcurrent Protection Scheme for Grid-Forming Inverter Under Large Grid Disturbances," *IEEE Transactions on Industrial Electronics*, vol. 70, no. 6, pp. 5927–5936, 2023.

[57] T. Midtsund, J. A. Suul, and T. Undeland, "Evaluation of current controller performance and stability for voltage source converters connected to a weak grid," in *The 2nd International Symposium on Power Electronics for Distributed Generation Systems*, 2010, pp. 382–388.

[58] J. Z. Zhou, H. Ding, S. Fan, Y. Zhang, and A. M. Gole, "Impact of Short-Circuit Ratio and Phase-Locked-Loop Parameters on the Small-Signal Behavior of a VSC-HVDC Converter," *IEEE Transactions on Power Delivery*, vol. 29, no. 5, pp. 2287–2296, 2014.

[59] D. Dong, B. Wen, D. Boroyevich, P. Mattavelli, and Y. Xue, "Analysis of Phase-Locked Loop Low-Frequency Stability in Three-Phase Grid-Connected Power Converters Considering Impedance Interactions," *IEEE Transactions on Industrial Electronics*, vol. 62, no. 1, pp. 310–321, 2015.

[60] L. Huang, H. Xin, W. Dong, and F. Dörfler, "Impacts of grid structure on PLL-synchronization stability of converter-integrated power systems," *IFAC-PapersOnLine*, vol. 55, no. 13, pp. 264–269, 2022.

[61] H. Gong, X. Wang, and L. Harnefors, "Rethinking Current Controller Design for PLL-Synchronized VSCs in Weak Grids," *IEEE Transactions on Power Electronics*, vol. 37, no. 2, pp. 1369–1381, 2022.

[62] F. Díaz-González, A. Sumper, O. Gomis-Bellmunt, and R. Villafáfila-Robles, "A review of energy storage technologies for wind power applications," *Renewable and Sustainable Energy Reviews*, vol. 16, no. 4, pp. 2154–2171, 2012, ISSN: 1364-0321.

[63] H. Zhao, Q. Wu, S. Hu, H. Xu, and C. N. Rasmussen, "Review of energy storage system for wind power integration support," *Applied Energy*, vol. 137, pp. 545–553, 2015, ISSN: 0306-2619.

[64] WindEurope, "Wind energy and on-site energy storage - Exploring Market Opportunities," Tech. Rep., 2017.

[65] S. Chaudhary, X. Wang, D. Yang, *et al.*, "Techno-economic Feasibility of a STATCOM with Battery Energy Storage for the Offshore Wind Power Plants," in *Proceedings of CIGRE Symposium Aalborg 2019*, CIGRE (International Council on Large Electric Systems), 2019.

[66] M. Bongiorno, "On control of grid-connected voltage source converters," *Chalmers University of Technology, Gothenburg, Sweden, PhD Thesis*, 2007.

[67] J. Rocabert, A. Luna, F. Blaabjerg, and P. Rodríguez, "Control of Power Converters in AC Microgrids," *IEEE Transactions on Power Electronics*, vol. 27, no. 11, pp. 4734–4749, 2012.

[68] P. Imgart, M. Beza, M. Bongiorno, and J. R. Svensson, "An Overview of Grid-Connection Requirements for Converters and Their Impact on Grid-Forming Control," in *2022 24th European Conference on Power Electronics and Applications (EPE'22 ECCE Europe)*, 2022, pp. 1–10.

[69] P. Unruh, M. Nuschke, P. Strauß, and F. Welck, "Overview on Grid-Forming Inverter Control Methods," *Energies*, vol. 13, no. 10, 2020, ISSN: 1996-1073.

[70] S. Anttila, J. S. Döhler, J. G. Oliveira, and C. Boström, "Grid Forming Inverters: A Review of the State of the Art of Key Elements for Microgrid Operation," *Energies*, vol. 15, no. 15, 2022, ISSN: 1996-1073.

[71] ENTSO-e, "Grid-Forming Capabilities: Towards System Level Integration," 2021.

[72] M. Beza, "Power System Stability Enhancement Using Shunt-connected Power Electronic Devices with Active Power Injection Capability," *Chalmers University of Technology, Gothenburg, Sweden, PhD Thesis*, 2015.

[73] A. Narula, M. Bongiorno, M. Beza, J. R. Svensson, X. Guillaud, and L. Harnefors, "Impact of steady-state grid-frequency deviations on the performance of grid-forming converter control strategies," in *2020 22nd European Conference on Power Electronics and Applications (EPE'20 ECCE Europe)*, 2020, P.1–P.10.

[74] E. Rokrok, T. Qoria, A. Bruyere, B. Francois, and X. Guillaud, "Classification and dynamic assessment of droop-based grid-forming control schemes: Application in HVDC systems," *Electric Power Systems Research*, vol. 189, p. 106 765, 2020, ISSN: 0378-7796.

[75] L. Harnefors, L. Zhang, and M. Bongiorno, "Frequency-domain passivity-based current controller design," *IET Power Electronics*, vol. 1, 455–465(10), 4 2008, ISSN: 1755-4535.

[76] A. Narula, M. Bongiorno, M. Beza, and P. Chen, "Tuning and evaluation of grid-forming converters for grid-support," in *2021 23rd European Conference on Power Electronics and Applications (EPE'21 ECCE Europe)*, 2021, P.1–P.10.

[77] T. Qoria, F. Gruson, F. Colas, X. Guillaud, M.-S. Debry, and T. Prevost, "Tuning of Cascaded Controllers for Robust Grid-Forming Voltage Source Converter," in *2018 Power Systems Computation Conference (PSCC)*, 2018, pp. 1–7.

[78] L. Harnefors, M. Bongiorno, and S. Lundberg, "Input-Admittance Calculation and Shaping for Controlled Voltage-Source Converters," *IEEE Transactions on Industrial Electronics*, vol. 54, no. 6, pp. 3323–3334, 2007.

[79] M. Beza and M. Bongiorno, "On the Risk for Subsynchronous Control Interaction in Type 4 Based Wind Farms," *IEEE Transactions on Sustainable Energy*, vol. 10, no. 3, pp. 1410–1418, 2019.

[80] G. Francis, R. Burgos, D. Boroyevich, F. Wang, and K. Karimi, "An algorithm and implementation system for measuring impedance in the d-q domain," in *2011 IEEE Energy Conversion Congress and Exposition*, 2011, pp. 3221–3228.

[81] M. Beza and M. Bongiorno, "Impact of converter control strategy on low- and high-frequency resonance interactions in power-electronic dominated systems," *International Journal of Electrical Power & Energy Systems*, vol. 120, p. 105 978, 2020, ISSN: 0142-0615.

[82] M. Beza and M. Bongiorno, "Identification of resonance interactions in offshore-wind farms connected to the main grid by MMC-based HVDC system," *International Journal of Electrical Power & Energy Systems*, vol. 111, pp. 101–113, 2019, ISSN: 0142-0615.

[83] P. Imgart, A. Narula, M. Bongiorno, M. Beza, and J. R. Svensson, "A Cascaded Power Controller for Robust Frequency Ride-Through of Grid-Forming Converters," in *2022 IEEE Energy Conversion Congress and Exposition (ECCE)*, 2022, pp. 1–8.

[84] X. Wang, M. G. Taul, H. Wu, Y. Liao, F. Blaabjerg, and L. Harnefors, "Grid-Synchronization Stability of Converter-Based Resources—An Overview," *IEEE Open Journal of Industry Applications*, vol. 1, pp. 115–134, 2020.

[85] J. Alipoor, Y. Miura, and T. Ise, "Power System Stabilization Using Virtual Synchronous Generator With Alternating Moment of Inertia," *IEEE Journal of Emerging and Selected Topics in Power Electronics*, vol. 3, no. 2, pp. 451–458, 2015.

[86] H. Wu and X. Wang, "A Mode-Adaptive Power-Angle Control Method for Transient Stability Enhancement of Virtual Synchronous Generators," *IEEE Journal of Emerging and Selected Topics in Power Electronics*, vol. 8, no. 2, pp. 1034–1049, 2020.

[87] R. Rosso, M. Andresen, S. Engelken, and M. Liserre, "Analysis of the Interaction Among Power Converters Through Their Synchronization Mechanism," *IEEE Transactions on Power Electronics*, vol. 34, no. 12, pp. 12 321–12 332, 2019.

[88] M. van Wesenbeeck, S. de Haan, P. Varela, and K. Visscher, "Grid tied converter with virtual kinetic storage," in *2009 IEEE Bucharest PowerTech*, 2009, pp. 1–7.

[89] Australian Energy Market Operator, "Trip of multiple generators and lines in Central Queensland and associated under-frequency load shedding on 25 May 2021," Oct. 2021.

[90] ENTSO-e, "Continental Europe Synchronous Area Separation on 24 July 2021 - Technical report," Nov. 12, 2021.

[91] Verband der Elektrotechnik Elektronik Informationstechnik e. V., *Technical Connection Rules for High-Voltage (VDE-AR-N 4120)*, Nov. 2018.

[92] M. Beza and M. Bongiorno, "Application of Recursive Least Squares Algorithm With Variable Forgetting Factor for Frequency Component Estimation in a Generic Input Signal," *IEEE Transactions on Industry Applications*, vol. 50, no. 2, pp. 1168–1176, Mar. 2014, ISSN: 1939-9367.

[93] GWEC, "Global Wind Report 2022," 2023.

[94] GWEC, "Global Offshore Wind Report 2022," 2023.

[95] Z. Yang, C. Shen, L. Zhang, M. Crow, and S. Atcitty, "Integration of a StatCom and battery energy storage," *IEEE Transactions on Power Systems*, vol. 16, no. 2, pp. 254–260, 2001.

[96] M. Pereira, D. Retzmann, J. Lottes, M. Wiesinger, and G. Wong, "SVC PLUS: An MMC STATCOM for network and grid access applications," in *2011 IEEE Trondheim PowerTech*, 2011, pp. 1–5.

[97] T. Soong and P. W. Lehn, "Evaluation of Emerging Modular Multilevel Converters for BESS Applications," *IEEE Transactions on Power Delivery*, vol. 29, no. 5, pp. 2086–2094, 2014.

[98] M. Vasiladiotis and A. Rufer, "Analysis and Control of Modular Multilevel Converters With Integrated Battery Energy Storage," *IEEE Transactions on Power Electronics*, vol. 30, no. 1, pp. 163–175, 2015.

[99] E. Spahic, C. P. Susai Sakkanna Reddy, M. Pieschel, and R. Alvarez, "Multilevel STATCOM with power intensive energy storage for dynamic grid stability - frequency and voltage support," in *2015 IEEE Electrical Power and Energy Conference (EPEC)*, 2015, pp. 73–80.

[100] C. Han, A. Q. Huang, M. E. Baran, *et al.*, "STATCOM Impact Study on the Integration of a Large Wind Farm into a Weak Loop Power System," *IEEE Transactions on Energy Conversion*, vol. 23, no. 1, pp. 226–233, 2008.

[101] M. Molinas, J. A. Suul, and T. Undeland, "Low Voltage Ride Through of Wind Farms With Cage Generators: STATCOM Versus SVC," *IEEE Transactions on Power Electronics*, vol. 23, no. 3, pp. 1104–1117, 2008.

[102] M. S. El-Moursi, B. Bak-Jensen, and M. H. Abdel-Rahman, "Novel STATCOM Controller for Mitigating SSR and Damping Power System Oscillations in a Series Compensated Wind Park," *IEEE Transactions on Power Electronics*, vol. 25, no. 2, pp. 429–441, 2010.

[103] L. Wang and D.-N. Truong, "Stability Enhancement of DFIG-Based Offshore Wind Farm Fed to a Multi-Machine System Using a STATCOM," *IEEE Transactions on Power Systems*, vol. 28, no. 3, pp. 2882–2889, 2013.

[104] L. Kocewiak, M. Gautschi, L. Zeni, *et al.*, "Power quality improvement of wind power plants by active filters embedded in statcoms," in *Proc. 15th Int. Workshop Large-Scale Integr. Wind Power Into Power Syst. As Well As Transmiss. Netw. Offshore Wind Farms*, 2016.

[105] Ł. H. Kocewiak, B. L. Ø. Kramer, O. Holmstrøm, K. H. Jensen, and L. Shuai, "Resonance damping in array cable systems by wind turbine active filtering in large offshore wind power plants," *IET Renewable Power Generation*, vol. 11, no. 7, pp. 1069–1077, 2017.

[106] M. Lehmann, M. Pieschel, M. Juamparez, K. Kabel, Ł. H. Kocewiak, and S. Sahukari, "Active filtering in a large-scale STATCOM for the integration of offshore wind power," in *17th International Wind Integration Workshop*, 2018.

[107] S. Chaudhary, R. Teodorescu, L. Kocewiak, *et al.*, "Challenges in Integration of MMC STATCOM with Battery Energy Storage for Wind Power Plants," in *Proceedings of 18th Wind Integration Workshop*, 18th Wind Integration Workshop ; Conference date: 16-10-2019 Through 18-10-2019, Energynautics, Oct. 2019, ISBN: 978-3-9820080-5-9.

[108] A. G. Gonzalez-Rodriguez, "Review of offshore wind farm cost components," *Energy for Sustainable Development*, vol. 37, pp. 10–19, 2017, ISSN: 0973-0826.

[109] S. Rahman, I. Khan, H. I. Alkhammash, and M. F. Nadeem, "A Comparison Review on Transmission Mode for Onshore Integration of Offshore Wind Farms: HVDC or HVAC," *Electronics*, vol. 10, no. 12, 2021, ISSN: 2079-9292.

[110] *Hornsea 1 Wind Farm*, `https://orsted.co.uk/energy-solutions/offshore-wind/our-wind-farms/hornsea1`, Accessed: 2023-02-14.

[111] *Hornsea 2*, `https://hornseaprojects.co.uk/hornsea-project-two`, Accessed: 2023-02-14.

[112] E. Ebrahimzadeh, F. Blaabjerg, X. Wang, and C. L. Bak, "Harmonic Stability and Resonance Analysis in Large PMSG-Based Wind Power Plants," *IEEE Transactions on Sustainable Energy*, vol. 9, no. 1, pp. 12–23, 2018.

[113] Ł. H. Kocewiak, I. A. Aristi, B. Gustavsen, and A. Hołdyk, "Modelling of wind power plant transmission system for harmonic propagation and small-signal stability studies," *IET Renewable Power Generation*, vol. 13, no. 5, pp. 717–724, 2019.

[114] J. Hjerrild, S. Sahukari, M. Juamperez, *et al.*, "Hornsea Projects One and Two–Design and Execution of the Grid Connection for the World's Largest Offshore Wind Farms," in *Cigre Symposium Aalborg*, 2019.

[115] S. K. Chaudhary, R. Teodorescu, J. R. Svensson, Ł. H. Kocewiak, P. Johnson, and B. Berggren, "Black Start Service from Offshore Wind Power Plant using IBESS," in *2021 IEEE Madrid PowerTech*, 2021, pp. 1–6.

[116] S. K. Chaudhary, R. Teodorescu, J. R. Svensson, Ł. H. Kocewiak, P. Johnson, and B. Berggren, "Islanded Operation of Offshore Wind Power Plant using IBESS," in *2021 IEEE Power & Energy Society General Meeting (PESGM)*, 2021, pp. 1–5.

[117] Verband der Elektrotechnik Elektronik Informationstechnik e. V., "VDE FNN Guideline FNN Guideline: Grid forming behaviour of HVDC systems and DC-connected PPMs," 2020.

[118] M. Yu, A. J. Roscoe, A. Dyśko, *et al.*, "Instantaneous penetration level limits of non-synchronous devices in the British power system," *IET Renewable Power Generation*, vol. 11, no. 8, pp. 1211–1217, 2017.

[119] P. Kundur, "Small-Signal Stability," in *Power System Stability and Control*. 1994, pp. 699–825.

[120] C. A. Nickle and C. A. Pierce, "Stability of Synchronous Machines Effect of Armature Circuit Resistance," *Transactions of the American Institute of Electrical Engineers*, vol. 49, no. 1, pp. 338–350, 1930.

[121] B. Dunn, H. Kamath, and J.-M. Tarascon, "Electrical energy storage for the grid: a battery of choices," *Science*, vol. 334, no. 6058, pp. 928–935, 2011.

[122] C.-T. Pham, "Assessment of energy storage systems for power system applications based on equivalent circuit modeling," Ph.D. dissertation, KTH Royal Institute of Technology, 2019.

[123] A. F. Cupertino, W. C. S. Amorim, H. A. Pereira, S. I. Seleme Junior, S. K. Chaudhary, and R. Teodorescu, "High Performance Simulation Models for ES-STATCOM Based on Modular Multilevel Converters," *IEEE Transactions on Energy Conversion*, vol. 35, no. 1, pp. 474–483, 2020.

[124] S. K. Chaudhary, A. F. Cupertino, R. Teodorescu, and J. R. Svensson, "Benchmarking of Modular Multilevel Converter Topologies for ES-STATCOM Realization," *Energies*, vol. 13, no. 13, 2020, ISSN: 1996-1073.

[125] K. Sharifabadi, L. Harnefors, H.-P. Nee, S. Norrga, and R. Teodorescu, "Introduction to Modular Multilevel Converters," in *Design, Control, and Application of Modular Multilevel Converters for HVDC Transmission Systems*. 2016, pp. 7–59.

[126] J. R. Miller and P. Simon, "Electrochemical Capacitors for Energy Management," *Science*, vol. 321, no. 5889, pp. 651–652, 2008.

[127] P. Simon and Y. Gogotsi, "Materials for electrochemical capacitors," *Nature materials*, vol. 7, no. 11, pp. 845–854, 2008.

[128] C. Liu, F. Li, L.-P. Ma, and H.-M. Cheng, "Advanced materials for energy storage," *Advanced materials*, vol. 22, no. 8, E28–E62, 2010.

[129] P. Sharma and T. Bhatti, "A review on electrochemical double-layer capacitors," *Energy Conversion and Management*, vol. 51, no. 12, pp. 2901–2912, 2010, ISSN: 0196-8904.

[130] Q. Ke and J. Wang, "Graphene-based materials for supercapacitor electrodes – A review," *Journal of Materiomics*, vol. 2, no. 1, pp. 37–54, 2016, ISSN: 2352-8478.

[131] R. Signorelli, D. C. Ku, J. G. Kassakian, and J. E. Schindall, "Electrochemical Double-Layer Capacitors Using Carbon Nanotube Electrode Structures," *Proceedings of the IEEE*, vol. 97, no. 11, pp. 1837–1847, 2009.

[132] S. Vazquez, S. M. Lukic, E. Galvan, L. G. Franquelo, and J. M. Carrasco, "Energy Storage Systems for Transport and Grid Applications," *IEEE Transactions on Industrial Electronics*, vol. 57, no. 12, pp. 3881–3895, 2010.

[133] D. Linzen, S. Buller, E. Karden, and R. De Doncker, "Analysis and evaluation of charge-balancing circuits on performance, reliability, and lifetime of supercapacitor systems," *IEEE Transactions on Industry Applications*, vol. 41, no. 5, pp. 1135–1141, 2005.

[134] C. Shen, S. Xu, Y. Xie, M. Sanghadasa, X. Wang, and L. Lin, "A Review of On-Chip Micro Supercapacitors for Integrated Self-Powering Systems," *Journal of Microelectromechanical Systems*, vol. 26, no. 5, pp. 949–965, 2017.

[135] J. Kowal, E. Avaroglu, F. Chamekh, *et al.*, "Detailed analysis of the self-discharge of supercapacitors," *Journal of Power Sources*, vol. 196, no. 1, pp. 573–579, 2011, ISSN: 0378-7753.

[136] *Press-pack IGBT and diode modules*, `https://www.hitachienergy.com/products-and-solutions/semiconductors/stakpak`, Accessed: 2023-02-09.

[137] ENTSO-e, "Explanatory document for the Nordic synchronous area proposal for frequency quality defining parameters and the frequency quality target parameter in accordance with Article 127 of the Commission Regulation (EU) 2017/1485 of 2 August 2017 establishing a guideline on electricity transmission system operation," 2018.

[138] ENTSO-e, "Overview of Frequency Control in the Nordic Power System," 2022.

[139] ENTSO-e, "Fast Frequency Reserve - Solution to the Nordic inertia challenge," 2019.

[140] M. Persson, "Frequency Response by Wind Farms in Power Systems with High Wind Power Penetration," *Chalmers University of Technology, Gothenburg, Sweden, PhD Thesis*, 2017.

[141] CIGRE, "Long Term Dynamics – Phase II – Final Report," 1995.

[142] ENTSO-e, "FCR-D design of requirements – phase 2," 2019.

[143] ENTSO-e, "Technical Requirements for Frequency Containment Reserve Provision in the Nordic Synchronous Area," 2022.

[144] P. Kundur, "Prime Movers and Energy Supply Systems," in *Power System Stability and Control*. 1994, pp. 377–462.

[145] D. Zografos, "Power System Inertia Estimation and Frequency Response Assessment," *KTH Royal Institute of Technology, Stockholm, Sweden, PhD Thesis*, 2019.

[146] Björk, Joakim and Johansson, Karl Henrik and Dörfler, Florian, "Dynamic virtual power plant design for fast frequency reserves: Coordinating hydro and wind," *IEEE Transactions on Control of Network Systems*, pp. 1–12, 2022.